UNIVERSITÀ DI PARMA

UNIVERSITA' DEGLI STUDI DI PARMA

DOTTORATO DI RICERCA IN

"SCIENZA E TECNOLOGIA DEI MATERIALI"

CICLO XXXI

Improving organic electrochemical sensing by aptamer functionalization

Coordinatore:

Prof. Enrico Dalcanale

Tutore:

Dr. Salvatore Iannotta

Co-Tutore:

Dr. Silvia Battistoni

Dottoranda: Carlotta Peruzzi

Anni 2015/2018

L’espressione più eccitante da ascoltare nella scienza, quella che annuncia le più grandi scoperte, non è “Eureka” ma “Che strano…”.

(Isaac Asimov)

CONTENTS

Organic Electronics in Biology .....

1.1 Biomarkers of diseases 1

1.2 Biosensors: Designs and Types 2

1.2.1 Bioreceptors 5

1.3 Aptamers 5

1.3.1 Transducers 8

1.4 From Inorganic to Organic Electronics 12

1.5 Organic Thin Film Transistors (OTFTs) 14

1.6 State of the art of OECTs in Biology 16

1.6.1 OECTs interfacing Cells 17

1.6.2 OECTs as Enzymatic Sensors 19

1.6.3 OECTs as Immunosensors 20

1.6.4 OECTs Sensing Nucleotides 21

1.7 OECTs Gate Selection 22

1.8 Thrombin-aptamer interaction 26

Organic Electrochemical Transistors .....

2.1 Intrinsically Conductive Polymers (ICPs) 29

2.2 The Discovery of PEDOT 35

2.3 From PEDOT to OECTs 38

2.4 operating principles 39

2.5 OECTs Behavior Models 43

2.5.1 Channel geometry and OECTs response 46

2.5.2 Gate Effect on OECTs response 48

2.6 OECTs FABRICATION 51

Materials and Methods .....

3.1 OECTs Fabrication 54

3.2 Graphene Gate Electrode Fabrication 55

3.3 OECTs driven by PMLG Gate Electrode: electrical characterizations 56

3.4 Synthesis and Characterization of Gold Nanoparticles 57

3.4.1 Characterization of the AuNPs 58
3.5 AuNPs Electrophoretic Deposition 59
3.5.1 AuNPs-PMLG gate electrode characterizations 59
3.6 Optimization of the Aptamers Concentration 60
3.6.1 Aptamers Preparation and Adsorption 60
3.6.2 Blocking the Gate Electrode Surface 60
3.6.3 OECTs driven by TBA_{15} modified AuNPs-PMLG Gate Electrode 60
3.7 Thrombin Detection 61
3.7.1 OECT driven by a Thr-incubated TBA-15 modified AuNPs-PMLG Gate Electrode 62
3.7.2 Evaluation of the Aptasensor Selectivity/sensitivity 62
Results and Discussion .....
4.1 PMLG Gate Electrode Morphology 63
4.2 PMLG - OECTs Electrical response 66
4.3 Gold Nanoparticles (AuNPs) 73
4.4 decoration of a PMLG electrode with AuNPs 75
4.5 response of an OECT with AuNPs-PMLG as gate electrode 76
4.6 Functionalization of AuNPs-PMLG Gate Electrode by Immobilization of Thrombin Binding Aptamer-15 (TBA-15) 78
4.7 Detection of Thrombin 91
Conclusions 95
Bibliography .....

Abstract

One of the most critical points for achieving a best prognosis is to diagnose a disease at its early stages. The ability to detect the onset of a disease, in fact, is crucial for the patients' survival. To this end, it is essential to develop tools that could reliably predict and diagnose an illness. Since the human body responds to the development of a disease by producing or changing levels of specific biomolecules, these biological markers (biomarkers), could be used to predict a disease and its evolution. The biomarkers are present in body fluids like urine, blood or saliva so that various detection methods have been developed to detect them. Unfortunately most of these approaches still suffer from lack of accuracy, sensitivity and specificity. The need to develop more efficient and reliable sensing technologies reinforces the approach based on biosensors as a solution in terms of sensitivity and fast and cost-effective measurements. In general, electrochemical methods are widely used for the detection and quantification of biomolecules because of their unique properties, such as rapid response and low-cost detection. In addition, they demonstrate the potential for the fabrication of re-generable biosensors with low detection limits, a wide linear response range, and good stability that could be easily miniaturized.

Within this challenging framework, the research activity developed during this PhD project has dealt with the development of biosensors based on Organic Electrochemical Transistors (OECTs) as the transduction element and aptamers ad bioreceptors. In OECTs, the key material is the poly(3,4-ethylendioxythiophene):polystyrene sulfonate (PEDOT:PSS), which is a flexible and biocompatible conductive organic polymers. This polymer can efficiently transduce an ionic signal, typical of the bio-world, into an electronic one with a high amplification allowing the detection of very low concentrations of biomarkers. Aptamers are short RNA or single-stranded DNA able to recognize with unprecedented selectivity a great variety of targets even compared to antibodies, which for long time have represented the gold standards in biosensors.

Generally, for biological application, the selectivity of an OECT can be engineered though the functionalization of the PEDOT:PSS or of the gate electrode, or by controlling the (bio)chemistry of the elctrolyte. In this project, we choose to functionalize the gate electrode, based on a multilayer graphene (PMLG), with thiolated-aptamers, though the non-covalent modification of the graphene

surface with gold nanoparticles (AuNPs), which can be used as binding sites because of the high affinity between gold and sulfur. The OECTs developed have been engineered for the selective detection of thrombin, which is a protein involved in the blood coagulation and it plays an essential role for homeostasis in many physiological systems and hence representing a quite good test case for our approach. The performance of our sensing devices has been investigated quite carefully, starting from the physico-chemical properties of the materials and interfaces, and hence by different electrical characterizations to extract some key parameters. We demonstrate that a AuNPs-PMLG composite gate electrode leads to several advantages compared to metallic electrodes generally used for this type of applications.

The main overall achievement of this work has been the development and demonstration of biosensors that, based for the first time on the combination of OECTs functionalized by aptamers, show limit of detection for monitoring thrombin down to its physiological concentrations in the real natural conditions with a great selectivity. We believe that our approach could be now expanded to a variety of different biomarkers and hence paving the way to a variety of different bio-medical applications.

Chapter 1

ORGANIC ELECTRONICS IN BIOLOGY

1.1 BIOMARKERS OF DISEASES

The early diagnosis of a disease and monitoring the patient therapeutic progression play a crucial role in modern medicine. The ability to detect the onset of a disease plays a very important role to accelerate healing process and to improve patients' survival while the continuous monitoring of the overall progress of the disease during and after treatments is considered fundamental for the patient care.

To this end, it is essential to develop tools that could reliably support the prediction, diagnosis, progression, regression or outcome of treatments of illness. Since the human body responds to the progression of diseases by producing and/or changing levels of specific groups of biomolecules, the detection or monitoring of such biological markers (**biomarkers**), can be used to predict, detect and monitor state of health or the onset of an illness. Biomarkers range from biomolecules like carbohydrates, proteins, lipids to genes, DNA, RNA, enzymes, hormones, changes in biological structure or a characteristic feature (such as blood pressure).

In 2001, the Biomarkers Definition Working Group defined biomarkers as "*A characteristic that is objectively measured and evaluated as an indicator of normal biological processes, photogenic processes, or pharmacological responses to a therapeutic intervention.*"[1]

Nowadays, there are different methods to classify biomarkers based on their different applications. A system, described by *Frank* and *Hargreave*[2], divides biomarkers into three types:

- **Type 0:** *Markers of the natural history of a disease, which correlate longitudinally with known clinical indices, such as symptoms over the full range of disease states.*
- **Type I:** *Markers, which capture the effect of an intervention in accordance with the mechanism of action of the drug, even though the mechanism might not be known to be associate with clinical outcome.*
- **Type II:** *Markers which are considered* ***surrogate endpoints*** *because change in that marker predicts clinical benefits.*

Another classification system suggested by the Food and Drug Administration (FDA)[3] categorized the various biomarkers under the groups of:

- **Diagnostic Biomarkers:** *A biomarker used to detect or confirm presence of a disease or condition of interest or to identify individuals with a subtype of the disease.*
- **Prognostic Biomarkers:** *Indicate future clinical course with respect to a specified clinical outcome, in the absence of therapeutic intervention.*
- **Predictive Biomarkers:** *Identify patients likely to respond (favorably or unfavorably) to a specific treatment.*
- **Response Biomarkers:** *Indicate the biological response has occurred in a patient after having received a therapeutic intervention.*

It should be mentioned only a very few particularly favorable cases a single biomolecule could be considered a reliable biomarker that gives a definite response on the health state with respect to a specific disease. In absolutely most of the cases, the combination of several biomolecules and their evolution in time is necessary to reliably assess the health status or the evolution of a diseases. This is why multi-molecular and/or multiparametric sensing devices and systems are the best choice for making a fundamental step forward in the field and in particular for home-care.

1.2 Biosensors: Designs and Types

Biomarkers can be found in body fluids like urine, blood, saliva, tears or sweat and in tumor tissues and serum. The assessment and definition of "good" biomarkers is a field of extensive research, the evolution of which depends also from the instrumentation available covering large dynamic ranges in terms of sensitivity and preparation of samples. In the field of biomarkers detection, one of the major aims of researcher is to develop fast, reliable and cost-effective analytical methods, which

could be easily and routinely used even by unprofessional personnel. In the past few decades, significant and substantial progress has been made in this field. Various biomarkers detection methods have been developed such as polymerase chain reaction (PCR), enzyme-linked immunosorbent assay (ELISA)[4–6], electrophoresis[7–9] radioimmunoassay, colorimetric assay, fluorescence methods etc. Most of these methods, however, still suffer from the lack of accuracy, sensitivity and specificity for clinical applications and some of them have also disadvantages like being time-consuming, hazardous to health and requiring highly trained operators or expensive and sophisticated instrumentation.[10]

Therefore, strong efforts have been carried out to develop more efficient and reliable sensing and monitoring technologies, able to perform sensitive, fast and cost-effective measurements taking advantage of biological processes: nowadays this technologies are qualified as "**biosensors"** .

According to IUPAC recommendations a biosensor can be defined as "*An independently integrated receptor transducer device, which is capable of providing selective quantitative or semi-quantitative analytical information using a biological recognition element.*".[11]

Appeared for the first time in 1962 when Clark and Lyons[12] coupled a glucose oxidase to an amperometric oxygen electrode for the direct detection of glucose in a sample (correlating the acquired drop in oxygen to the conversion of glucose to gluconic acid and hydrogen peroxide[13]), a biosensor consists of three main elements: a bioreceptors, a transducer and a signal processing system (Fig. 1.1).[14]

The bioreceptor is a biological sensitive component that recognizes the target analyte, while the transducer is a physicochemical detector component that coverts the interaction between the analyte and the bioreceptor into a measurable signal. Finally, the processing system is a complex electronic circuit that performs signal conditioning such as amplification and conversion from an analogic signal to a digital one.[15]

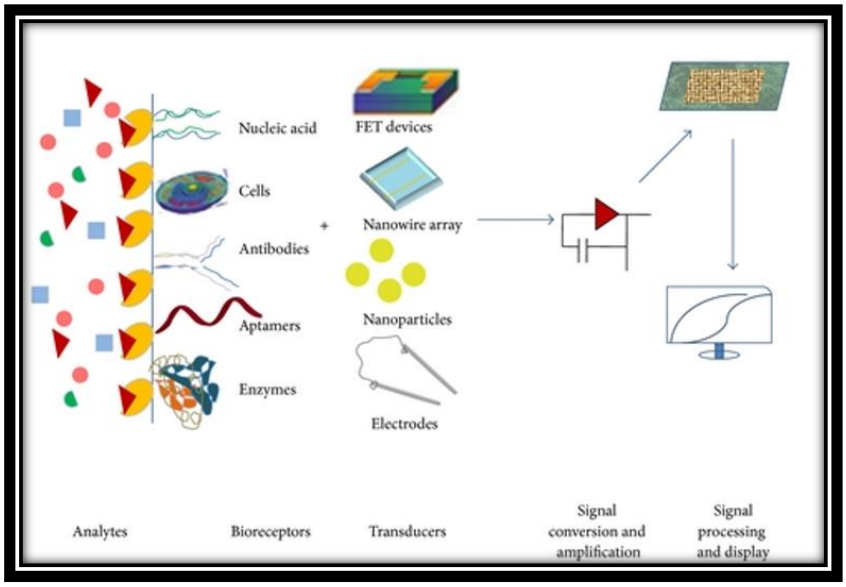

Figure 1.1: *Schematic diagram of biosensor components. (Adapted with permission from D. Grieshaber © English: Biosensors systems and components, (2008))*

Fig. 1.2 schematically reports the most common biosensors classification, in which they are categorized either by the type of biological element used and/or by the type of signal transduction employed.[16]

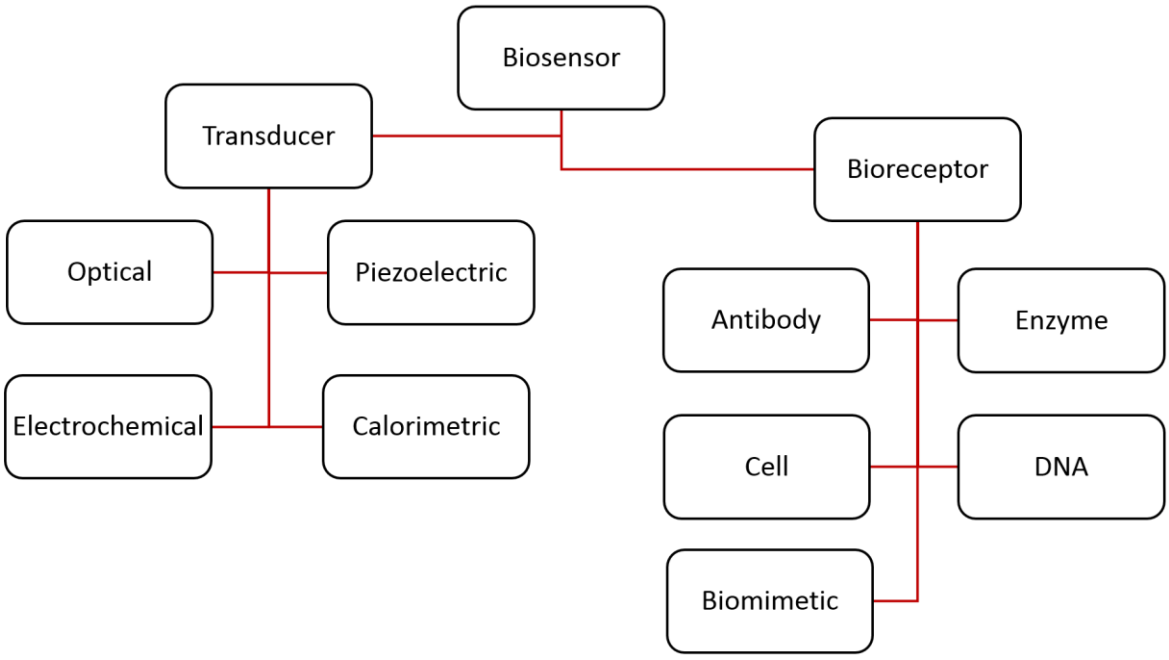

Figure 1.2: *Schematic classification of transducers and bioreceptors used in biosensors*

1.2.1 Bioreceptors

As already mentioned and reported in figure (Fig. 1.2), biosensors can be classified by the type of biological signaling mechanism that in turn are divided into five major categories:

1. **Antibody/Antigen**: take advantage of the specific chemical interaction between antibodies and antigens during an immune reaction.[17,18]
2. **Enzymes**: are based on the detection of the products of reaction between the analyte and the enzyme, which is able to bio-catalyze the reaction and bind specifically the target molecules.[19–21]
3. **Nucleic Acids:** in which the highly specific affinity binding's reaction between two single strand of DNA (ssDNA) to form a double stranded DNA (dsDNA) is used in this kind of biosensors which appoint nucleic acids as the biological recognition elements.[22,23]
4. **Cells and Viruses:** that use the ability of living cells to detect the intra and extracellular microenvironment condition and physiological parameters, therefore, in addition to analyte sensing and detecting, they provide a useful tool to study the in situ effects of analytes.[24,25]
5. **Biomimetic materials:** constituted by artificial or synthetic materials that mimic the function of natural bioreceptors. An example of this class of bioreceptors are Aptamers that are synthetic strands of nucleic acid that can be designed to recognize amino acids, oligosaccharides, peptides and proteins.[26]

The choice of biological material depends on several factors such as specificity, storage, operational and environment stability. The key factor, for a bioreceptor, is to be selective towards a specific analyte to avoid interference with another substance from the sample matrix.[27]

Different recognition molecules have been employed for clinical diagnosis. Antibodies based systems represent the gold standard in biosensors. However, the use of antibodies in biosensors can face limitations due to the antibody binding capacity that is strongly dependent on the assay conditions (e.g. pH and temperature) while the antibody-antigen interaction is generally irreversibile.[28] For these reasons novel bioreceptors, such as aptamers, are currently being more and more explored and considered to replace antibodies on biosensors.[15]

1.3 APTAMERS

In 1990 three different laboratories have independently reported the development of an *in-vitro*

selection and amplification technique for the synthesis of specific nucleic acid sequences, which can bind, with high affinity and specificity, a wide array of non-nucleic acid trargets.[29–31] Aptamers are short RNA or single-stranded DNA, composed by a selected sequence of the 4 nucleotides to form strands of usually 20-80 units (6-30 kDa molecular weight). Aptamers can form different secondary structures, such as loops, stems, bulges, psuedoknots and G-quadruplex, which in turn lead to specific three-dimensional architectures able to specific recognize a target molecule. As shown in Fig 1.3, they can bind a specific target using high specificity and affinity through van der Waals or electrostatic interactions, hydrogen bonding, stacking of flat moieties and shape complementarity, with dissociation constant K_d ranging from pico to nanomolar.[32]

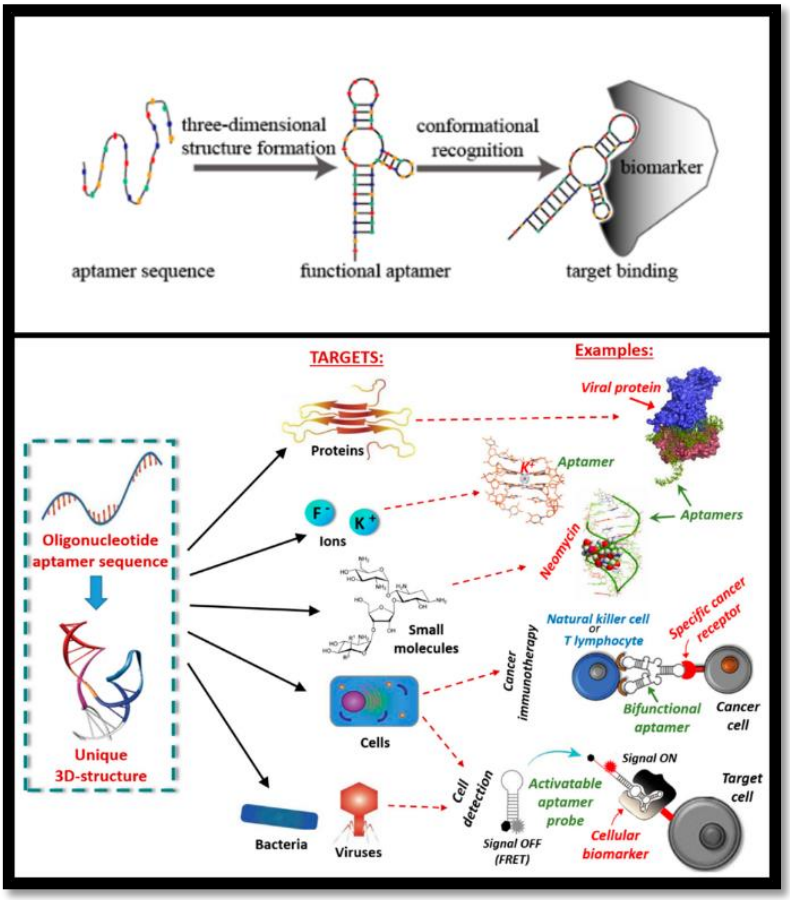

Figure 1.3: *Formation of an aptamer-target complex during detection and conformational recognition of the target of interest. Aptamers are able to bind with high affinity and specificity a wide range of targets like metal ions, organic dyes, nucleotides, amino acids, proteins, cells and entire organism including virus and bacteria.(Adapted with permission from Sun H.et al,[33] © (2015) Molecules)*

Since their discovery, aptamers have attracted great interest in the area of therapeutics and diagnostics, because aptamer-based biosensors possess unprecedented advantages if compared with biosensors using other natural receptors such as antibodies and enzymes.[34] With aptamers, is possible

to develop "**aptasensors**" selective to a wide range of specific targets (from small molecules to large proteins and even cells), thanks to the possibility of an *in-vitro* synthetization of aptamers specific for any given target. Differently from antibodies or enzymes, aptamers are usually highly chemical stable and have longer shelf life[35], and moreover, they are produced with simple, fast and inexpensive process, because, unlike antibodies, aptamers do not required animals or immune response for their production,.[36] Their chemical synthesis and the *in-vitro* selection can be automatized leading to rapid parallel production of different aptamers against complex target sets[37] and giving the possibility of generating aptamers against toxic compounds, which would kill the animal in the antibodies production. The stability of the aptamers can be further increased by chemical modification of the nucleotides: labels and linkers, for detection and conjugation, can be easily inserted at the desired position in the oligonucleotide sequence, without compromising the binding affinity or selectivity.[38] Usually, the use of aptamers in biosensors allows to obtain device with high detection sensitivity and selectivity often superior to biosensors based on antibodies as bioreceptors.[39,40] Nowadays, in fact, many authors proposed aptamers as a powerful and satisfactory alternative to antibody-based in the detection technique of several diseases from leukemia[41] to breast cancer.[42]

The conventional method for aptamers engineering, known as SELEX (Systematic Evolution of Ligands by Exponential Enrichment), is an *in vitro* process that allows the selection of different oligonucleotides sequences from approximately 10^{12}-10^{15} combinatorial oligonucleotide libraries.[36] A schematic representation of the SELEX process is reported in Fig. 1.4 and it includes four steps that are iteratively repeated in order to find the oligonucleotide sequence with the highest affinity toward the chosen chemical or biological target.

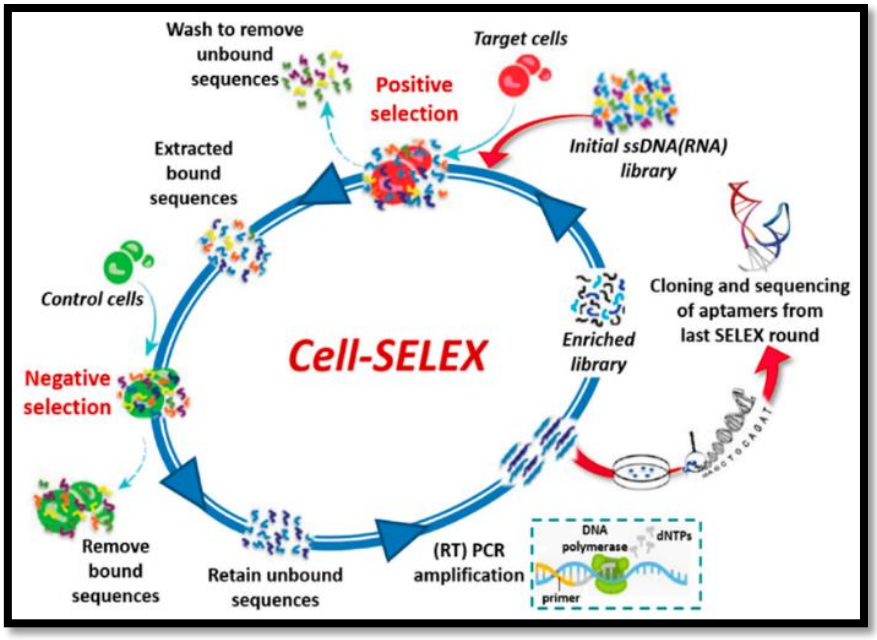

Figure 1.4: *Schematic representation of SELEX process steps. (Adapted with permission from Musumeci D. et al,*[43] *© (2003) Cancers)*

The first SELEX step is the binding procedure in which the target molecule is incubated with a library of 20/60 nucleotide random sequences under specific experimental conditions. In the second stage, the target-bound aptamers are separated from the unbound components (e.g. by gel shift or filtration through nitrocellulose). The third phase involves the elution of the bound sequences from the target through heterogeneous (filtration, affinity chromatography or magnetic bead-based separation) or homogenous methods (electrophoretic, microfluidic or microarray-based separation). In the fourth and last step, the amplification by PCR of the selected aptamers is performed to create a new library to be used in the next round.[44] This library can be used as starting point for the next round selection that involves the same steps described. After the final round, PCR products are cloned and sequenced to identify the high affinity aptamers. Finally, the identified aptamers are synthetized and studied to control their target affinity and binding specificity.[45]

1.3.1 Transducers

The way to classify biosensors is based on the signal transduction mechanisms that are divided in four main classes:

1. **Optical:** optical detection is performed by exploiting the interaction of light with a biorecognition element. Optical biosensors can be divided into two big groups: label-free and

label based. Briefly, in a label-free mode, the signal is generated directly by the interaction of the analyzed material with the transducer. In contrast, label-based sensing involves the use of a label. This method of transduction has been employed in many classes of biosensor due to many different types of spectroscopies that could be used such as absorption, fluorescence, phosphorescence, Raman, SERS, refraction and dispersion spectroscopy.[46–48]

2. **Electrochemical:** this method measures the current produced from oxidation and reduction reactions between the biomolecules immobilized on an electrode and the target analyte. The current produced during the recognition process is correlated either to the concentration of the electroactive species or to its rate of production/consumption. Electrochemical biosensors can be further divided in four categories: amperometric, potentiometric, impedance and conductometric, according to the nature of the electrochemical changes detected during the biorecognition event.[49–51]
3. **Piezoelectric (mass-sensitive):** the receptors is immobilized on an oscillating crystal, whose resonance frequency depends on the total crystal's mass, and thus, after the binding between the biorecognition element and the target, the mass of the crystal increases and the oscillation frequency varies, consequently. The resulting oscillation frequency change can be measured electrically and used to determinate the mass of the analyte of interest tied to the crystal.[52]
4. **Calorimetric (thermos-metric):** the biomolecules are immobilized onto a sensor that measures the changes in temperature during the reaction between the bioreceptor and suitable analytes. The total heat produced or absorbed is proportional to the analyte concentration, so this change in temperature can be correlated to the amounts of reactants consumed or products formed. The heat change is measured using either a thermistor or a thermopile.[53,54]

The four classes of signal transduction methods and the already mentioned types of bioreceptors can be combined for the fabrication of efficient sensors with multiple applications and features.

For example, the development of aptasensors has been carried out with various detection schemes, from label-free methods like surface plasmon resonance (SPR),[55,56] surface acoustic wave (SAW),[57] quartz crystal microbalance (QCM)[58,59] and microchannel cantilever sensors[60] to other methods often requiring labels such as electrochemistry,[61–63] fluorescence[64] and chemiluminescence.[65] So far, the aptasensors most widely used are those where aptamers are integrated with optical or electrochemical transduction.[66]

Optical aptasensors are widely used for the detection of small molecules such as adenosine and

dopamine. These biosensors include aptamers labeled with fluorophore, luminophore and nanoparticles or aptamers with label free detection systems. Actually, most of the methods are mainly based on fluorescence-based optical biosensors where the target recognition is always accompanied by changes in fluorescence emission due to an enhancement (signal-on) or a quenching (signal-off) effect.[43] An example of signal-on fluorescence based aptasensors is reported in Fig 1.5 developed by Montesarchio et al.[45] for the detection of thrombin. It exploits the host-guest system dansyl/β-cyclodextrin, where β-cyclodextrin can capture the dansyl fluorescent group increasing its fluorescence emission.

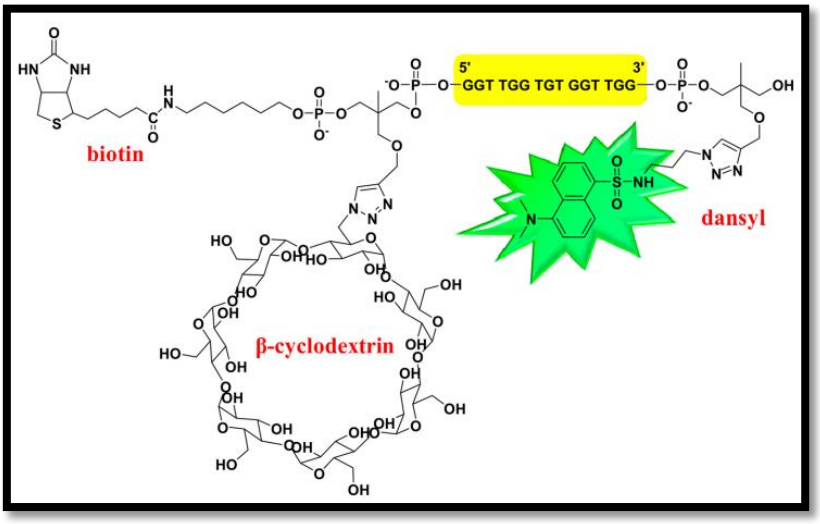

Figure 1.5: *Molecular structure of Tris-m-TBA with structural modifications. The oligonucleotide sequence is highlighted in yellow and the dansyl group (fluorophore) is highlighted in green. (Adapted with permission of Riccardi C. et al,[45] © (2017) American Chemical Society)*

In this system, both dansyl group and β-cyclodextrin are anchored on the aptamer (Tris-m-TBA), respectively on the 3' and 5' terminal. At the aptamer 5' end there is also a biotin moiety. When Tris-m-TBA is unfolded, the dansyl probe shows only a basal fluorescence. In turn, when Tris-m-TBA is folded into an antiparallel, unimolecular G-quadruplex structure, the 5' and 3' terminal move closer leading to the encapsulation of the dansyl group into the hydrophobic cyclodextrin cavity. In these conditions, the dansyl group fluorescence is enhanced.

Recently, electrochemical devices have received considerable attention for the transduction of aptamers-target interactions. Electrochemical transduction offers several advantages, including high sensitivity, which can be further increased by attaching labels to the aptamer-target complexes, and

scalable, easy and low cost fabrication processes since they do not require expensive instruments as in the case of optical transducers.[66] The first electrochemical aptasensors was an amperometric device used for the thrombin detection[67] that was developed using two different anti-thrombin aptamers that can recognize different parts of the target (Fig. 1.6).

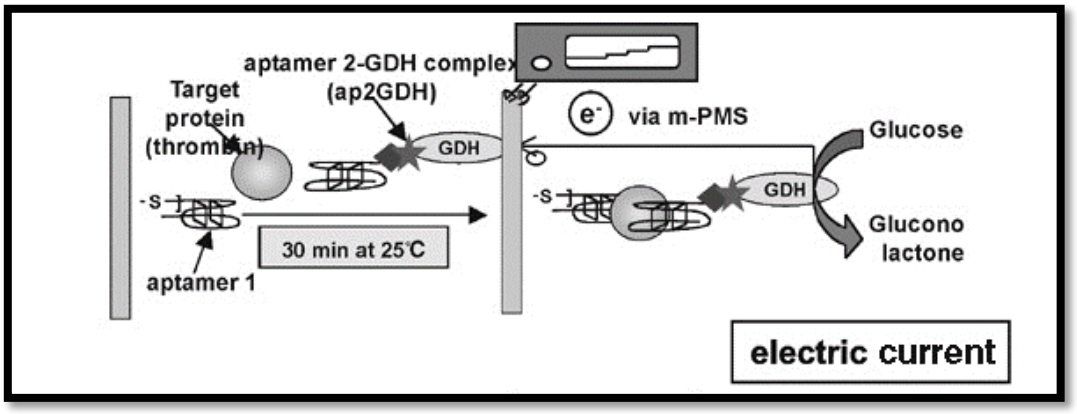

Figure 1.6: *Scheme of the electrochemical detection system of thrombin. The first thilated aptamer (aptamer 1) is anchored onto the gold electrode; the target thrombin and the GDH-labeled aptamer (ap2-GDH) are incubated in the reaction buffer for 30 minutes at RT. After the formation of the complex aptamer1-thrombin-ap2GDH, glucose is added and the current response is measured. (Adapted with permission from Ikebukuro K. et al,[67]© (2004) Taylor & Francis)*

As shown in Fig. 1.6, a sandwich architecture was used with a glucose dehydrogenase GDH-labeled anti-thrombin aptamer for the thrombin recognition and another aptamer immobilized onto a gold electrode to capture the protein. The thiolated aptamer captures and immobilizes the thrombin onto the gold electrode, exposing its free portion to the interaction with the second GDH-labeled aptamer for the formation of a complex where the protein is between the two aptamers. A current response can be measured with the addition of glucose, which can react with the GDH enzyme linked on the aptamer.

Biosensors have a very wide range of applications such as industrial process control, medical diagnosis, drug development, environmental field monitoring and many more, since, in most cases, these devices provide better stability and sensitivity as compared with traditional methods.

Generally, successful biosensors must possess high selectivity and sensitivity matching the typically extremely low concentration of biomarkers and the needed disease selective detection. Other requirements including repeatability, stability, cost-effectiveness, reusability and disposability are of vital importance.[68]

1.4 FROM INORGANIC TO ORGANIC ELECTRONICS

Electrical methods for biological sensing are considered advantageous, in particular because they are label free and do not require expensive and time consuming techniques such as fluorophores or chromophores (optical methods).[69] The electrical diagnostic approach includes electrochemical biosensors, passive metal electrodes and/or large scale integrated systems, in which the electrode interface acts as a transducer between the electrons, processed in electronic circuits, and the ions of biological tissue.[70] Nowadays, improving the conversion of the ionic current, that flows in the electrolyte, in an electronic current, that flows in the electrode, is crucial to optimize the sensitivity of these type of biosensors. Since the impedance of the electrode is an expression of how difficult this conversion is performed, to achieve low impedance characteristics, a high amount of charge needs to be stored at the interface, which needs to be easily accessed by the ions from the electrolyte. One option is to increase the effective surface area by the incorporation of porous structures or equivalent conducting 3D structures.[71] A state-of-the-art solution involves the use of **conductive organic polymers** (discussed in more details in Chapter 2) as they can create porous coatings with high charge storage capacity and fast ion conduction. The use of conducting organic polymers coatings can facilitate highly selective transduction, since they can be synthesized including various receptors or anchoring sites, as well as to express desired chemical characteristics. Due to their "soft" nature, these materials can also be produced with geometries, morphologies, and mechanical properties providing minimal invasiveness and, ensuring bio-stability over long periods.[72]

The combination of both electronic and ionic conductivity with semiconducting organic polymers and small molecules, has driven, in recent decades, the development of **Organic Bioelectronics** (term coined by Berggren and Richter-Dahlfors in their seminal review)[73] as excellent tools to effectively interface biology with conventional electronics.[71]

Interest in organic electronic materials dates back to fundamental studies of their electronic structure conducted in the '60s[74] followed by the demonstration of the possibility of developing conducting polymers[75] in the mid '70s, by Heeger at al.. Few years later, the commercialization of organic electronic materials in electrophotography [76] began paving the way for the launch in the '90s, of a variety of organic-based devices including light emitting diodes, transistors and solar cells.[77,78] As can be seen in Fig. 1.7, which is a schematic representation of the publication trend in organic electronics compiled using data from ISI Web of Science, in contrast with other applications, the interfacing of organic electronics with biology is an emerging trend in the field.[79]

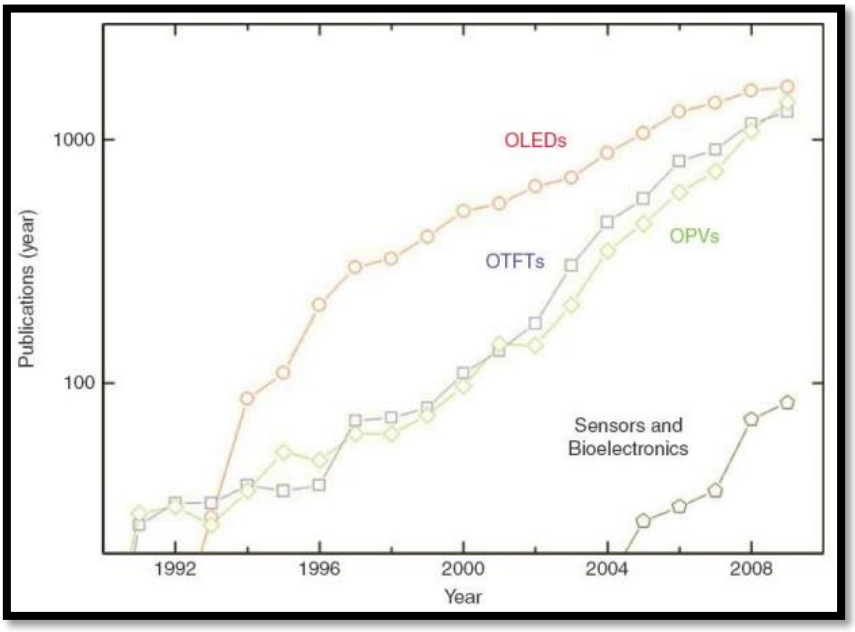

Figure 1.7: *Since their discovery, publications on organic light-emitting diodes (OLEDs), organic thin film transistors (OTFTs), and organic photovoltaics (OPVs), show a dramatic increase in the past decade, while the use of organic electronic in sensors and bioelectronics shows a recent involvement. (Adapted with permission from Owens R.M. et al,*[79] *© (2010) Cambridge University Press)*

In addition to the already mentioned advantages, the most useful properties of organic electronic materials are the ability to conduct ions, in addition to electrons and holes, and their affinity to directly (oxide-free) interface electrolytes. These features, together with their compatibility with biological molecules in neutral aqueous solutions and the wide number of functionalizations with specific groups as anchor sites, gives the opportunity of coupling conducting polymers with several classes of biological recognition elements such as antibodies, oligonucleotides, and living cells.[80–82]

One of the most promising conducting polymer is polyaniline (PANI) that has been largely employed in the development of electrochemical biosensors. An example is the detection of glucose using composites of PANI and $NiCo_2O_4$ nanoparticles.[83] Despite the unique properties of PANI composites, there are some limitations to their use in biosensors under physiological conditions since, for example, PANI is inactive at neutral pH. Other systems based on PANI composites have been coupled with different bioreceptors, such as AuNP-functionalized PANI and multiwalled carbon nanotube (MWCNT) composite was covalently attached to an antibody for 2,4-dichlorophenoxyacetic acid (2,4-D) herbicide detection.[84]

Another example of conducting polymers is polypirrole (PPy). Due to its beneficial and unique

chemical, physical, and electronic properties, PPy and its composites with metal and metal oxide nanoparticles (NPs), MWCNTs, graphene, enzymes, and electron-transfer mediators have been studied as electrochemical electrode materials, particularly for biosensing applications. A DNA sensor was developed using a PPy-AuNP composite electrode in which the DNA detection was performed by immobilizing the captured DNA strand on the AuNPs, and the hybridization assay was performed by exposing the modified electrode to the target and then to the HRP-modified probe strand. This study demonstrated the detection of DNA concentrations at the pM level.[85] Furthermore enzymatic glucose sensors were reported attaching covalently the glucose oxidase (GOx) enzyme to PPy nanowires,[86] or using a biocompatible chitosan-GOx complex immobilized on a PPy/Nafion/MWCNT nanocomposite electrode.[87]

Thiophene-based composites have been used in the fabrication of many electrochemical sensors, including those that detect neurotransmitters,[88] gases,[89] glucose[90] and many other analytes. Polythiophene materials have been proven to be optimal surfaces for the stable immobilization of antibody molecules in a sensor. For examples, antibodies were immobilized on a polythiophene-graphene oxide composite enabling the sensitive detection of carcinoembryonic antigen (CEA).[91] Furthermore, immobilized GOx on a polymerized, newly synthesized thiophene conducting monomer, has achieved robust covalent binding between the biomolecule and the immobilization platform.[92]

The most widely used of all polythiophene polymers is the poly(3,4-ethylenedioxythiophene) (PEDOT), which, in his composite form with the poly(styrenesulfonate) (PSS), has been largely used in the fabrication of thin-film transistors (OTFTs).

1.5 Organic Thin Film Transistors (OTFTs)

OTFTs are experimenting an increasingly important role in a wide range of applications: from flexible displays to disposable sensors. Cost-effectiveness, easy fabrication and in particular biocompatibility with highly selective biological recognition elements, make OTFTs ideally suitable for sensing applications in cheap, single-use or disposable devices that deliver accurate results.[93]

OTFTs can be divided into two primary categories, namely, organic field-effect transistors (OFETs) and organic electrochemical transistors (OECTs), according to the operation principles and device

structures.[94]

The main components of an OFET (Fig. 1.9 a) are the active channel made of an organic semiconducting film, an insulating layer as the gate dielectric and three terminals: source, drain, and gate electrodes. The field effect is a phenomenon in which the conductivity of a semiconductor changes due to the application of an electric field normal to its surface, via a gate electrode in the device. Consequently, the channel current could be varied of several orders of magnitude by the gate voltage, indicating that the device is a type of amplifier or a transducer that can convert a voltage/potential signal into a current response.[95,96]

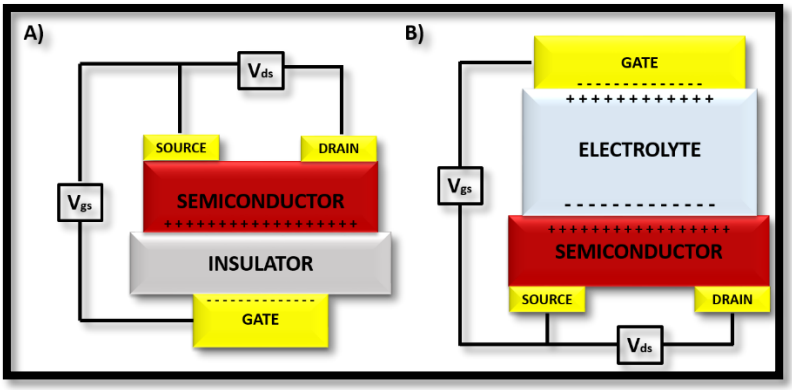

Figure 1.9: *Schematic illustration of a) FETs and B) OECTs architecture.*

On the other hand, an OECT has the same combination of electrodes (source, drain, and gate), but, instead of solid-state insulating layer, an electrolyte medium is placed in between the gate electrode and the organic semiconductor channel (Fig. 1.9 b).[97]

Compared with OFET-based sensors, OECT sensors offer a unique set of advantages for biomedical applications. First, OECTs can operate at much lower working voltages (about 1 V), preventing the risk of hydrolysis during operation. More importantly, OECT-based sensors can operate in aqueous electrolytes that are essential for real-time chemical and biological sensing applications. For example, these devices have shown high stability, reproducibility and reliable performances when maintained in cell culture media under physiological conditions for 5 weeks[98] or interfaced with cellular cultivation. [99] In addition, OECTs have a very simple and flexible structure that can be adapted to a wide variety of fabrication methods, from the most simple to most complex. The channel and gate electrodes could be fabricated separately, making easy their integration in complex systems, like

microfluidic channels, or their fabrication as sensor arrays for high throughput sensing.[99,100] PEDOT:PSS, which is one of the materials for the OECTs channel, is biocompatible and softer than silicon, allowing its conformation to 3D biological systems hence reducing by far the impact on cell and tissue samples. For this reason, OECTs have been integrated with natural and synthetic fibers for fully integrated sensors and wearable circuits.[101–104]

The most important feature of an OECT is its high amplification that is precious to increase the signal to noise ratio and improve the detection limit leading to an increased sensitivity. Khodagholy et al.,[105] showed OECTs with high amplification performance varying the device geometry. Rivnay et al[106] engineered OECTs with the highest amplification at zero gate voltage, giving the possibility of employing these devices in many low voltages biological applications .

All together the mentioned OECTs properties and features make them ideally suitable candidates for biosensing. Chapter 2 further describes the architecture, the operating principle and the methods for fabricating these transistors. The next paragraph is a report of the state of the art of OECTs in biological applications.

1.6 STATE OF THE ART OF OECTS IN BIOLOGY

Matsue et al.[107] were the first to incorporate a bio-recognition element into an OECT, in which the organic transistor acts as a transducer in a selective biosensor. They fabricate a microarray electrode coated with pyrrole-N-methylpirrole on which was immobilized diphorase (Dp), a flavin enzyme catalyzing the reduction of oxidized dyes by NADH (nicotinammide adenina dinucleotide).

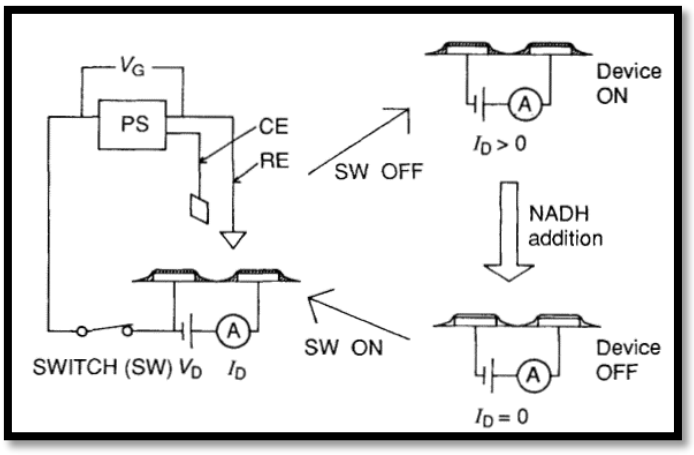

Figure 1.10: *Schematic device representation: two sets of Pt arrays on a glass substrate on which is electropolymerized the polymer containing Dp. The off-on response in observed only in the presence of Dp, confirming its catalyze activity*

of the polymer reduction by NADH. (Adapted with permission of Matsue T. et al,[107] © (1991) Royal Society of Chemistry)

The device scheme and working principle are shown in Fig. 1.10. Briefly, the oxidized form of the polymer is conductive and Dp immobilized on the polymer catalyzed its reduction mediated by NADH, thus the device transition from its ON to its OFF state (Low Resistance and High Resistance states, respectively) as a direct response to the addition of NADH.

1.6.1 OECTs interfacing Cells

The first OECT integrated with non-electrogenic cells was presented by Bolin et al.,[108] in which the Madin Darby canine kidney (MDCK) epithelial cells were seeded on the PEDOT:PSS channel and the device measured the electrochemical gradient established along the film. Cellular adhesion is regulated by changing the surface properties of the conductive polymer film via the application of appropriate voltages between the source and the drain terminals. This *in situ* control is of great interest for cell growth and to regulate migration and locomotion of cells. The authors have also reported that live cells can grow up and proliferate with long term stability demonstrating the biocompatibility of the polymer. OECTs transduce ionic to electronic signals so that it is quite sensitive to changes in biological ion fluxes, a parameter that could monitor the integrity of cells since dysregulation of cellular exchange liquids, is often a sign of dysfunction or disease. Jimison at al.,[109] have used OECTs for monitoring barrier tissue, which modulates ion flux between different bodily sections and its role is often compromised during toxic events. Time scales for non-acute events exceed minutes and can be extended for days or weeks. OECTs excellent stability and long-term operation makes them good candidates for long term measurements, as shown by Tria et al..[110] They used OECTs for monitoring the integrity of an *in vitro* model of the human intestinal epithelium after infection with the pathogenic organism *Salmonella typhimurium*. The advantages of live-cell-based measurements performed with OECTs is that the disruption of ion flow in the cell layer is only due to live pathogens and cannot be affected by dead bacteria or background flora which often leads to false positive. Cell death detection is a critical diagnostic issue because it can be the result of a physiological process or can be a consequence of pathological event. Romeo at al.,[111] for the first time, proposed an OECT based sensor for *in-vitro* monitoring of cellular dynamic, including stress and death induced by a drug treatment. They engineered an OECT with a Transwell (Twell) support integrated on the PEDOT:PSS channel as represented in Fig. 1.11.

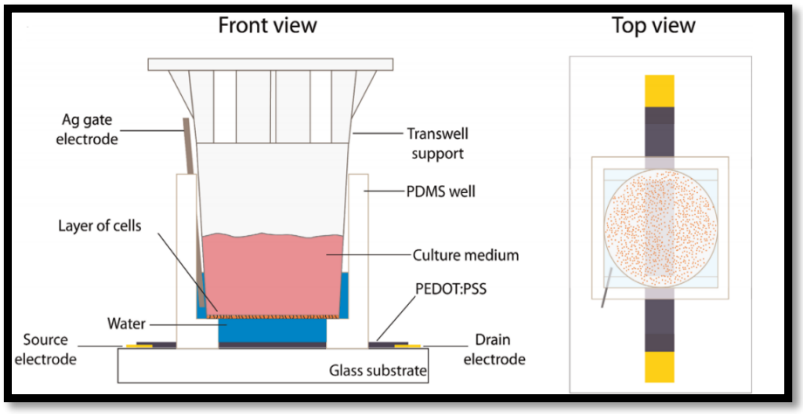

Figure 1.11: *Front and top view of the schematic representation of the OECT integrated with a Tweel support. (Adapted with permission of Romeo A. et al,*[112] *© (2015) Elsevier)*

The gate was immersed in a thin layer of pure water used as electrolyte and the cell culture media was confined in the Tweel and was separated from the electrolyte by a porous membrane. A monolayer of A549 cancel cells was cultured in the Tweel over the membrane, which shields the cations drift from the culture medium to the water electrolyte through the membrane. In this configuration, the OECT channel current, constitutes the base line characteristic since water acts as an electrolyte with zero ionic concentration. The exposure of A549 cells to the anticancer drug doxorubicin, leads to cell death and to the reduction of cancer cells covering the Tweel membrane. Consequently, the ionic flux across the membrane increases enriching the water electrolyte underneath, and this effect can be monitored by the OECT response in terms of current channel modulation that depends strongly by presence of ions. With an appropriate modelling this system demonstrates the highest observed sensitivity to the early stages of cell death and apoptosis. D'Angelo et al.,[113] extended this device and the same principle for the real time monitoring the consequence of osmotic stress on the cellular activity, which is often related to the occurrence of several disease conditions. In the works cited, cells were physically separated from the top-gated devices by the electrolyte and with the integration of filters. Cells can also be seeded directly on the channel adopting either a top-gate or a side-gate format. The former architecture was proposed by Lin et al.[114] to detect cells attachment and detachment by shifting the potential applied at the gate electrode. Ramuz et al.[115] engineered OECTs with both the gate and the channel in the same plane (side-gate format) and MDCK cells were seeded in order to cover directly an area comprising both the channel and the gate electrode. Exploiting the transparency of PEDOT:PSS, the author combined optical and electrical measurement for constantly monitoring ions flow in epithelial cells. *Physarum polycephalum* cells

(PPC) were integrated with an OECTs by Tarabella et al.[116] In this way, they engineered a hybrid "living" device, demonstrating for the first time an OECT simultaneously operating as a transistor with memristive properties. PPC is the slime mould with recognized properties of "intelligence", "solving problem" and "learning capacity" and these are the reason why recently it is largely used in unconventional computing. The paper demonstrate the ability to detect and monitor intracellular processes while being able to change its conductive status as a typical memristive device.

1.6.2 OECTs as Enzymatic Sensors

OECTs enzymatic sensors take advantage of changes in local pH upon species oxidation or transfer of electrons to the gate of the device. The former principle was propsed by Nishizawa et al.[117] to sense penicillin. The enzyme penicillinase that catalyze the oxidation of penicillin in pinicilloic acid, was immobilized on the top of the channel. This reaction leads to a change of the local pH, which increases the conductivity of the polymer. Zhu et al.,[118] in turn, demonstrated the use of OECTs for glucose sensing by measuring electron transfer. The sensing mechanism is based on the conversion of glucose in gluconoalactone catalyzed by the enzyme glucose oxidase in presence of oxygen, which leads to H_2O_2 as byproduct. The produced H_2O_2 transfers electrons to the Pt gate of the OECT. A Platinum electrode has been extensively used as gate in OECTs because of its good catalytic performance in the oxidation or reduction of several biomolecules. Tarabella et al.,[119] proposed OECTs with a Pt gate electrode for detecting and investigating the electrical properties of synthetic eumelanin, which is related to dynamic response of human skin and eyes to sun exposure. The Pt gate electrode induces an electrochemical reaction in presence of eumelanin (Fig. 1.12) leading to a change of the channel current.

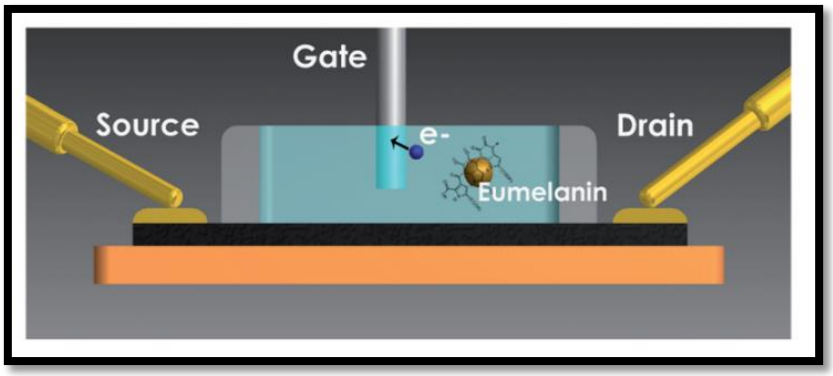

Figure 1.12: *Schematic diagram and electrical circuit of the OECT-based biosensor for the detection of eumelanin pigment in colloidal suspension. Oxidation of eumelanin at the Pt gate electrode lead to electron injection into the gate circuit. Cation produced during the oxidation are detected by the OECT which measures a channel current change. (Adapted with permission of Tarabella G. et al,[119]© (2013) Royal Society of Chemistry)*

Tang et al.,[120] have shown an improved OECTs limit of detection modifying the Pt gate electrode with Pt nanoparticles and carbon nanotubes. In this case the high electrocatalytic activity and the high surface to volume ratio of nanoparticles give to the modified electrode gates a greater sensitivity compared to pristine Pt, increasing the limit of detection to glucose to 10 nM. On the basis of the same principle, Kergoat and al,[88] have blended Pt nanoparticles with PEDOT:PSS to engineer OECTs for the glutamate and acetylcholine sensing. Another glucose sensor was developed by Shim et al.,[121] employing an all PEDOT:PSS OECT. To provide to the polymer low catalytic properties for the H_2O_2 oxidation, ferrocene has been used as mediator for transfer electrons to the gate electrode. An all plastic device was employed by Yang et al.[122] as glucose sensor using a room temperature ionic liquids as electrolyte instead of a liquid electrolyte, where the presence of evaporation could produce an unstable ionic concentration. The used of ionic liquids further improves the transistor long-term stability.

1.6.3 OECTs as Immunosensors

As sketched in Fig. 1.13, He at al.,[123] have functionalized the OECT channel with the *Escherichia coli* antibody, aiming at capturing the *E. coli* bacteria through antibody-antigen interactions.

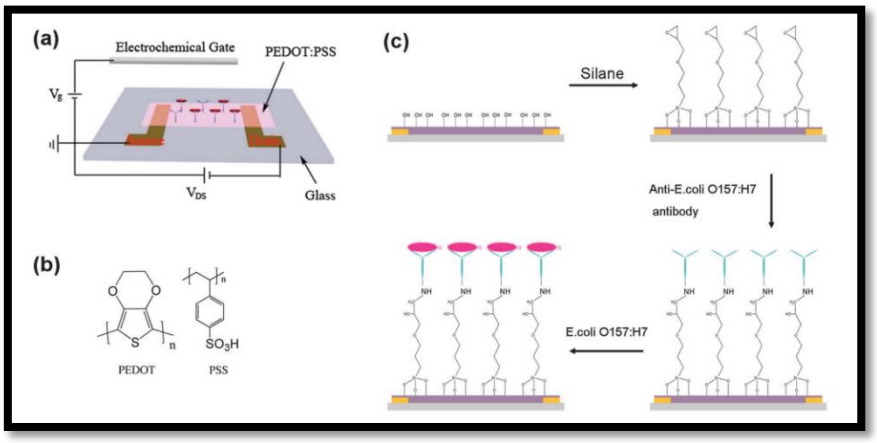

Figure 1.13: *a) Schematic diagram of OECT with an active layer of PEDOT:PSS functionalized with E. coli antibody; b) Chemical units of PEDOT and PSS polymers; c) Schematic diagram of the channel functionalization with the antibody and the following interaction with E. coli bacteria. (Adapted with permission from He R.X. et al.,[123] © (2012) Royal Society of Chemistry)*

Following the same principle, Kim at el.,[124] fabricated an OECT immunosensor for prostatic specific antigen (PSA) by functionalizing the channel with a PSA specific antibody. In this experiment a

sandwich-type immunosensor was developed in which the primary PSA monoclonal antibody was immobilized on the amine-functionalized PEDOT:PSS surface through a linker molecule. Successively, the PSA antigen was incubated and then a secondary polyclonal PSA antibody reacts with the bound antigen leading to a detectable signal. Signal amplification was performed linking gold nanoparticles (AuNPs) to the polyclonal PSA antibody.

1.6.4 OECTs Sensing Nucleotides

Nucleic acid diagnostic has relevant applications in gene expression monitoring, viral and bacterial identification and in clinical medicines. Lin et al.,[125] engineered an OECT for DNA sensing, in which the device was integrated in a flexible microfluidic system, as shown in Fig. 1.14.

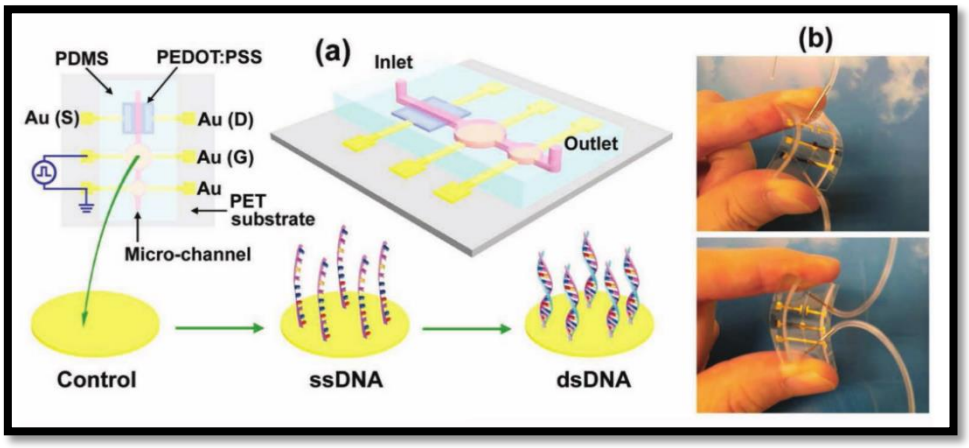

Figure 1.14: *a) The OECT is fabricated on flexible polyethylene terephthalate (PET) as substrate and integrated in a microfluidic channel formed by poly(dymethylsiloxane) (PDMS) on the top. B) The device can be easily bent to both sides. (Adapted with permission from Lin P. et al.,*[126] *© (2011) Wiley Online Library)*

A single stranded DNA has been immobilized on the gate electrode to detect the complementary DNA targets. A similar approach was also performed by Liao et al.,[127] by developing an OECT based DNA sensors for detecting diatoms, a type of algae found in the seawater.

These are the only two published papers founded in literature claiming the integration of OECTs with DNA strands and, no works reports yet on the OECTs functionalization in either the gate or the channel with aptamers. Some pioneering examples of thin film transistors modified with aptamers are of FET type. Lee and coworkers,[128] first demonstrated single-walled carbon nanotube field-effect transistors (SWCNT-FETs) sensing thrombin. The anti-thrombin aptamers were covalently

immobilized on the SWCNT channel. An antibody size (~ 10 nm), is larger than the typical electrical double layer hence, in most cases, the charged protein will be at distance greater than the Debye length (~ 3 nm). Therefore in FET transistors, aptamers are a better option because of their smaller size (1-2 nm). Hammock et al.,[129] reported an OFET based sensors for the detection of thrombin. In this device, the recognition element is a thrombin-specific DNA aptamer deposited on the semiconductor as shown in Fig 1.15.

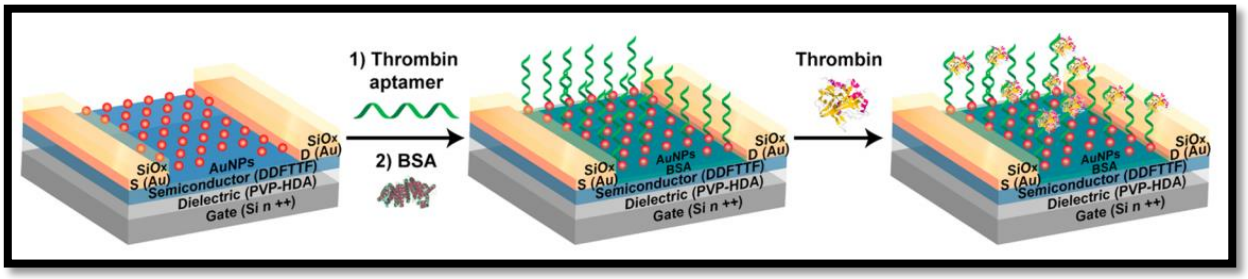

Figure 1.15: *Schematic diagram of the OFET channel functionalization with gold nanoparticles and anti-thrombin aptamers and of the following interaction between aptamers and thrombin in the recognition event. (Adopted with permission from Hammock M.L. et al,[129] © (2013) American Chemical Society)*

Hagen et al.,[130] engineered a Zinc Oxide-FET (ZnO-FET) covalently functionalized with riboflavin binding aptamer on the ZnO semiconductor surface. In all the cases, the typical approach adopted is that the aptameric functionalization is carried out on the active channel of the transistor devices, leaving the gate electrode material as standard.

In our project, we implement the idea that one could exploit the previously described effects of the gate nature on the device properties to explore and optimize the effects of an aptameric functionalization on the gate electrode aiming at optimizing the sensing properties.

1.7 OECTs GATE SELECTION

Gate electrodes in OECTs are typically made of metals such as Ag, Ag/AgCl, Pt, Au[104,120,125,131,132] or patterned PEDOT:PSS films.[121,133,134] Metal gate electrodes, often, leads to higher costs and complicates the OECT fabrication process, requiring the exploitation of new materials.[121] The lowering cost of graphene synthesis together with its interesting physical properties, including fast electron transport, high thermal conductivity, excellent mechanical flexibility and good biocompatibility,[135] make it a very attractive material. Thanks to these unique properties, since its discovery in 2004,[136] graphene was widely used in several fields such as biosensing, flexible and

transparent electronics (OLED), photonics (photodetector and optical modulator), transistors, energy generation and storage, composite materials, paints and coatings.[137]

Graphene is a one-atom–thick crystal of sp^2-bondend carbon atoms arranged in a 2D honeycomb lattice. With this structure, graphene has a strength to weight ratio that outperforms metals and metal composites maintaining a flexible structure, which can forms also different allotropes including nanotubes and fullerenes (Fig 1.16).

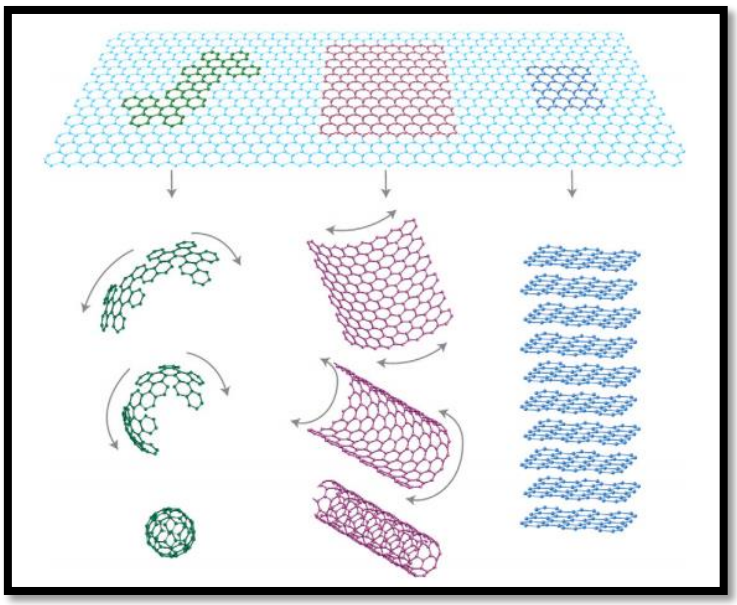

Figure 1.16: *The flexible structure of graphene can be wrapped to form 0D fullerenes, can be rolled into 1D nanotubes and can be stacked into 3D graphite.*

It has a large theoretical surface area (2630 m^2/g), high intrinsic mobility ($2x10^5$ $cm^2/v{\cdot}s$),[138] high Young's modulus (~1.0 TPa),[139] optical transmittance (~97.7%), thermal conductivity (~5000 $W/m{\cdot}K$)[140] and good electrical conductivity.[141,142] A large number of techniques have been developed and improved to synthesize graphene and can be divided in "bottom up" and "top down" methods.[143] In bottom up methods are included thermal or plasma chemical vapor deposition (CVD)[144] and epitaxial growth from silicon carbide.[145,146] Top down approaches include chemical reduction methods,[147] electrochemical synthesis[148] and chemical or mechanical graphite exfoliation.[149,150] Among these, the most widely used technique is the reduction of graphene oxide (GO) prepared by graphite oxide exfoliation.[151152] The quality and the quantity of graphene produced depends on the method chosen, which leads to graphene composed by a different number of layers: from a mono or bi-layers to a few-layers graphene (3 to ~10 layers).[153] Some examples of graphene production are shown in Fig. 1.17, reporting the dependence between the quality of graphene and the cost of

fabrication.

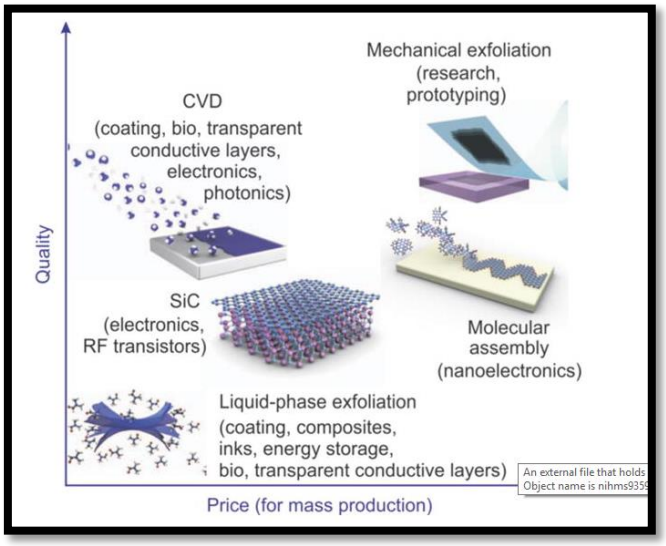

Figure 1.17: *Methods of graphene mass-production. (Adapted with permission from Zhu Y. et al.,*[153]*© (2010) Wiley Online Library)*

In particular, graphene is considered an effective option for silicon replacement, because allows a faster and easier devices fabrication, in fact in the last decade graphene-based transistors have been rapidly developed.[154] A graphene field effect transistor (GFET), has the same FET geometry but, in this case, a graphene channel replaces the silicon one. In contrast to conventional FET, due to the zero-gap of graphene, GFETs cannot switch off with the application of a gate voltage. GFETs, in fact, exhibit ambipolar behavior in which charge carriers change from holes to electrons or vice versa when the Fermi level reaches the Dirac point (where the valance band touches the conduction band). In this point, graphene conductivity is quasi-zero due to a very small number of free carriers at that voltage.[143,155,156]

Another example of the graphene application in transistors technologies is the graphene solution-gated-field effect transistor (G-SgFETs). In this device, the graphene channel is in contact with an electrolyte instead of a gate insulator. The G-SgFET operates in solution with the gate voltage applied on the channel by the gate/electrolyte and electrolyte/graphene interfaces.

Graphene in OECTs, has been used only to modify platinum gate electrode in order to enhance the device sensitivity for glucose[157] and dopamine[120] biosensors, but it has never been used as pure gate electrode. Nevertheless, graphene is a promising platform for sensing biomolecules because of its large surface area, every atom in a graphene layer is a surface atom, and hence molecular interactions and electron transport through graphene can be highly sensitive to absorbed molecules. In addition,

due to good electronic transport and high electrocatalytic activity, electrochemical reactions of analytes are greatly promoted on graphene film leading to an enhanced voltammetric response.[158]

In last decades, there has been increasing interest in investigating graphene surface modifications, because dispersion and functionalization of graphene sheets are of crucial importance to achieve the best performance for their applications.[159] Graphene can be modified through both covalent and non-covalent functionalizations. Generally, non-covalent modifications of the graphene surface are preferred because covalent approaches compromise the sp^2 structure of the graphene lattice leading to defects and a loss of electronic properties. Non-covalent interactions include π-π interactions, electron-donor acceptor complexes, hydrogen bonding and van der Waals forces and lead to a better dispersibility, biocompatibility and reactivity.[160] Different studies show that non-covalent interactions between graphene and metal nanoparticles offer a number of additional unique physicochemical properties and functions.[161–163] By combining these two materials additional synergic properties can be achieved, for example metal nanoparticles modify the local electronic structure of graphene changing its charge transfer behavior. This leads to an enhanced catalyst performance, which can be exploited in sensing applications, because the selectivity and the sensitivity of the graphene-metal nanoparticles based sensors is greater than either graphene or metal nanoparticles based sensors alone.[164]

Moreover, it is possible to use metal nanoparticles, gold nanoparticles (AuNPs) in particular, on the graphene surface as binding sites for several biomolecules, such as proteins, nucleic acids and aptamers. AuNPs, in fact, are widely used to label biological because of their rich surface chemistry, easy and low-cost synthesis and low toxicity *in vivo* giving rise to a several applications in therapeutics and diagnostics. Biomolecules are anchored to gold nanoparticles with physical or chemical interactions including: ionic attraction (typically between negatively charged AuNPs and positively charged proteins at physiological pH), hydrophobic attraction, dative bonding between the gold electrons and the sulfur group in the antibody/oligonucleotidic structure, chemisorption via thiol derivatives, using linkers (polyethylene glycol, PEG) or the interaction streptavidin-biotin.[165]

In this framework aptamers are conjugated on gold nanoparticles by thiolated aptamers. Since the sulfur-AuNPs interaction is in the order of 45 kcal/mol, it is considered as a "semi-covalent" bond, in comparison with covalent carbon-carbon bond strength of 86 kcal/mol.[166] Exploiting this Au-S great affinity it is possible to bind, with high stability, aptamers on the graphene surface using AuNPs as binding sites. [167,168]

In this scenario of a wide range of biosensing possibilities that graphene offers, the innovative

approach of exploiting this material as gate electrode in OECT technology appears very promising and is the main subject of this work.

Moreover, the already mentioned approach involving its conjugation with aptamers through gold nanoparticles paves the way for the establishment of a new class of OECT systems dedicated to the sensing of biomolecules.

In this PhD project, thus the property of OECTs of high amplification transducer was coupled with the already mentioned properties of a multi-layers graphene (MLG) gate electrode decorated with AuNP-aptamers, responsible for the detection, as bioreceptors, of a wide range of target molecules.

The one proposed here is the first aptasensor based on OECTs with graphene gate electrode. In this new and innovative approach, we took advantage of the combination of properties of OECT and of a graphene gate electrode, never tested before, to whom we applied the aptameric functionalization, responsible for the detection, exploring a configuration never tested before.

To test the performances and the reliability of our sensing system, we choose the detection of thrombin as a test bench and validation system.

1.8 THROMBIN-APTAMER INTERACTION

Thrombin was extensively studied since its discovery in the 19th century[169] and continues to be at the core of several biomedical researches.

Thrombin is a serine protease involved in the blood coagulation cascade and it plays an essential role for homeostasis in many physiological systems.[170] It is the only factor capable of converting soluble fibrinogen into insoluble fibrin and promotes a variety of coagulation-related reactions.[171] In absence of efficient and timely thrombin production, stable blood clots cannot form, leading to hemorrhage. Conversely, unregulated thrombin generation results in diffusion of the clot beyond the site of tissue damage, causing thrombosis.[172]

Thrombin was the first biological macromolecule exploited for aptamers selection and nowadays there are two anti-thrombin aptamers (TBA) largely used for its specific detection: the so-called TBA_{15}, possessing 15 bases and TBA_{29} owing 29 bases.[173] The TBA_{15} originally described by Bock et al.[174] can form stable intermolecular G-quadruplex structure, which is in anti-parallel orientation with a chair-like conformation. The TBA_{15} (5′-GGT TGG TGT GGT TGG-3′) interacts with one of

the two thrombin binding sites called the fibrinogen-recognition exosite (exosite I) through its two T-T loops, with a dissociation constant K_d of about 100 nM. The TBA_{29} (5′-AGT CCG TGG TAG GGC AGG TTG GGG TGA CT-3′), having also a G-quadruplex structure, binds the thrombin heparin-binding domain (exosite II) with a greater affinity of 0.5 nM. These aptamers can bind only the α-thrombin, while the β or γ-thrombin cannot be bonded because the exosites I and II are partially of fully lost during the proteolytic cleavage of α-thrombin.[173]

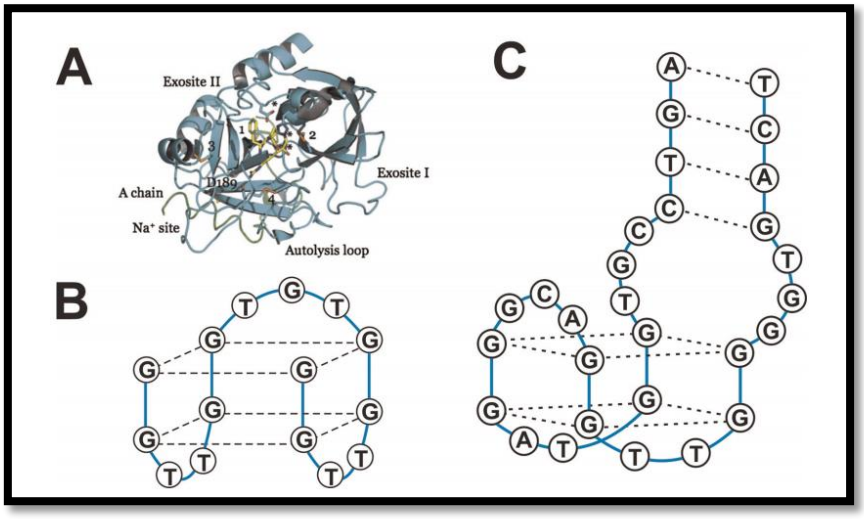

Figure 1.18: *a) thrombin structure in which the two the fibrinogen and heparin sites are reported. b) TBA_{15} and c) TBA_{29} with their G-quadruplex structures. (Adapted with permission from Deng B. et al.,*[173] *© (2014) Elsevier)*

Generally, in electrochemical aptasensors signals can be generated through three different mechanisms: with the introduction of catalytic labels at the electrode, varying the distance of the electrochemical label from the electrode and switching the conductivity of the DNA strand immobilized on the electrode.

The use of catalytic labels includes the use of enzymes and nanoparticles. In the case of thrombin detection, this strategy always requires a sandwich assay format, in which both the two anti-thrombin aptamers (TBA_{15} and TBA_{29}) are employed, exploiting their possibility of bonding the protein in two different domains. Usually, one aptamer acts as capture probe and it is immobilized on the electrode, while the second aptamer is the signal read-out probe, being modified with the catalytic probe. During the recognition event, the formation of the sandwich binding complex brings the label in proximity of the electrode surface leading to amperometric, voltammetric or impedimetric detection.[173] Katakis and al.,[175] reported an example of this mechanism, in which an aptamer was linked to the horseradish

peroxidase (HRP) catalytic label and the second thiolated aptamer was conjugated to a gold electrode. The HRP catalyzed the relay-mediated reduction of H_2O_2 generating an amperometric response.

The second strategy includes electrochemical labels such as methylene blue and ferrocene, which requires proximity to the electrode surface to produce electrical signals. The possibility of switching the aptamers structure during its coordination of the target molecule can be exploited to change the proximity between labels and electrodes. Plaxco and coworkers,[176] engineered a thrombin aptasensor in which one of the two ends of the aptamer, immobilized on the electrode, was modified with methylene blue.

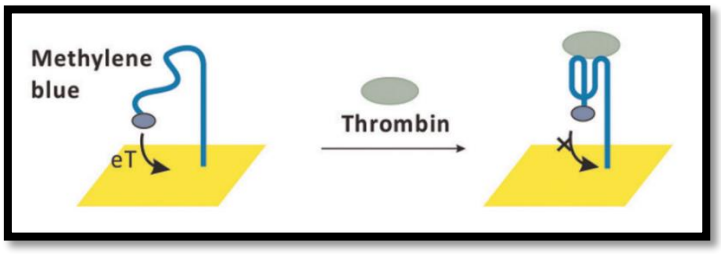

Figure 1.19: *Electrochemical aptasensor for thrombin detection. The possibility of methylene blue to transfer an electron to the electrode surface depends on the aptamer conformation. (Adapted with permission from Deng B. et al.,*[173] *© (2014) Elsevier)*

The operating principle is schematized in Fig. 1.19, in absence of thrombin, the natural aptamer conformation enabled the close proximity of the electrochemical label to the surface electrode, generating a voltammetric response. After the coordination of the thrombin, aptamer assumes the G-quadruplex structure and moves the methylene blue away from the electrode surface shielding their electron-transfer communication.

Since the molecular conductivity of DNA double strands has been shown experimentally to depend on their conformational state,[177] it is possible to develop an electrochemical aptasensor by directly measuring changes in the DNA conductivity caused by its conformational changes during the recognition event. According to this principle, Yu et al.,[178] developed a thrombin sensor by incorporating aptamers into a double-helical conduction path. The latter was formed by a DNA three-way junction and ferrocene was labeled at the strand that encompassed an aptamer sequence. In absence of thrombin, the three-way junction structure does not allow electron transfer between ferrocene and the electrode surface. Upon binding thrombin, the aptamer alters the conformation of the three-way junction allowing the charge transfer between the electrode and the electrochemical label.

Chapter 2

ORGANIC ELECTROCHEMICAL TRANSISTORS

2.1 INTRINSICALLY CONDUCTIVE POLYMERS (ICPS)

Conductive polymers or, more precisely, intrinsically conductive polymers (ICPs) are organic polymers that can carry an electric current along their molecular chain.[179]

For a long time, polymers have been considered insulating materials, in contrast to inorganic solids, which can behave as semiconductors, metals and insulators.

The properties of metals, semiconductors and insulators can be described, according to the band theory, in terms of their electronic structure. In diatomic molecules, the atomic orbitals merge to form molecular orbitals with discrete and well-defined energy levels. The one with lower energy has a bonding character, because electrons in this orbital are mostly located in the region between the two nuclei. The other with higher energy has an anti-bonding character because electrons in this orbital spend most of their time away from the region between the two nuclei. When a very large number of atoms is arranged in a three-dimensional lattice, as in the case of polymers, the atomic valence levels broaden into continuous bonding and antibonding bands.[180]

In order to be electronically conductive, polymers must possess besides charge carriers also an orbitals system allowing the charge carriers to move. From this point of view, a continuous orbital overlapping seems to be necessary for polymers to become intrinsically conducting. In fact, these "synthetic metals" are composed of a conjugated molecular structure with alternating single and double bonds, in which extended π-bonds are delocalized along the polymeric backbone.[181] If the carbon-carbon bonds were equally long, the remaining electrons would be positioned or in a half

filled continuous band or localized in the merging of the highest occupied (HOMO) and the lowest unoccupied (LUMO) π-electron bands. However, Peierls and others have proved that a one-dimensional chain equally spaced with one π electron per carbon is unstable resulting in the so called Peierls' lattice distortion that leads to a bond-alternated structure with lower symmetry.[182] This bond-alternated structure has a repetitive unit with two carbon atoms closer together and the next two carbon atoms further apart. For example, in the case of polyacetylene, the simplest conjugated polymers which was synthesized in 1950 by Natta, the repetitive unit can be described as –CH=CH- instead of -CH-.

The electronic structure result is that the π-band is divided into π- and π*- bands. Since each band can hold two electrons per atom (spin up and spin down), the π-band is filled and the π*-band is empty and they can be described respectively as valance and conduction bands in analogy with inorganic semiconductors. In this way, the energy difference between the highest occupied state in the π-band and the lowest unoccupied state in the π*-band is described as the π-π* energy gap, E_g.

Consequently, since the energy band gap is typically in the range of 1 to 4 eV, conjugated polymers in their pristine state, show very low conductivities. In fact, it is well known that the doping process is a necessary step for electronically conducting polymers.

In 1977 Shirakawa, Heeger and MacDiarmid (Nobel Prize for Chemistry, 2000) produced accidentally conducting polyacetylene when acetylene monomers were doped with bromine and iodine vapors.[183] The resulting electrical conductivity was 10 times higher than the undoped monomers. From that time, increasingly strong efforts have been devoted to increase polymers' conductivity. Generally, a **reversible doping** of polymers can be obtained chemically via a redox reaction with a dopant molecule or electrochemically by charge transfer with an electrode. This is a quite different concept of "doping" that could be misleading with respect to the concept originally used in solid-state physics where doping consists in introducing foreign neutral atoms into a host lattice.[184]

A first option is based on a redox reaction in which the polymer can be partially oxidized (p-type doping) or partially reduced (n-type doping) by an electrons acceptor (e.g. I_2, AsF_5) or an electrons donor (e.g. Na, K) respectively.[75,183]

$$(-CH=CH-)_n + \frac{3x}{2} I \rightarrow (-CH=CH-)_n^+ + I_3^- \rightarrow \text{(p-type doping)}$$

$$(-CH=CH-)_n + xNa \rightarrow (-CH=CH-)_n^{x-} + xNa^+ \rightarrow \text{(n-type doping)}$$

Conjugated polymers can also be easily oxidized (p-doping) or reduced (n-doping) electrochemically with the conjugated polymer acting as either an electron source or an electron sink. The electrochemical doping of the polymer is described by the following formulas:

$(\text{-CH=CH-})_n + [M^+X^-]_{solution} \rightarrow [(\text{-CH=CH-})^y (X^-)_y]_n + [M]_{electrode} \rightarrow$ (p-type doping)

$(\text{-CH=CH-})_n + [M]_{electrode} \rightarrow [(M^+)_y (\text{-CH=CH-})^{-y}]_n + [M^+X^-]_{solution} \rightarrow$ (n-type doping)

The doping reaction can be achieved by applying a current between the conjugated polymer and a counter electrode.[185] Electrochemical doping shows several advantages compared with chemical doping. Firstly, the electrochemical doping allows a precise control of the doping level by simply monitoring the current flown between the two electrodes. Secondly, the transition between doped and undoped forms is highly reversible without requiring chemical products removal. Finally, both p- or n-type doping can be achieved even without introducing dopant species by conventional chemical reactions. In both cases, however, counter ions are introduced for stabilizing the charge along the polymer backbone.

The charges introduced in the polymers via the doping process lead to defects, which are associated to a molecular distortion in the polymer chain. These defects are localized onto the polymer chain and result in novel energy levels in the electronic structure of conjugated polymers including the quasi-particles **solitons**, **polarons** and **bipolarons**.

Solitons are charge carriers that only occur in polymers with degenerate ground state. Degenerate polymers are those where an interchange of single and double bonds along the polymeric chain leads to two geometries with the same energy (Fig 2.1a). Polyacetylene exists in two isomeric forms (*cis* and *trans*): the *trans*-acetylene form is thermodynamically more stable and the *cis–trans* isomerization is irreversible. *Trans*-Polyacetylene (Fig. 2.1b) is the only known polymer with a degenerated ground state due to its access to two possible configurations.[186] Soliton is an unpaired electron (Fig. 2.1c), a radical, at the borderline between two phases with an interchange of single and double bonds. Presence of a soliton leads to the appearance of a localized electronic level in the middle of the band gap. The soliton states can be filled with one electron (neutral soliton, spin ½), with two electrons (negatively charged soliton, spin zero) or empty (positively charged soliton, spin zero) (Fig. 2.1d).[187]

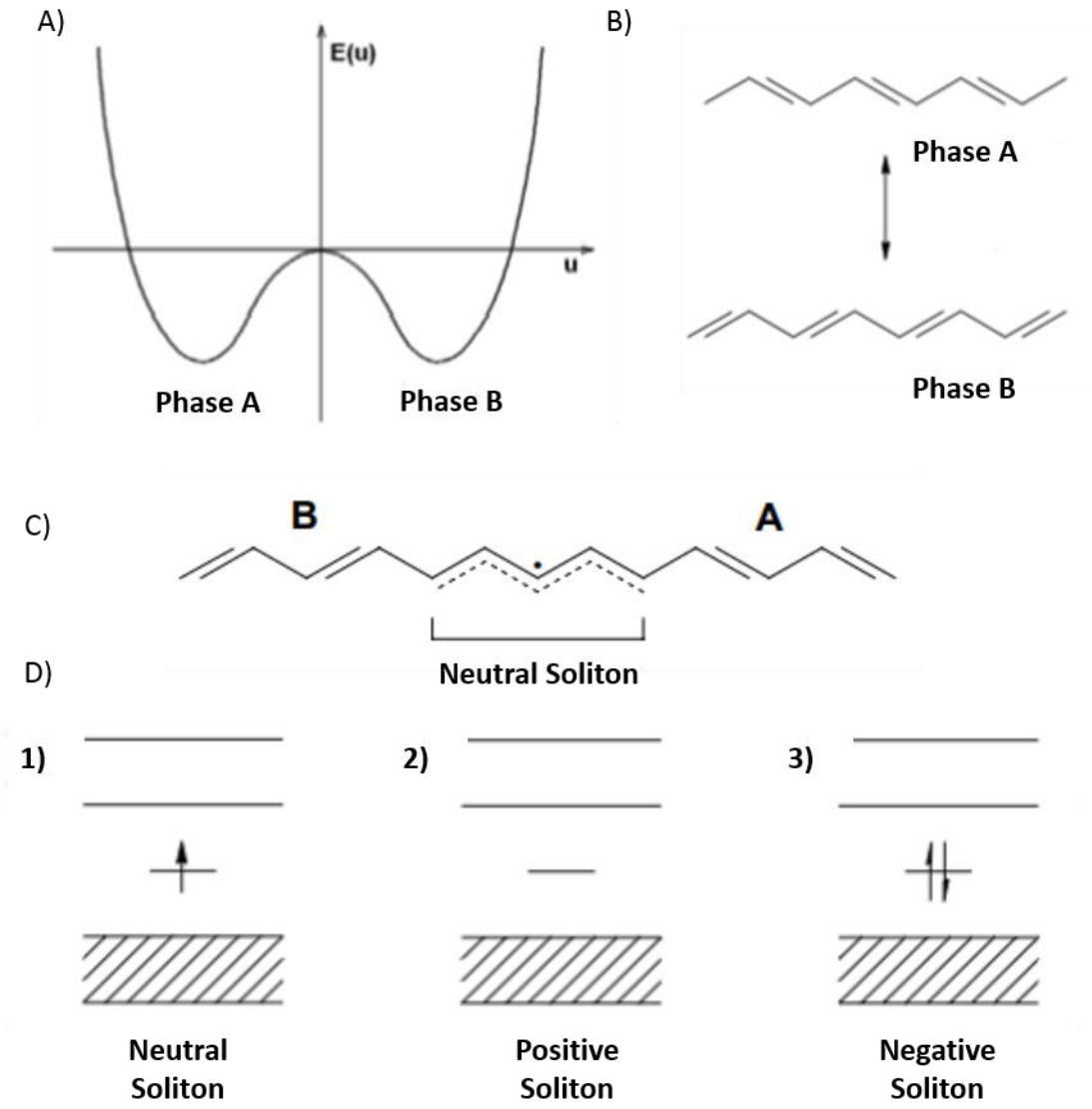

Figure 2.1: *a) Energy levels of a degenerate system, in which the two phase A and B are isoenergetic; b) Phase A and B differ from each other by the position of carbon-carbon single and double bonds; c) Soliton is an unpaired π-electron that it is not localized on one carbon but spread over several carbon atoms; d) The mid-gap is half occupied in the case of neutral soliton (1), empty in the case of positive soliton (2) and double occupied in the case of negative soliton (3).*

Most of conjugated polymers do not have a degenerate ground state and the interchange of the single and double bonds produces energy configurations with local minima and absolute minima levels (Fig 2.1a). Examples are polyparaphenylene (PPP), polypyrrole (PPy) or polythiophene (PT) polymers in which the ground-state geometry corresponds to an aromatic structure with a single-like bond between rings. The second resonance structure is a quinoid-like structure, characterized by a strong double-bond between close rings (Fig. 2.2a). The quinoid form has a higher total energy than the aromatic form (Fig. 2.2b).[188] Addition or removal of an electron from the conjugated polymer results in a chain distortion and the consequent formation of localized defects that move together with the

charge. This combination of an additional charge coupled with local lattice distortion is called a polaron consisting of a tightly bound radical and cation. The formation of polarons causes the injection of states from the bottom of the conduction band and top of the valence band into the band gap. In the case of positive polarons, an electron is removed from the newly created level moved up from the valance band. In the case of negative polarons, the added electron is stored in the newly created level drawn from the conduction band. In both cases, a half-filled level is created with spin ½ (Fig. 2.2c).

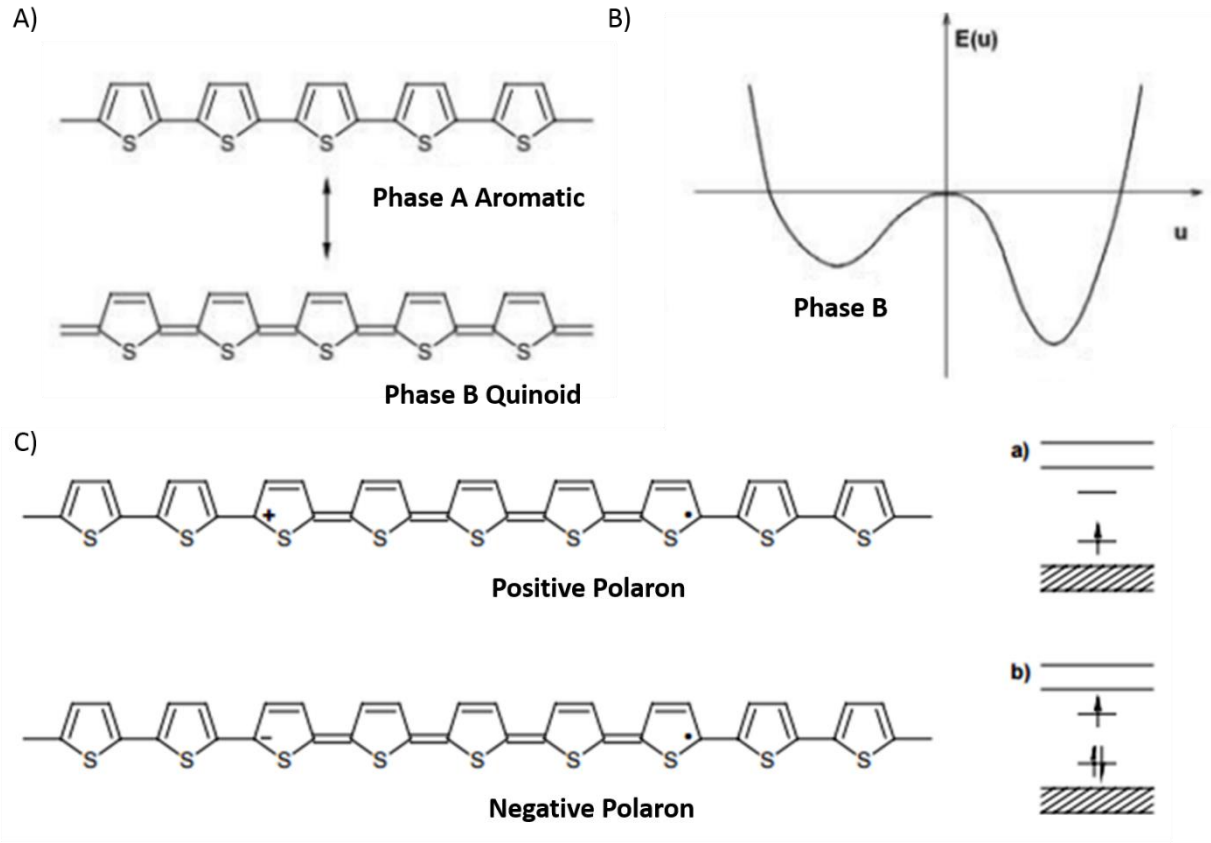

Figure 2.2: *a) Aromatic (A) and Quinoid (B) phases of non-degenerate polymer; b) Energy levels of non-degenerate states: aromatic phase is more stable than the quinoid phase; c) A polaron is a positive or a negative charge coupled with an unpaired electron. For both positive and negative polarons in the mid-gap, there is a half-filled level.*

A further addition of charges to the polymer chain may induce the formation of 2 polarons in close proximity or of a single bipolaron. This latter is an energetically more stable structure in which, despite electrostatic repulsion, two charges might couple. The two free radicals combine, leaving behind two cations separated by a quinoid section of the polymer chain. The higher energy of the quinoid section binds them together, resulting in correlated motion. The net effect is formation of a doubly charged defect acting like a single entity and delocalized over several rings. Bipolarons also

have two levels in the energy gap and in the case of negative bipolarons both levels are fully occupied while for positive bipolarons both levels are empty. In either case, the spin is zero (Fig. 2.3).

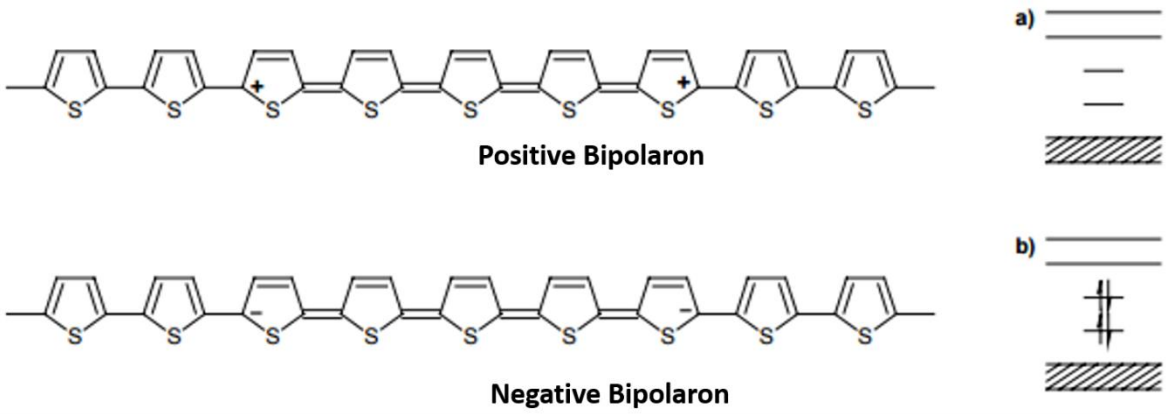

Figure 2.3: *In a positive bipolaron the unpaired electron of the polaron is removed and the levels in the mid-gap are empty; in a negative bipolaron an unpaired electron is added to the polaron and the levels in the mid-gap are full.*

The population of polarons, bipolarons, and/or solitons increases with the increase of the doping level. At high doping levels, additional states are created in the gap until the valence and conduction bands are overlapped in a single band through which electrons can flow.

Good conductivity properties are achieved when these charge carriers can move quite freely along the polymer chain. To correctly understand mechanisms involved in the charge transport in conjugated polymers it is necessary to consider several processes among which charges localization at defects is the major contribution. The different sources of defects in polymers include inhomogeneous doping, sp^3 defects, chain termination, cross link, *cis* segment within *trans* chain, impurities etc.[189] Chemical defects such as non-conjugated carbon atoms inserted in the chain or impurities may result in a local and strong potential and may trap charge carriers. Consequently, the conduction mechanism into conjugated polymers cannot be explained only on the basis of charge transport across the π-system, but also interchain couplings should be included.[190] The main characteristic in the microstructure of polymer materials is the presence of crystals embedded into an amorphous phase that, on the one hand, lowers the crystallinity but at the same time ensures a highly interconnected network. Thus, the macroscopic conduction of charge carriers in a real material demands the movement of charge form one chain to the neighboring chain. The widely used models to explain the transport mechanism of conducting polymers are Mott's variable Range Hopping (VRH)[191] and Fluctuation Induced Tunneling (FIT) developed by Sheng.[192] In VRH model, transport takes place by thermally activated hopping of the charge carriers or defects from one place to another.

In FIT model, where the polymer is described, according to Prigodin and Efetov,[193] in terms of highly conducting regions separated by low conductivity or insulating areas, the conduction mechanism is governed by tunneling between conducting particles and /or phonon assisted tunneling. In this model, it is assumed that charges move freely within a metallic grain but a thermally activated process is required for inter-grain transfer in order to overcome coulombic forces. Generally, hopping across chains due to inter-chain interactions is the most relevant process for the undoped semiconducting polymers, while tunneling between conducting segments that are separated by less conducting regions is most relevant in the case of doped polymers.[192,194,195]

2.2 THE DISCOVERY OF PEDOT

Since its discovery, in 1977, conductive polyacetylene was the most highly conductive polymer known for several years, but its air sensitivity and difficult processability of its doped state, forced researchers to find a way to stabilize the π-electron system. At the beginning, the most promising approach was employing heteroatoms as electron-donor substituents or as polymer chain atoms. The latter has been realized only in polyaniline, while the first solution offered different options like the incorporation of N or S atoms in heterocyclic conjugated structure.[196] Tourillon and Garnier in 1982, first observed a remarkable conductivity of 10-100 S/cm in polythiophene.[197] The real breakthrough was the discovery that oxygen substituents at the 3 and 4 position of the thiophene moiety stabilize the doped polythiophenes with their electron donating properties (mesomeric stabilization).

This gave rise to a new era of stable and highly conductive thiophene based polymers.

At the, beginning, alkoxy-substituted thiophenes had success as monomers for highly conductive polymers[198], but polyalkoxy or polydialkoxythiophenes showed a higher short-term stability against humidity and air oxygen. The solution, surprisingly, was the ring closure of two alkoxy substituents, and hence the EDOT (3,4-ethylendioxythiphene) emerged as the most attractive monomer, whose polymerization generates the high conductive, stable and processable poly-3,4-ethylenedioxythiopene (PEDOT).[199,200]

PEDOT is the most known π-conjugated polymer, mainly because of its good electrical conductivity and electro-optic properties, as well as processability. Historically, PEDOT was prepared using standard oxidative chemical polymerization by the action of iron(III)-chloride.. However this method results in an insoluble powder with a very high conductivity. A solution to the PEDOT insolubility is

the introduction of counterions as salts in the reaction mixture for charging the balancing and solubilizing the polymer. The same approach could be used in electrochemical polymerization methods, where a quite large number of counterions have been used (typically PSS^-, ClO_4^-, BF_4^-, PF_4^-, NO_3^-, SO_4^-, $CF_3SO_3^-$,etc.), in opposition to the very limited number tested for chemically polymerized PEDOT.

Polystyrenesulfonic acid (PSS) was the first counterion used as polyanion to form, through electrostatic interactions with PEDOT (the polycation), a polyelectrolyte complex (PEC) leading to a stable dispersion, compatible with an industrial scale and with several deposition techniques. Nowadays, PEDOT:PSS (Fig. 2.4) dispersions are commercially available under the trend name Clevios™, in which PSS is always used in excess. The weight ratio between thiophene and sulfonic acid groups is in the range of 1:1.25 up to 1:20. These dispersions can be deposited by a wide range of common techniques such as drop casting, spin coating, electrospinning and spraying.[201]

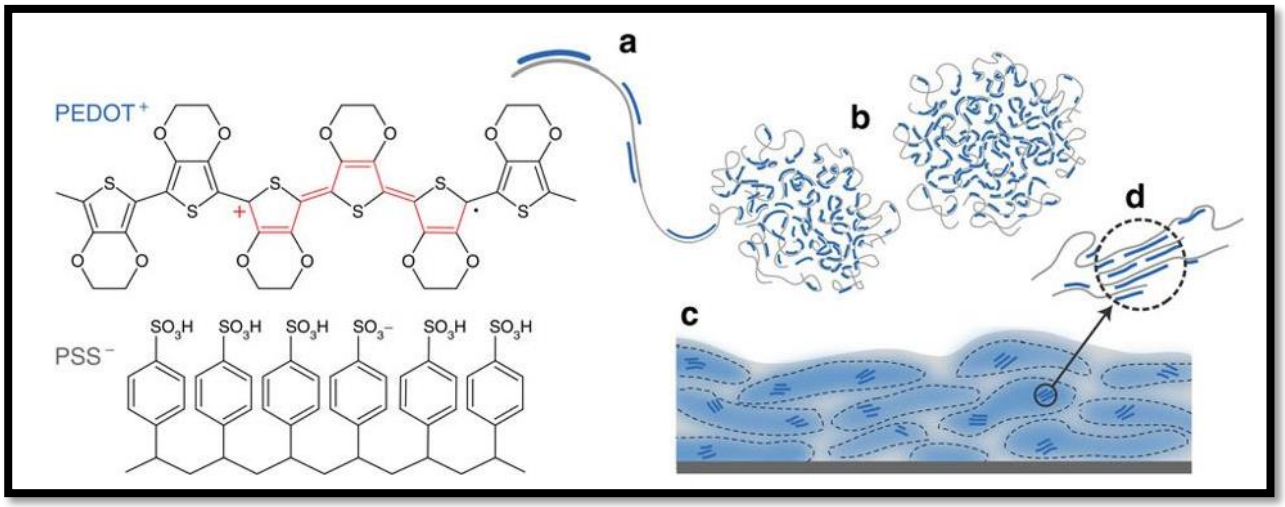

Figure 2.4: *Chemical structure of the organic soluble semiconductor PEDOT:PSS. a) PSS (blue lines) acts as a template during the PEDOT (gray lines polymerization; b) PEDOT:PSS dispersion: hydrophobic cores of PEDOT are surrounded by hydrophilic PSS shell; c) Spin-coated film of PEDOT:PSS; d) Horizontal layers of PEDOT crystal separated by insulating PSS lamellas. (Adapted with permission from Rivnay J. et al.,*[202] *© (2016) Nature Communications)*

PEDOT:PSS has an optical absorbance in the visible spectrum with a peak absorption at around 650 nm which makes the polymer appear bluish. PEDOT:PSS can change color (from transparent to blue) when undergoes a redox reaction between its oxidized and reduced states: this characteristic is common to other conductive polymers and it's known as electrochromism (elektro- and khroma).[203]

The electrical conductivity of PEDOT:PSS ranges between 10^{-3} and 1 S/cm,[204] however charge transport mechanism in PEDOT:PSS is still not fully understood. Generally, the polymer conductivity is influenced by the "macroscopic" morphology of dried particles in the film, which depends on the annealing process and on the distribution of PEDOT segments in the matrix, which is probably determined by the polymerization conditions. In PEDOT:PSS dispersions, PEDOT and PSS form a PEC, where the hydrophobic PEDOT core region is surrounded by a hydrophilic PSS shell, yielding colloidal gel particles which have a micelle structure.[205,206] For spin-coated thin films, the currently accepted morphology, consists of PEDOT-rich clusters organized in horizontal layers and separated by insulating PSS lamellas, as depicted in Fig. 2.4.[207,208] In the normal direction, the separating barriers (the PSS lamellas) are quasi-continuous, whereas the separations in the lateral direction is much less. Because of this strong anisotropy, electrical properties of the polymer cannot be explained within the quantum mechanical Bloch model, one should hence introduce the concept of charge hopping between adjacent sites. PEDOT:PSS conductivity is, therefore, determined by the holes moving from one isolated PEDOT segment to the next, through a matrix of non-conducting PSS. The frequency of charge hopping between adjacent sites depends on its relative energy state, the distance and the relative orientation. The temperature dependence of the conductivity in doped organic materials like PEDOT:PSS has been described in the framework of variable range hopping (VRH)[191] as:

$$\sigma(T) = \sigma(0) exp\left[-(\frac{T_0}{T})^{\alpha}\right] \tag{2.1}$$

where $\sigma(0)$ is the conductivity pre-factor, T_0 is the characteristic temperature and α the exponent that in standard VRH theory is equal to 1/(1+D), where D is the dimensionality of the system. This relationship between conductivity and temperature is typical of strongly disordered inhomogeneous systems[209] and this characteristic comes in also in the temperature dependences of conductivity, which is highly anisotropic in the temperature range of 77-300 K. When the current flows normal ($\perp$) to film, the horizontal PSS lamellas, between PEDOT-rich domains, form thin barriers, which impose more frequent near-neighbor hopping leading to a strongly reduced conductivity. When the current flow is parallel ($\parallel$) to the film, thinner barriers laterally separate PEDOT-rich particles and conduction can take place by 3D VRH. In this way, charge carriers can hop to non-neighbor sites resulting in a conductivity enhancement.[208] Higher conductivity can be obtained with the addition of

high boiling solvent like ethylene glycol or dimethyl sulfoxide,[210–213] of poly-hidroxy compounds such as sorbitol and glycerol[214] or decreasing the pH solution. For example, the highest conductivity was found in a pH range between 0 and 3.[209] Lower conductivity can be obtained increasing the PSS content or by adjusting PEDOT:PSS particles size.

2.3 FROM PEDOT TO OECTS

When H. White and al. reported the fabrication of organic electrochemical transistors (OECTs) in 1984, they described their finding with the following words:[215]

"*We wish to report the fabrication of a chemically derivatized microelectrode array that can function as a transistor when immersed in an electrolyte solution. The key finding is that we have been able to show that a small signal (charge) needed to turn on the device can be amplified. The device to be described mimics the fundamental characteristics of a solid-state transistor, since the resistance between two contacts can be varied by a signal to be amplified*"

Their transistor was a set of tree gold microelectrodes, namely the source, drain and gate terminals, covered with polypirrole, deposited on 1 μm thick SiO_2 grown on <100 > Si. According to White, to work properly, the transistor needs three essential features:

- to allow the flowing of a measurable current between the source and the drain, when the voltage applied between them is significant and the bias applied at the gate is above the threshold (V_T), the three Au electrodes must be closely spaced.
- the polypirrole shows a sharp conductivity when it is oxidized and the potential at which this occurs is V_T.
- when the microelectrode array is covered with a sufficiently amount of polypirrole the individual microelectrodes can be electrically connected by the polymer and driven as one electrode.

For the first time, it was proven that the current between source and drain, which flows through the polypirrole film, can be modulated by the application of a voltage at the gate electrode.

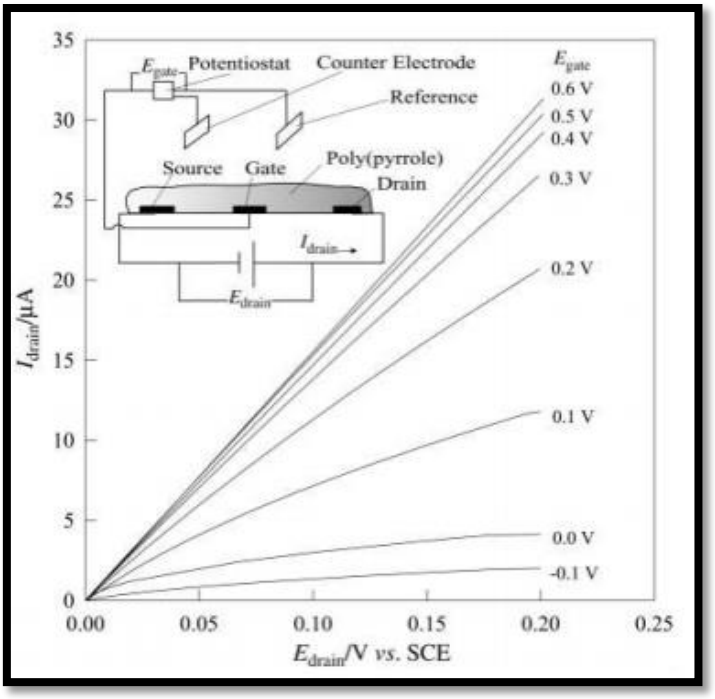

Figure 2.5: *Response of channel current I_{ds} versus the voltage applied between the source and the drain electrodes (V_{ds}) for different values of voltage applied at the gate electrode (V_{gs}); In the inset schematic diagram of White's polypirrole based OECT. (Adapted with permission from White H.S. et al.,*[215] *© (1984) Journal of the American Chemical Society)*

In the typical configuration, OECTs consist of a conducting polymeric film in direct contact with an electrolyte. The polymeric channel is comprised between a couple of metal electrodes (source and drain) and the current measured at a given drain to source voltage (drain voltage, V_{ds}) is called drain current I_{ds}. A third terminal (the gate electrode) is physically separated from the semiconductor by an electrolyte and is used to modulate the current flow inside the channel from the source to the drain electrode, with the application of an appropriate bias, (gate voltage, V_{gs}).[97]

2.4 OPERATING PRINCIPLES

As already mentioned, the application of a voltage between the drain and the source electrode (V_{ds}), causes the flowing of a current through the semiconductor channel. This current I_{ds} is the output current of the OECT and can be modulated by means a suitable gate biasing (V_{gs}). More precisely, when a voltage is applied to the gate electrode, an electric field is generated through the electrolyte whose that drives ions from the electrolyte into the semiconductor channel.

The density of charge carriers in the channel and the effect induced by the injected ions on its conductivity depends on the properties of the semiconductor.

In hole-transporting p-type semiconductors, the application of a positive (negative) gate voltage leads to a decrease (increase) of the channel conductivity while for electron-transporting n-type semiconductors, the effect of the potential sign at the gate electrode acts inversely on the modulation of the current in the channel.

Depending on the operation mode of the polymer, OECTs can also be classified as "depletion-mode" or "accumulation-mode" transistors (Fig. 2.6). Depletion-mode transistors are highly conductive at V_{gs} = 0 V and hence the device is in the "ON" state. By applying an appropriate bias through the gate electrode, the channel become less conductive and the device is switched in the "OFF" state. Accumulation-mode transistors behave in the opposite way.

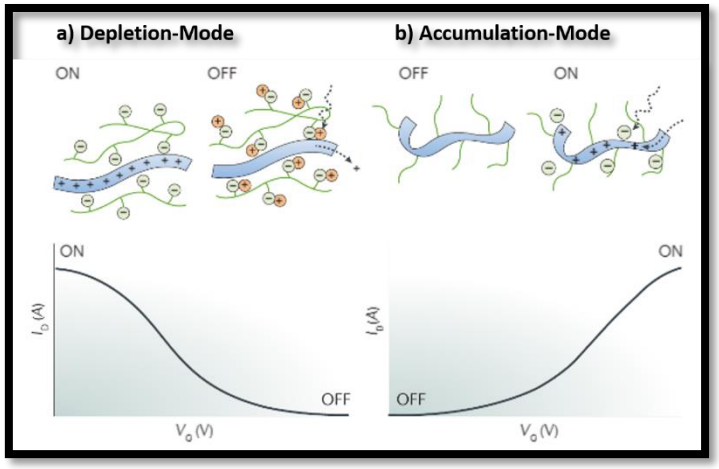

Figure 2.6: *a) OECT characteristic curve showing depletion-mode operation: at zero gate, the device is ON and charge carriers (holes) in the polymer chain contribute to the high drain current. When a positive gate voltage is applied, cations enter in the polymer replacing holes and the device is switched to OFF. b) OECT characteristic curve showing depletion-mode operation: at zero gate, the transistor is OFF and the polymer chain has few mobile holes. When a gate voltage is applied, holes accumulate and compensate injected anions and the transistor is switched ON. (Adapted with permission from Rivnay J. et al.,*[216] *© (2018) Nature Reviews Materials)*

The current state of art for OECTs is based essentially on the p-type semiconductor poly(3,4-ethylenedioxythiophene):poly(styrenesulfonate) (PEDOT:PSS), as active material, a commercially available polymer with high conductivity. Because PEDOT:PSS is naturally in a conductive state, the OECTs using this polymer are classified as depletion-mode transistors.[217]

As already mentioned, PEDOT:PSS is a polyelectrolyte complex (PEC), in which the PSS does not contribute to charge transport directly, but acts as a template to keep PEDOT in the dispersion state and provide film-forming properties.[196] In addition to solubilizing PEDOT, the PSS forms an ionic bond with PEDOT and withdraws electronic charge density giving to the PEDOT positively charged electronic carriers (holes).

Actually, a comprehensive understanding and modeling of OECT properties is still missing and some of devices' features are not fully understood. A direct example is the discrepancy between the existing models for the design of OECT sensors and circuits, and polymer physics. A representative example is the intense debate about the working mechanism of OECTs started with the observation that an electric field, induced by the application of a voltage between source and drain electrodes, affects the conductivity of an intrinsic conducting polymer like PEDOT:PSS, when used in an all-organic field effect transistor configuration.[218]

Nilsson et al.,[97] who created for the first time an organic transistor based on PEDOT:PSS film as the active layer, proposed an electrochemical mechanism to explain the electric field dependence. In their view, the working principle was based on redox reactions between the PEDOT:PSS film and the electrolytes, in which PEDOT:PSS can be switched reversibly between the conducting form ($PEDOT^+$) and the non-conducting state ($PEDOT^0$), according to the following reaction:

$$PEDOT^+ : PSS^- + M^+ \leftrightarrow PEDOT^0 + M^+ : PSS^- + e^- \qquad (2.2)$$

where M^+ are the metal ions supplied by the electrolyte and e^- is the electron transported inside the PEDOT:PSS film. The left side of the equation represents the oxidized state of PEDOT when no voltage is applied at the gate electrode and the device is in its "ON" state. The right side of the equation shows the PEDOT reduction when a bias is applied at the gate electrode, which correspond to the device "OFF" state. Cations are included in this redox equation in order to maintain the charge neutrality in the negatively addressed PEDOT:PSS film.[219]

However, other authors replied to this assumption reporting that the current change of the conducting channel was too slow to be explained by a redox reaction. In addition it was observed that the electric field effect has a temperature dependence and it can be suppressed decreasing the room temperature of 10°C.[220]

Therefore, Hsu et al.[221] proposed that an ion diffusion motion inside the PEDOT:PSS was involved in the observed I_{ds} modulation. With the application of a positive gate voltage, the electric field that arises pushes cations from the electrolyte into the semiconductor channel, which is permeable to ions. These cations form ionic bonds with the PSS, displacing it from PEDOT. Consequently, holes are no longer coulombically stable on the PEDOT backbone so the $PEDOT^+$ is reduced from its conductive state to its insulating neutral state, $PEDOT^0$. Therefore, the inserted ions effectively interrupt the localized states available for the hopping mechanism, causing a conductor-nonconductor transition. According to their research, 0.001-0.1% ionic charges inserted in every three PEDOT rings are enough to change significantly the conductivity of the semiconducting polymer. Approximately the compensation of 2% of holes on the polymer backbone can alter the PEDOT conductance up to three order of magnitude.[221]

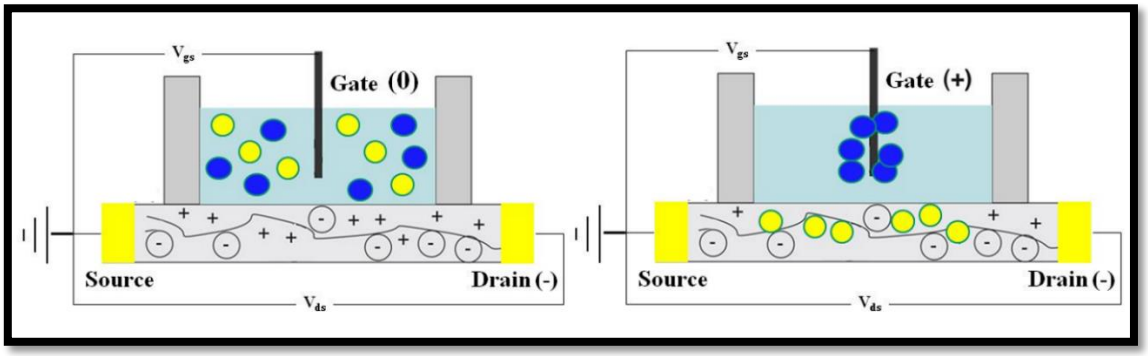

Figure 2.7: *Schematic diagram of an OECT based on a PEDOT:PSS film. When the gate is not biased, the organic polymer is in its conductive state leading to a current flow through the channel. In this situation, the device is in the ON mode. When a positive bias is applied at the gate electrode, cations from the electrolyte solution enter into the channel leading to a loss of conductivity. In this situation, the current through the channel decreases and the device is switched to the OFF mode.*

The transition between a conductive and non-conductive state for a PEDOT:PSS film is a reversible process, so that, when the gate voltage, V_{gs}, is switched back to 0 V, the cations diffuse back out of the channel, and the PSS forms new ionic bonds with the $PEDOT^0$, oxidizing it to its doped and conductive state, $PEDOT^+$. The passage from $PEDOT^+$ to $PEDOT^0$ is considered as a de-doping process while the reversible reaction when the polymer comes back to $PEDOT^+$ is considered as doping process.

2.5 OECTs Behavior Models

As already mentioned, PEDOT:PSS has triggered a great interest in the application of conductive polymers. The main reason is that it combines both ionic and electronic conductivities: in the PEC, the PEDOT domains provide the electrical conductivity (holes transport), while PSS offers ionic transport.[222] The electronic transport is influenced by the density and mobility of the holes, while the ionic transport is determined by the ions in the electrolyte.

Bernards at al[223] proposed a model for explaining some of the device performances. They used the standard treatment of a long-channel depletion-mode inorganic FET modified by incorporating a ionic coupling between the channel and the gate. According this method the OECT is divided into an electronic and ionic circuit.

Electronic Circuit: describe the transport of holes into the conductive polymer between the source and drain terminal. This circuit is modeled by Ohm's law:

$$J(x) = q\mu p(x)\frac{dV_x}{dx} \tag{2.3}$$

Where J is the current flux, q the elementary charge, μ the hole mobility, p the hole density and dV_x/dx the electric field.

Ionic circuit: takes in account the transport of ionic charges in the electrolyte and the interaction of ions with the organic film. A resistor (R_s) and a capacitor (C_d) in series compose this circuit. R_s is related to the conductivity of the electrolyte and is a measure of the ionic strength. C_d accounts for a electrical double layer formed at both the interfaces gate/electrolyte and electrolyte/channel.

Bernards, moreover, proposed a description for the steady state and the transient OECT behavior.

For the **static model** they modified the standard treatment of FET long-channel depletion-mode by incorporating an ionic coupling between the gate and channel.

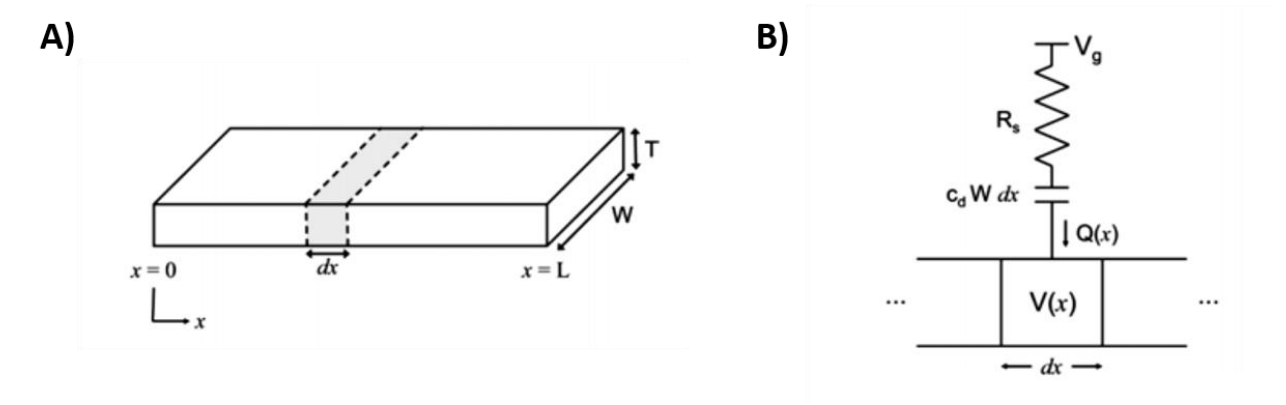

Figure 2.8: *a) Organic film with the source at x = 0 and the drain at x = L (L is the Length, W the Width and T the Thickness of the channel) b) Considering a differential slice of the organic semiconductor, an ionic circuit from the electrolyte is incorporated with the electronic circuit. The resistance R_S represents the ionic strength of the electrolyte while the capacitance c_d is the ionic capacitance per unit area. (Adapted with permission from Bernard D.A. et al.,[224] © (2007) Advanced Functional Materials)*

According to this model, when $V_{ds} < 0$:

$$I_{ds} = \begin{cases} G\left[1 - \dfrac{V_{gs} - {}^{1}/_{2}V_{ds}}{Vp}\right]V_{ds} & for\ V_{ds} \geq V_{ds}^{sat} \quad (2.4) \\ -G\,\dfrac{V_{ds}^{sat\,2}}{2V_p} & for\ V_{ds} \leq V_{ds}^{sat} \quad (2.5) \end{cases}$$

V_{ds}^{sat} is the voltage where the current saturation occurs and is given from the expression:

$$V_{ds}^{sat} = V_{gs} - V_p \quad (2.6)$$

and V_p is the pich-off voltage defined as:

$$V_p = \frac{qp_0t}{c_d} \quad (2.7)$$

where c_d is the capacitance for unit area, which is given by the capacitance of two capacitors in series (gate-electrolyte capacitance in series with electrolyte-semiconductor capacitance), t the thickness of the film and p_0 is the initial hole density in the organic semiconductor before the application of a gate voltage.

G is the conductance of the organic film under zero applied field and is defined as:

$$G = \frac{q\mu p_0 Wt}{L} \quad (2.8)$$

where W and L are respectively the width and the length of the channel.

These equations describe the depletion mode of an OECT when the potential applied between the source and drain electrode is negative ($V_{ds} < 0$). In this regime, a portion of the organic film can be de-doped when the local density of the injected cations become equal to the intrinsic dopant density. When $V_{ds} \leq V_{ds}^{sat}$ (Eq. 1) the semiconductor will be depleted near the drain terminal, when $V_{ds} \geq V_{ds}^{sat}$ (Eq. 2) the depletion region is extended to the source terminal.

The accuracy of this model, however, is limited because Bernards assumes that the OECT channel behaves as an ordered crystalline semiconductor. Actually, as stated above, PEDOT:PSS is a disordered material in which the density of state is very low and the charge carrier gets trapped. An extension of the previous model, was performed by Friedlin at al.,[225] in which they develop a non-uniform mobility model. The current-voltage relationship is the following:

$$I_{ds} = \begin{cases} \dfrac{GV_p}{\frac{E_0}{kT}+1}\left[\left(1-\dfrac{V_{gs}-V_{ds}}{V_p}\right)^{\frac{E_0}{kT}+1} - \left(1-\dfrac{V_{gs}}{V_p}\right)^{\frac{E_0}{kT}+1}\right] & for\ V_{ds} \geq V_{ds}^{sat} \quad (2.9) \\ \dfrac{GV_p}{\frac{E_0}{kT}+1}\left(1-\dfrac{V_{gs}}{V_p}\right)^{\frac{E_0}{kT}+1} & for\ V_{ds} \geq V_{ds}^{sat} \quad (2.10) \end{cases}$$

Bernards at all[223] described also the OECTs **transient behavior**, which is dominated by the injection of cations into the organic film and the removal of holes at the source terminal. This model is useful to study the speed with which the transistor responds to external changes, such as biological signals. According to their assumptions, in which the average voltage drop between the channel and the gate electrode is chosen to ensure that the transient behavior is consistent with the steady-state characteristics. The transient behavior for a simplified OECT is described by the following equation:

$$I(t, V_{gs}) = I_{ss}(V_{gs}) + \Delta I_{ss}\left(1 - f\frac{\tau_e}{\tau_i}\right) exp\left(-t/\tau_i\right) \quad (2.11)$$

Where $I_{ss}(V_{gs})$ is the steady-state source-drain current at a given V_{gs}, $\Delta I_{ss} = I_{ss}(V_{gs} = 0) - I_{ss}(V_{gs})$, f is a proportionality constant for the spatial non-uniformity of the de-doping process. The characteristic f range is from 0 (when $V_{ds} >> V_{gs}$ at $V_{ds} > 0$) to ½ (when $V_{gs} >> V_{ds}$). The electronic and ionic transient time are described by τ_e and τ_i.

The ionic transient time τ_i in the electrolyte depends on the solution resistance and capacitance of the ionic double layer. From Gouy-Chapman theory for double layer capacitance, $\tau_i \sim l/C^{1/2}$ where *l* is the distance between the organic film and the gate electrode and C is the ionic concentration. Therefore, the device time response is improved decreasing the distance between the channel and gate electrode or increasing the electrolyte concentration. The electronic transient time is described by the equation $\tau_e = L^2/\mu V_{ds}$ and it is correlated to the channel length (L) and to the holes mobility (μ). From equation 8, one can approximate the transient response as depending on $\tau_e/\tau_i \sim lL^2/\mu V_{ds}$ and can be varied changing the gate electrode location, the channel length and the drain voltage.

The response to an applied gate voltage can be either a monotonic decay ($\tau_i > f\tau_e$) or a spike-and-recovery ($\tau_i < f\tau_e$) as reported in Fig. 2.9.

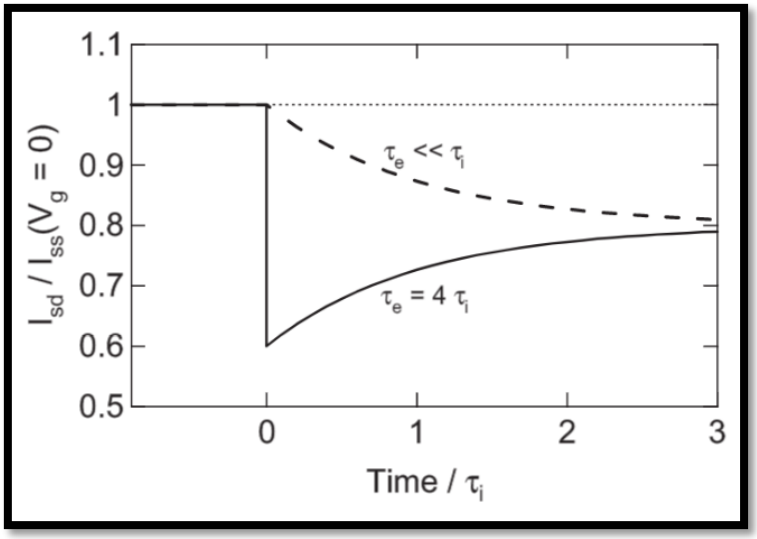

Figure 2.9: *Current transient-behavior for two possible responses according to the relationship between τ_i and τ_e: a monotonic decay response when $\tau_i > f\tau_e$ and a spike-and-recovery response when $\tau_i < f\tau_e$. (Adapted with permission from Bernard D.A. et al.,*[224] *© (2007) Advanced Functional Materials)*

The first decay indicates that the electronic response of the organic film is sufficiently fast to be ignored in the overall transient response and this is the case of devices with small source and drain distance or/and large V_{ds}. A spike-and-recovery is when hole transport in the organic film is relatively slow and holes extraction from the film is the main contribution to the transient current.

2.5.1 Channel geometry and OECTs response

Transconductance is one of the main OECT features that represents a direct measure of the effective

signal amplification. It is defined as the ratio between the change of output current and the input voltage change:

$$g_m = \frac{\Delta I_{ds}}{\Delta V_{gs}} \tag{2.12}$$

This parameter is closely related to the use of OECTs as biosensors, in which it is of crucial importance the transduction of small biological signals.

Unlike FET transistors, where the charge accumulation at the two interfaces determines the current response, in an OECT since the role of the dielectric is directly played by the electrolyte the ions injection into the channel leads to a response dependent on the volume of the polymer also because of the very large porosity/permeability. According to Khodagholy[105], at low frequencies, about 7.8 x 10^{20} ions cm^{-3} are injected into the channel, indicating that the transistor operates close to the limit of complete dedoping.

Transconductance depends on the channel geometry, which is correlated to both the PEDOT:PSS volumetric capacitance and the biasing conditions. In the work,[106] this dependence was described by the following equation:

$$g_m = \left(\frac{WT}{L}\right) \mu C^* \left(V_{th} - V_{gs}\right) \tag{2.13}$$

where V_{th} is the threshold voltage and it is independent by the channel geometry and C^* is the capacitance per unit volume. In the equation governing the OECT performance, the geometry dependence is expressed by the WT/L term and the gate bias offset by $(V_{th} - V_{gs})$.[226]

Bernards et al.,[224] define the ionic transient time as $\tau_i = C_d R_s$, where C_d is the volumetric capacitance, and make clear that the volumetric capacitance also affects the dependence of the response time τ that is hence thickness dependent. C_d scales with film volume and R_s scales with film area. As expected, a thinner channel leads to a faster response but at the same time the I_{ds} decreases and as consequence also the transconductance decreases.[106]

Rivnay et al.,[106] for the first time, measured the electrochemical impedance of PEDOT:PSS films with different volumes. A good fit for the entire set of data was obtained with an equivalent circuit consisting of a capacitor and two resistors. The result is that the capacitance scales with the volume of the film leading to a capacitance per unit volume $C^* = 39$ F/cm^3. The results of Malliaras group,[227] show that the volumetric capacitance of PEDOT:PSS is the quantification of capacitors formed between sulfonate ions and the cations injected, when a de-doping bias is applied. In this

model, the equation that describe the capacitance per unit volume is the following:

$$C^* = \frac{C'_{DL}}{\alpha} \tag{2.14}$$

where C'_{DL} is the capacitance per unit area. This is derived from the Helmholtz model of the electric double layer generated at the interface between a metallic plate and an electrolyte by accumulation of electrons in the first and ions in the latter due to the application of a potential.[228] α is the distance between sites that can host holes in the polymer film. Eq. 11 shows as the density of these sites increases corresponds an increase of the volumetric capacitance.[227]

Volkov et al.,[229] instead, have proposed that PEDOT:PSS volumetric capacitance is an intrinsic property of the polymer and is not due to the formation of capacitor formed between sulfonate ions and the cations injected or to an electrochemical process between the conductive polymer and the polyelectrolyte. According to them, the cyclic voltammetry of conducting polymers can be explained in terms of coupled ion-electron diffusion and migration, without the need of assuming any redox reactions. Elaborating a 2D model, they show that the major contribution to PEDOT:PSS capacitance is originated from charging of double layers formed along the interface between nanoscaled PEDOT-rich and PSS-rich grains in the bulk polymer.

Recently, Berggren confirmed this last hypothesis, whereby the volumetric capacitance is a natural consequence of the polymer structure, in which the electrostatic potential difference between the electronic and ionic material phase, leading to an electrical double layer (EDL) with capacitive characteristics.[230]

2.5.2 Gate Effect on OECTs response

While the effects of the channel geometry on the OECTs response has been widely discussed, the effect of the gate electrode material in determining device performance is still a matter of debate. A theory was elaborated by Tarabella et al,[131] which demonstrates a different effect on the OECT response of two metal wires. Upon the application of the same V_{gs}, Ag gated OECT shows a larger I_{ds} modulation than Pt gated OECT. They suggested that this effect is caused by a change in the OECT operation regime from capacitive, in the case of Pt gated OECT, to Faradaic, in the case of Ag gated configuration. An OECT, in fact, can operate in two regimes depending on the interaction between the gate and the electrolyte.[122,131,133,231] In the capacitive regime, the application of V_{gs} leads to the formation of an electrical double layer (EDL) between the gate/electrolyte interface. In the Faradaic

regime, instead, with the application of V_{gs} a steady-state gate current is generated by a redox reaction between the electrolyte and the gate electrode.[122] In this experiment, the electrolyte was NaCl (0.1 M) and the gate-source current (I_{gs}) was monitored to study the effective operation regime with Ag or Pt as gate electrodes.[231] As shown in Fig. 2.10a for an Ag gated OECT a high steady-state source-gate current is measured indicating the presence of a Faradaic process at the gate electrode. In the case of Pt as gate electrode, the source-gate current is very small indicating that, for a gate small enough to prevent electrolysis of water, there is no charge transfer between the electrolyte and the gate electrode. This last result is consistent with the polarizable nature of Pt electrodes, which leads to the formation of the EDL at the Pt/NaCl interface so $V_{sol} < V_{gs}$. Consequently, the generated potential drop into the electrolyte bulk (Fig. 2.1 b), leads to the induction of a smaller electric field able to inject ions in the channel.[232] Being Ag a non-polarizable electrode no EDL is formed so the absence of a potential drop in the electrolyte means that $V_{sol} \sim V_{gs}$ (Fig. 2.1 b). Since in this case the potential at the electrolyte bulk is equal to the applied potential, leading to an electrical field higher than in the case of Pt-OECTs, in an Ag-OECT the channel current modulation is higher (Fig. 3.1c).

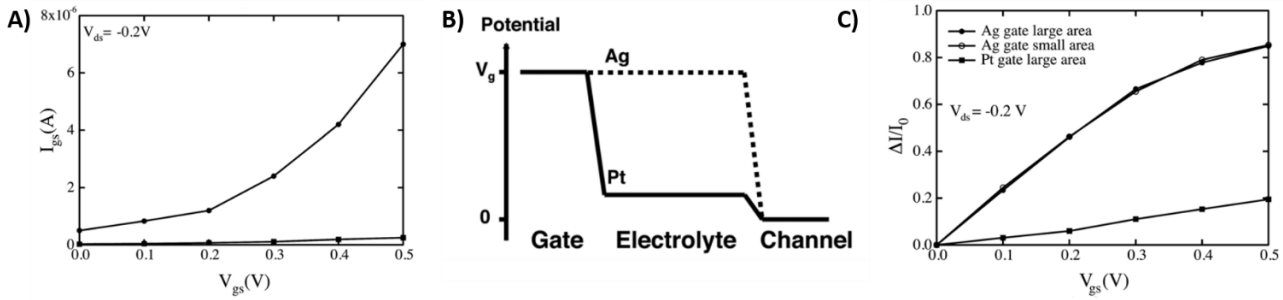

Figure 2.10: *a) I_{gs} vs V_{gs} (V_{ds} cost = -0.1 V) Ag electrode surface is 3.3 mm^2 and Pt surface area is 10.8 mm^2, the I_{gs} of Ag-OECT is bigger than I_{gs} of Pt-OECT. b) Distribution of the potential between the gate electrode and the channel for Ag (dashed line) and Pt electrodes. c) $\Delta I_0/I_0$ vs V_{gs} (V_{ds} cost = -0.2 V), the Ag electrode with surface are of 3.3 mm^2 (large gate) is compared with a smaller Ag electrode with a surface area of 1.62 mm^2 (small gate). The response of the Ag-OECTs is the same regardless of the surface area of the silver electrode. This observation supports the hypothesis of the presence of steady-state source-gate current due to redox reactions between the gate and the halide electrolyte: Ag + X^- ↔ AgX + e. (Adapted with permission from Tarabella G. et al,*[131] *© (2010) Applied Physics Letters)*

The OECTs sensing mechanism was proposed by Lin et al.[233] staring from Bernards[224] model of the dependence of the channel current I_{ds} on the voltage gate V_{gs} with the following equations:

$$I_{ds} = \frac{q\mu p_0 tW}{LV_p}\left(V_p - V_{gs}^{eff} + \frac{V_{ds}}{2}\right)V_{ds} \qquad when\ |V_{ds}| \ll \left|V_p - V_{gs}^{eff}\right| \tag{2.15}$$

$$V_p = {qp_0t}/{c_i} \tag{2.16}$$

$$V_{gs}^{eff} = V_{gs} + V_{offset} \tag{2.17}$$

where c_i is the capacitance for unit area, which is not only related to the capacitance formed between the electrolyte and the PEDOT:PSS film (C_d) but also to the capacitance at the interface between the electrolyte and the gate electrode (C_g). q is the charge, p_0 the initial hole density in the conductive film, μ the hole mobility, t, W and L are geometric parameters of the organic polymer, V_p the pinch-off voltage, V_g^{eff} the effective gate voltage applied and V_{offset} an offset voltage at the interface, depending on the potential drop at the two interfaces: gate/electrolyte and electrolyte/channel. As mentioned before, the formation of a double layer between the electrolyte and the gate electrode interface is related to the gate material, while in the case of the double layer between the electrolyte and the channel is related to the insolubility of PEDOT:PSS in aqueous solution and its permeability.[120,234]

The OECTs sensing mechanism is based on the change of the potential drop across these two interfaces caused by the effect of analytes.[233]

In case of electrochemical reaction occurring at the gate electrode, the voltage applied at the double layer near the channel is given by:

$$V_{offset} = A + \frac{kT}{ne}\ln[M^{n+}] \tag{2.18}$$

where A is a constant, k the Boltzmann's constant, T the temperature, n the number of electron transferred in the electrochemical reaction, e the electron charge and $[M^{n+}]$ is the electrolyte cations concentration.[234]

For an Ag gate electrode, as stated above, there is no capacitance at the gate electrode so the gate voltage becomes directly applied to the interface between the PEDOT:PSS and the electrolyte. Lin et al,[234] during the development of an ion-sensitive OECT, demonstrated the possibility of having the same channel current modulation by increasing the ions concentration in the electrolyte and lowering the applied gate voltage. This horizontal shift shows a Nernstian relationship with the cations concentration For Au and Pt gate electrodes, no charge transfer reaction occurs while a double layer is generated between the gate electrode and the electrolyte. The total electrical configuration can be schematized as a series of capacitors including the contribution between gate and electrolyte (C_g) and the capacitor between the polymer and the electrolyte (C_d). The effective capacitance c_i is:

$$c_i = \frac{(C_g C_d)}{WL(C_g + C_d)} \tag{2.19}$$

The capacitance C_g depends on the nature of the polarizable electrode and could hence modulate the OECT response. Generally, for polarizable electrodes, the gate voltage is only partially applied to

the interface between the channel and the electrolyte. For this reason, a higher gate voltage is needed to compensate the drop at the gate/electrolyte interface and at the electrolyte/polymer interface. This latter can be modulated changing the electrolyte cations concentration. The offset voltage for device with polarizable electrode is hence given by:

$$V_{offset} = A' + (1 + \gamma)\frac{kT}{ne}\ln[M^{n+}] \tag{2.20}$$

$$\gamma = {C_d}/{C_g} \tag{2.21}$$

A' is a constant and γ the ratio between C_g and C_d. Since the two capacitances depend on the effective voltage applied on the double layers, γ is not a constant.[234]

2.6 OECTs FABRICATION

One of the advantages of organic materials like PEDOT:PSS is the possibility of process them in a wide range of conditions. The opportunity of tuning molecular structure through organic synthesis can be exploited to control a wide number of processing/deposition parameters, including solubility, functionality, stability, melting point or sublimation temperature. These features gave rise to cheap, high-throughput methods for device manufacturing. The entire manufacturing process can be divided in two stages. The first step is the definition of the channel geometry (length L and width W) by pattering the source and drain electrodes with a highly conductive material. For PEDOT:PSS based transistors, gold is the metal of choice due to its work function which is slightly above the HOMO level of the conducting polymer allowing a low contact resistivity and a more efficient holes injection.[235] In the second step, the conducting polymer is deposited over the source and drain terminals forming the transistor channel.

The first stage of pattering is a crucial part in the OECTs fabrication. PEDOT:PSS must be confined in the channel region to avoid leakage and to reduce cross-talk to achieve better device performance. The selection of the channel size must be done according to the specific application. Nowadays, the target is to reduce the channel to cellular dimension (1-10 μm) to interface with single electrically active cells[236] and to have a fast response down to 100 μs time constant.[237] As mentioned before, smaller is the distance between the drain and source electrode (channel length), higher is the current output and faster the transistor switching speed.[105,122]

Optical lithography is a conventional technique for pattering microelectronic and photonic devices. This method can be performed in two different way: the *top-down* or *subtractive* approach in which PEDOT:PSS is first deposited on a substrate and subsequently patterned, and *bottom-up* or *additive* approach where PEDOT:PSS is spin coated on pre-patterned layout. In both cases, the pattern is transferred to the film from a mask using a photoresist that can react in different ways after the exposition to the UV-light depending on its chemical structure. A positive photoresist can be removed, after the light exposition, by a developer (typically an alkaline solution), while a negative photoresist is insoluble in the developer and cannot be removed. The incompatibility of most of organic materials with conventional lithography solvents used for the deposition, the development and the removal of the photoresist leads to negative effects including dissolution, cracking, swelling, and delamination. A solution to this problem is the use of parylene-C to protect the organic film during the deposition and the development of the photoresist and from solvents, strong acids and bases.[238] Nevertheless, even thogh photolithography is quite expensive, is still a technique of choice because can achieve 100 nm resolution.[239]

Printing processes have generated much interest for industrial applications since they allow a flexible, easy and low-cost fabrication into large area and different substrate (e.g. paper or plastic). *Screen-printing* involves squeezing a specially prepared ink through a screen mask onto a substrate surface to form the desired pattern and print all the active components of an OECT.[240,241] Components of OECTs can also be deposited using ink-jet printing, which delivers small droplets of polymer solution to selected places on the substrate and is similar to the operation of a conventional ink-jet printer, but uses specially formulated inks.[242]

These techniques, however, have limited feature size resolution, 75 μm in the case of screen-printing and 25 μm in the case of ink-jet and both require specially formulated inks and non-standard equipment.

During the OECTs fabrication, before the PEDOT:PSS deposition, which can be performed with several techniques like drop casting, spin coating or spray coating, the PEDOT:PSS can be enriched with different components in order to improve its features. The cross-linking agent 3-glycidoxypropyltrimethoxysilane (GOPS), is used to improve the film mechanical stability and its adhesion to the substrate. GOPS, in fact, prevent delamination and eventual re-dispersion of the conducting film when is exposed to water or other polar solvents and during the washing step.[243,244] The surfactant dodecyl benzene sulfonic acid (DBSA) is widely used as additive to facilitate film processing from PEDOT:PSS suspensions.[245] This also affects positively the conductivity but for

concentration higher than 0.5% v/v can induce a phase separation in the mixture which results in poor film quality.[214] Ethylene glycol (EG) and dimethyl sulfoxide (DMSO) can be used as conductivity enhancing agents to achieve high film conductivity. The role of these co-solvents is still under debate. Kim et al.,[213] proposed that EG or DMSO, with a screen effect, reduce the coulombic effect between $PEDOT^+$ and PSS^- enhancing the charge carrier hopping rate and the conductivity of the film. According to Inganas et al,[246] instead, the co-solvents can aid the reorientation of PEDOT:PSS chains during the baking process to form more connection pathway between $PEDOT^+$ chains.

Chapter 3

MATERIALS AND METHODS

3.1 OECTs FABRICATION

OECTs have been fabricated on a 2-in. circular-shaped and flexible Kapton substrate (DuPont) (Fig. 3.1 a). Source and drain electrodes, made of a Ti(20 nm)–Au(100 nm) bilayer, were deposited by sputtering using a Kurt J. Lesker PVD 75 DC Magnetron Sputtering. The Ti/Au bilayer was then patterned by lift-off technique (image reversal AZ 5214E photoresist followed by dimethyl sulfoxide, DMSO Sigma Aldrich, bath at 60 °C), determining a 100 µm long (L) and 6 mm wide (W) device channel (Fig. 3.1 b). To improve the PEDOT:PSS performances, a mixture of PEDOT:PSS (Clevios PH1000), ethylene glycol (20:1 in volume, Sigma Aldrich) and DBSA (0.05%, Sigma Aldrich) has been spin-coated on several substrates including Kapton (Fig. 3.1 c) resulting in a 20 nm-thick film. The spun film has been annealed at 150 °C in vacuum for 90 min. To pattern the as-prepared film, a procedure described elsewhere has been followed;[247] briefly, a 150 nm-thick Ag layer has been deposited using an ULVAC EBX-14D electron beam evaporator and subsequently patterned by a wet etching (E6 Metal Etching, 16 V H_3PO_4 (85%) : 1 V HNO_3 (65%) : 1 V CH_3COOH : 2 V H_2O) at room temperature (Fig. 3.1 d). Finally, the PEDOT:PSS excess has been removed using a O_2 plasma (100 mTorr, 50 sccm, 100 W, 13.56 Hz) for 30 s and the residual Ag protective layer has been removed by the aforementioned E6 wet etching, defining in this way the PEDOT:PSS-based device channel (Fig. 3.1 e-f). A Sylgard 184 poly(dimethylsiloxane) (PDMS, Sigma Aldrich) well has been set on the channel to contain the electrolyte solution (Fig. 3.1 g).

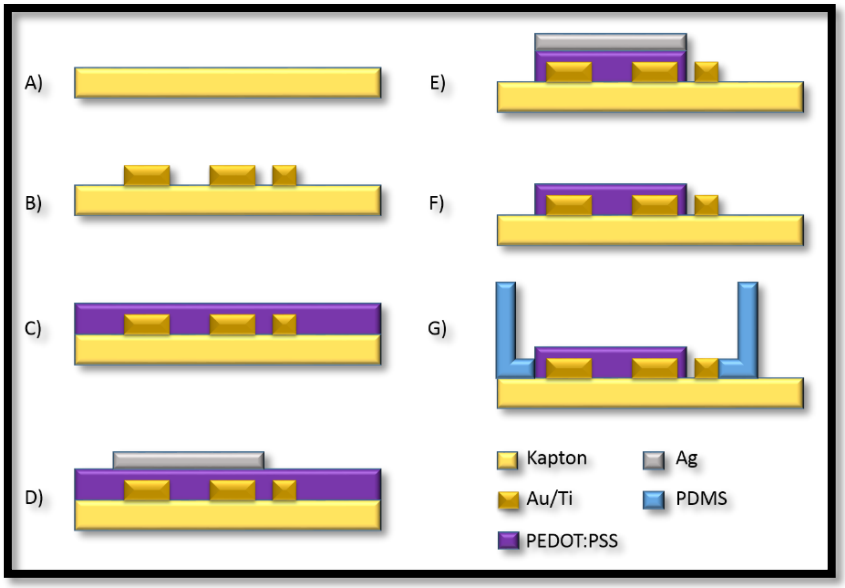

Figure 3.1: *Schematic diagram of OECTs fabrication steps.*

3.2 Graphene Gate Electrode Fabrication

The graphene gate electrodes consist of conductive multi-layers graphene (MLG) deposited on a flexible and insulating substrate made of low-density polyethylene (LDPE) film. The preparation of polyethylene multi-layers graphene (PMLG) films follows the procedure reported by Carotenuto and coworkers.[248] Briefly, PMLG films were produced through exfoliation of nanographite through thermal and ultrasonic treatments ensuring mechanical lamination of the material. The obtained powder has been suspended in an alcoholic solution and deposited on LDPE surface by means of a drop casting method. The gate electrodes were fabricated cutting rectangular shaped sheets (5x10 mm) from the PMLG film.

High-resolution scanning electron microscopy (ZEISS field emission gun scanning electron microscope) and Raman spectroscopy (Renishaw Invia Qotr) were performed to characterize the properties of the graphene surface of the PMLG film. SEM characterization was carried out with 15 keV acceleration voltage of the electron beam and 2.8 mm working distance. The Raman spectra were collected with a 532 nm excitation laser, 50X objective, 0.5 mW of laser power, 10s of acquisition time and two acquisitions per spectra. The Raman maps were acquired with similar parameters on an area of 20 µm x 18 µm with a spatial resolution of 500 nm.

3.3 OECTs DRIVEN BY PMLG GATE ELECTRODE: ELECTRICAL CHARACTERIZATIONS

The transistor response when PMLG is used as gate electrode, was studied by performing OECTs electrical measurements including the so-called output, sensing and transfer curves. With the aim of using these devices in biological applications, all these characterizations were made in PBS (phosphate buffered saline) pH 7.4 10 mM, which is the buffer solution commonly used in biological research, because of its similarities (salts concentrations and pH) with physiological solutions.[249]

The OECT's performances with the PMLG gate electrode were tested with two source measure units (National Instruments PXle-4138/9) and a 2-channel-source-meters precision unit (Agilent B2902A) controlled by a customized *ad hoc* LABVIEW code. The PMLG-LDPE gate electrode was set horizontally, parallel to the polymeric channel and directly in contact with the electrolyte solution, as shown in Fig. 3.2. During all characterizations, 200 µL of the chosen electrolyte was confined on the top of the PEDOT:PSS channel in a PDMS well. This latter was replaced systematically after each measurement in order to exclude the any possible contribution due to the electrolyte evaporation. This measurement routine was applied in all the experiments performed in this PhD project.

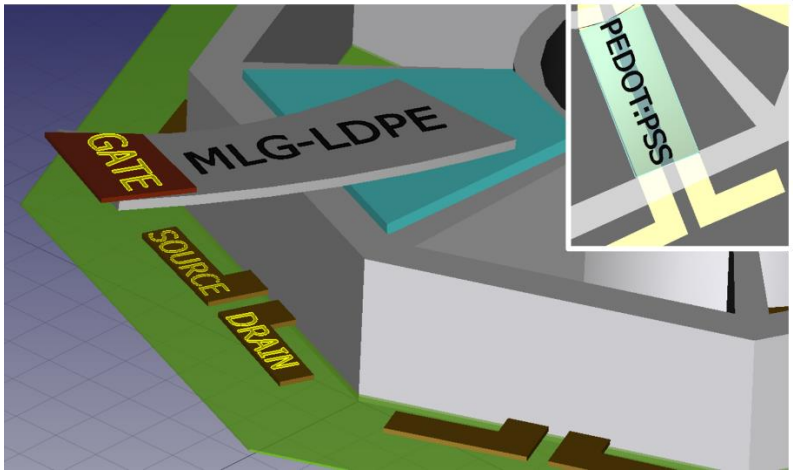

Figure 3.2: *Gold electrodes (Source and Drain) are evaporated on the Kapton film while the Gate electrode (MLG-LDPE) is in physical contact with the liquid electrolyte (blue in figure). The polymeric layer of PEDOT:PSS is deposited between the source and the drain electrodes (inset) forming a conductive channel of about 0.2 x 6 mm.*[250]

Standard characterizations of the OECT response begins with the so called **output curves** in which the current flowing in the PEDOT:PSS channel (I_{ds}) is measured while the voltage applied between

the source and the drain electrodes (V_{ds}) is varied from 0 to -0.6 V, with a step of 0.05 V and a holding time of 5 s. During this negative scan of the V_{ds}, the voltage applied between the gate and the source electrodes (V_{gs}) was kept constant. Different values of V_{gs} have been investigated, from 0 to 1 V with step of 0.1 V.

A study of the role played by the holding time was achieved in the **sensing curves**, in order to evaluate the time of constant V_{gs} application needed for achieving the saturation of I_{ds} modulation and the proper application time in our system. In these experiments the I_{ds} (measured at a fixed values of V_{ds}) was recorded against time, while the V_{gs} is varied in the range of 0 and 1 V, with step of 0.1 V. Between each steps, V_{gs} is brought back to 0 V for the same amount of time and different holding time were studied: 1, 2, 5, 10 and 20 s.

After these preliminary tests, a characterization called **transfer curves** was performed. In this type of measurement, I_{ds} current was recorded by the constant application of a fixed value of $V_{ds,}$ as a function of the V_{gs} modulation varied between 0 and 1 V, with steps of 0.01 V and a holding time of 5 s.

Since the main components of a 10 mM PBS buffer solution are sodium chloride (NaCl) and sodium phosphate, in concentration of about 10 mM and 1 mM respectively, we decided to acquire transfer curves, considering aqueous solutions of these two salts as electrolytes in order to study independently the effect of each single salt on the transistors response.

Furthermore, the behavior of PMLG OECTs in PBS 10 mM has been compared with the response of OECTs driven by gate electrodes made of silver (Ag) or gold (Au) wires in the same electrolyte. For this experiment, transfer characterizations were performed with the same parameters previously discussed.

3.4 Synthesis and Characterization of Gold Nanoparticles

Gold nanoparticles (AuNPs) were synthesized according to the procedure reported by Frens.[251] To obtain spherical AuNPs with a diameter of about 16 nm, a solution of tetrachloroauric acid $HAuCl_4$ (50 mL of 10^{-2}% p/p, **solution I**) and a solution of sodium citrate Na_3-citrate (10 ml of 1% p/p, **solution II**) were prepared. **Solution I** is heated with vigorous magnetic stirrer, once it reaches the boiling point (~ 100 °C) 1 mL of **solution II** is added. During the nucleation process, the solution appears blue, while at the end of the reaction the solution assumes a bright red color corresponding

to the formation of monodisperse spherical gold nanoparticles. The tetrachloroauric acid reduction by sodium citrate is complete after five minutes of reaction at the boiling temperature.

3.4.1 Characterization of the AuNPs

In order to eliminate impurities and nanoparticles aggregates from the solution, the AuNPs suspension has been centrifuged with centrifuge (Rotina 380, Hettich) at a speed of 12000 rpm for 20 minutes at room temperature and putting 1.5 ml of AuNPs solution in an Eppendorf. After the centrifugation the supernatant has been eliminated and the seated colloidal was re-suspended with 1 ml of Milli-Q water (> 18.0 MΩ cm). The AuNPs dispersion has been stored in the dark at room temperature for a maximum of one month time.

To study the surface plasmon resonance of the freshly synthesized AuNPs, a Uv-vis spectrum has been collected using a standard Thermo-Fisher system by scanning the wavelength of a diluted nanoparticles suspension in the range between 350 nm and 1100 nm.

The size and shape of AuNPs have been evaluated using a transmission electron microscope, JEOL JEM 2200 EX, at an accelerating voltage of 200 kV. The samples were prepared by evaporating a drop of gold colloids onto dedicated carbon-coated copper grids and allowing it to dry in the air. The histogram of the particles size distribution and the average diameter was obtained by measuring a batch of 500 AuNPs using ImageJ Fiji Software.

The hydrodynamic diameter distribution of the AuNPs in solution has also been determined by using the DLS (Dynamic Light Scattering) technique. The DLS measurements were carried out with a 90 Plus Particles size Analyzer from Brookhaven Instruments (Holtsville, NY) set-up with a 1.2 mW HeNe laser as light source, a scattering geometry at 90° in 2Θ and S polarization. The detector is a single mode fiber coupled avalanche Geiger module (SensL) with a time resolution of 60 ns. The single photon signal was correlated with a 480 ns resolution correlator. Each sample was allowed to equilibrate for 10 minutes prior to starting the measure and five independent measurement of 60 s duration were performed, and their average values were reported. The samples were prepared by dilution with MillQ water in order to obtain a final concentration of AuNPs close to 100 µg/mL.

The charge state was studied by the Zeta potential method using a Zeta Plus from Brookhaven Instruments (Holtsville, NY) operating at applied voltage of 4 V and minimum 4 run of ten cycles per samples were performed to ensure measurement repeatability, the final zeta potential value was the average of the four runs.

3.5 AuNPs Electrophoretic Deposition

The electrophoretic deposition (EPD) method has been performed to deposit AuNPs on the PMLG gate electrode surface with two source measure units (NI PXle-4138/9) controlled by a customized LABVIEW code. Before the EPD, the PMLG gate electrode was sonicated in isopropanol for 10 minutes to clean the electrode without damaging the graphene surface. The PMLG electrode (5 x 10 mm) was immersed into the AuNPs suspension and was used as anode, together with a chrome electrode (5 x 10 mm) used as cathode. The two electrodes were placed at a distance of about 1 cm and a voltage of 40 V was applied between anode and the grounded cathode, for 15 minutes at room temperature. At the end of the EPD the PMLG gate electrode resulted decorated with AuNPs (AuNPs-PMLG) and it was rinsed three times with Milli-Q water (> 18 MΩ cm) and was allowed to dry in the air.

3.5.1 AuNPs-PMLG gate electrode characterizations

To investigate the morphology of the AuNPs and the quality of the thin film deposited on the PMLG electrode surface a high-resolution scanning electron microscopy (ZEISS field emission gun scanning electron microscope) has been performed. SEM characterization was obtained with 5 keV acceleration voltage of the electron beam at 3.9 mm working distance.

The AuNPs-PMLG gate electrode has been also characterized by Energy dispersive X-ray spectroscopy (EDX) performed with a JEOL 2200FS microscope working at 200 KeV, in order to study the graphene nanocomposite surface coverage. The PMLG surface has been investigated by scanning the SEM electron beam over the area of interest and simultaneously acquiring the EDX spectrum, in order to reconstruct the spatial distribution of the C and Au signals.

Finally the OECT response with the AuNPs-PMLG gate electrode was evaluated acquiring a transfer curve (V_{ds} at -0.25V, and V_{gs} modulation varied between -0.2 and 0.8 V, with steps of 0.01 V and a holding time of 5 s). Also in this case 200 µl of electrolyte (PBS 10 mM) was confined on the top of the PEDOT:PSS channel in a PDMS well and the PMLG-LDPE gate electrode was set horizontally, parallel to the polymeric channel and directly in contact with the electrolyte solution.

3.6 Optimization of the Aptamers Concentration

The thrombin binding aptamers (TBA-15) used in this thesis as bioreceptor elements were purchased from and synthesized by the BIOMERS (Germany) with the following sequence 5' Fc-G-G-T-T-G-G-T-G-T-G-G-T-T-G-G- C_6-SH 3'. The C_6-SH at the 3' end is a thiol group separated from the oligonucleotides sequence by a linear chain of six carbons, while the Fc at the 5' end is a Ferrocene molecule, covalently linked to the aptamers sequence and it is used as redox label.

3.6.1 Aptamers Preparation and Adsorption

The first step of the analytical procedure for the aptasensor fabrication consists in the immobilization of the aptamers onto the AuNPs-PMLG gate electrode surface using a wet physical absorption procedure. To do this, solution of aptamers with different concentrations (0.1, 0.2, 0.4, 1, 5 and 10 µM) have been prepared in sterilized water and 10 µl. Each sample has been heated at 90 °C for 5 minutes to promote to loose the aptamers conformation. The samples were successively dipped in a bath of cold water for 15 minutes to block aptamers in the new conformation. Each sample was then drop casted on the surface of an AuNPs-PMLG gate surface and let dry at room temperature for 4 h. Finally, the as prepared TBA-15 modified AuNPs-PMLG gate electrode has been washed twice with sterilized water, in order to remove the unabsorbed aptamers. .

3.6.2 Blocking the Gate Electrode Surface

After aptamers immobilization, each gate electrode has been dipped in a solution of 6-mercapto-1-hexanol (MCH) (purchased by Merck, Germany) having a concentration of 100 mM for 15 min at room temperature with soft stirring to minimize he eventual un-specific adsorption caused by AuNPs not coordinated with aptamers . Two washing steps with sterilized water followed this procedure.

3.6.3 OECTs driven by TBA_{15} modified AuNPs-PMLG Gate Electrode

OECT response with the TBA_{15}-AuNPs-PMLG gate electrode was evaluated using the same method already explained in section 3.5.1 AuNPs-PMLG gate electrode characterizations, (a transfer curve with V_{ds} at -0.25V and V_{gs} modulation between -0.2 and 0.8 V, with step of 0.01 V and a holding time of 5 s).

An X-ray photoelectron spectroscopy (XPS) study has been performed to verify the formation of the gold-thiol bonds between aptamers and AuNPs on the PMLG gate electrode surface. Photoelectron spectra were recorded with an ESCA system Surface Science Instruments SSX-100. The chemical analyses and the elaboration of the obtained spectra were performed by Igor Pro software. Concerning XPS, experiments have been performed at normal electron acceptance using acquisition conditions ideal for quantitative and high resolution studies (Passing energy, PE, of 20eV and 10eV). The photon source was a Mg Kα with an energy of 1253.6eV, achieved from a magnesium anode. Total maximum energy resolution is 0.86 eV. All the core level binding energies (BE) were normalized to the Au 4f7/2 core level signal (at 84.0 eV), obtained from a sputtered gold surface. The core level analysis has been performed by Voigt line-shape deconvolution after the background subtraction of a Shirley function. The typical precision for each component's energy position is ±0.05 eV. The uncertainty for the full width at half-maximum (FWHM) is less than ± 2.5%, while for the area evaluation it is about ± 2%.

3.7 Thrombin Detection

In order to evaluate the sensing performance of the OECT-based aptasensor against thrombin (Thr) protein, a calibration curve has been made by using different concentrations of Thr. The purified human α-thrombin (purchased from Sigma-Aldrich, USA) from its lyophilized form was dissolved in its buffer to reach a final concentration of 1 μM. The thrombin buffer (Alfa Aesar, USA) presents the following composition: 200 mM Tris-HCl pH 8.4, 1.5 mM NaCl and 25 mM $CaCl_2$.

From this stock solution, samples of Thr were prepared with different concentrations operating the appropriate dilutions, in order to obtain the following concentrations: 1, 5, 10, 20, 40, 60, 80 and 100 pM.

The last step of the analytical procedure for the aptasensor consists in the recognition of thrombin by the immobilized aptamers on the AuNPs-PMLG gate electrode. To do this, 10 μl of each Thr solution, with the desired concentration, was drop casted on the gate electrode surface for an overnight incubation at 4°C. After that, the electrode was washed twice with sterilized water to remove nonspecific protein adsorption.

3.7.1 OECT driven by a Thr-incubated TBA-15 modified AuNPs-PMLG Gate Electrode.

The OECT response after the thrombin incubation on the TBA_{15}-AuNPs-PMLG gate electrode was studied by direct comparison between transfer curves before and after the thrombin incubation process while the data acquisition was made by using the same set up and working parameters (already mentioned in sections 3.5.1)

3.7.2 Evaluation of the Aptasensor Selectivity/sensitivity

The evaluation of the OECT-based aptasensor against thrombin has been tested by drop casting 10 µl of a solution of bovine serum albumin (BSA) (purchased by Biowest, USA) with a concentration of 1 mM in PBS 10 mM solution, on the surface of a TBA_{15} modified AuNPs-PMLG gate electrode. The protein has been incubated overnight at 4 °C following the same procedure employed for thrombin and finally the electrode was washed twice with sterilized water to remove excesses of protein.

Also in this case, OECT response after the BSA incubation was evaluated by the comparison between acquired transfer curves before and after the incubation and performed with the same set of parameters, conditions and methodology already reported in this chapter.

The formation of unspecific bonds between thrombin and the gate electrode surface was investigated performing the so call “blank measure”. To do this, 10 µl of a 100 pM thrombin solution have been drop casted on the surface of a AuNPs-PMLG gate electrode without aptamers functionalization and the thrombin was incubated overnight at 4 °C. The electrode was washed twice with sterilized water to remove excesses of protein and the OECT response has been studied performing a transfer characterization using the same parameters employed for the construction of the calibration curve.

Chapter 4

RESULTS AND DISCUSSION

4.1 PMLG GATE ELECTRODE MORPHOLOGY

The gate electrode is composed of multi-layers graphene (MLG) deposited on a substrate of low-density polyethylene (LDPE) and it comes as a flexible and grayish film.

A morphological characterization of the graphene gate electrode (PMLG) surface was performed by scanning electron microscopy (SEM) and a typical micrograph is reported in Fig. 4.1.

Fig. 4.1 shows that the MLG covers the whole surface of LDPE substrate and displays an uncontrolled and not ordered over-layer of graphene sheets with different dimensions. This is probably due to the deposition procedure of the MLG on the LDPE substrate that was carried out through a drop casting method.[248] In some areas, the MLG electrode shows an intermediate structure between graphene and graphite due to the presence of stacking of variable number of polygonal platelets and a certain content of defects, which lead to a non-planar structure.

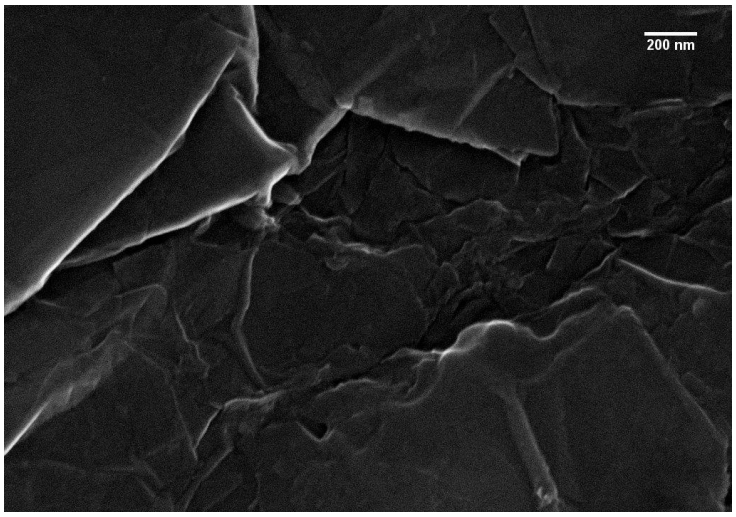

Figure 4.1: *SEM image of the graphene surface of the MLG-LDPE gate electrode with a 100.00 K X magnification.*

This morphological observation has been further supported by Raman spectroscopy that was used to study the properties of the graphene surface in terms of defects density and number of layers.

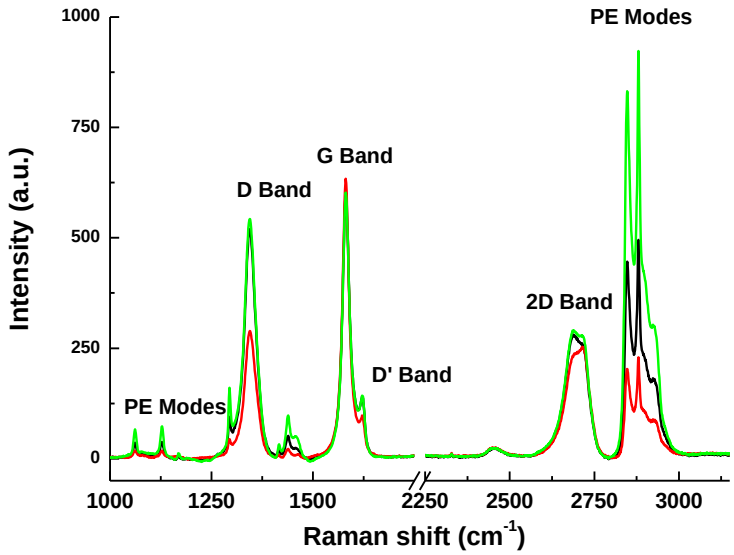

Figure 4.2: *Raman spectrum from different PMLG surface areas. Three typical main spectra were found and they are indicated with three different colors: green, red and black.*

Raman analysis reported in Fig. 4.2 shows the concurrent presence of visible peaks related to both MLG and LDPE. The peaks attributed to the LDPE were identified in the spectrum as PE Modes and they can be found at Raman shift values of: 1064 cm^{-1}, 1140 cm^{-1}, 1293 cm^{-1}, 1412 cm^{-1}, 2847 cm^{-1},

2886 cm^{-1} e 2933 cm^{-1}. The peaks at 1064 cm^{-1} and 1140 cm^{-1} are related to the asymmetric stretching of C-C bonds of the polymer backbone. The peaks at 1293 cm^{-1} and 1412 cm^{-1} are respectively associated to the asymmetric bending out-of-plane (twisting) and to the asymmetric bending in-plane (wagging) of the $–CH_2$ group. Usually, Raman peaks in the region of the spectrum between 2700 cm^{-1} and 3100 cm^{-1} are identified as due to the C-H bond stretching, thus peaks at 2833 cm^{-1} and 2933 cm^{-1} have been attributed to the bond asymmetric stretching, while peak to 2847 cm^{-1} is connected to the asymmetric stretching of the C-H bond.

Graphene Raman peaks are located in the typical Raman shift values: 1347 cm^{-1}, 1582 cm^{-1}, 1610 cm^{-1} and 2700 cm^{-1} for a laser excitation at 532 nm. The peak at 1347 cm^{-1} is the so called D-band which can be found only in disordered graphene with an high density of defects. The D peak is a defects induced mode and comes from the *breathing mode* A_{1g} of the carbons in the benzene rings.[252] The peak at 1582 cm^{-1} is the G-band, which is the only due to a normal first order Raman scattering process in graphene and that is related to a primary *in-plane* vibrational mode (E_{2g}) at the Brillouin zone center.[253] D-band at 1610 cm^{-1} is another disorder-induced peak and it is caused by double resonance intra-valley scattering of a photo-excited electron by a phonon along with elastic scattering by a defect. The peak at 2700 cm^{-1} is related to a second-order overtone of the D-band, but does not need defects to be activated.[254]

The Raman analysis allows to distinguish graphene from graphite, in fact, in the case of monolayer graphene the G-band is located at Raman shift values higher than 3-5 cm^{-1} with respect to graphite. Another parameter that can be used to discriminate graphene from graphite is the 2D band: in graphite two peaks, named 2D1 and 2D2, compose the band, respectively at ¼ and ½ height of the G-peak while in graphene the 2D is a single symmetric peak at lower wavenumbers. From the evaluation of the 2D band intensity, it is also possible to determine the numbers of graphene layers: from a monolayer to a bilayer graphene the intensity of the peak decreases and becomes 2/3 of the G-peak intensity. As the number of layers increases, the 2D band changes its shape and position and becomes very similar to the graphite band with two components. In this case, as shown in Fig. 4.2, the 2D band is not a single peak but shows the presence of two different peaks, furthermore, it is less intense than the G-peak that indicates the presence of several graphene layers. The ratio between the intensity of the 2D and G peaks, I_{2D}/I_G, is about 0.55, which corresponds to a number of layers between 5 and 10.

From Raman analysis of different PMLG surface areas, we identified zones in which the ratio between the MLG G peak (1580 cm^{-1}) and the LDPE C-H stretching mode intensities (2800 cm^{-1}-

2900 cm^{-1}) differs significantly. The spectra obtained in these different areas are reported in Fig. 4.2 with different colors. According to the ratio values, it is possible to define three main different areas:

1- G Band >> LDPE modes (red line)

2- G-Band ≈ LDPE modes (black line)

3- G Band << LDPE modes (green line)

These results indicate a different thickness of the MLG in the LDPE matrix, in total agreement with the non-planar structure highlighted in the SEM analysis.

4.2 PMLG - OECTs ELECTRICAL RESPONSE

PMLG OECT's performance is investigated by different electrical characterizations from which some key parameters including the device's amplification power (transconductance) and its time response are extracted.

One of the first characterizations that can be carried out is the so-called "output characteristic" that measures the I_{ds} variation as a function of V_{ds} at a fixed V_{gs}. To get a complete picture of the OECT operation, it is necessary to study the effects of both V_{ds} and V_{gs} on the I_{ds} modulation, and thus for this purpose, output characteristics are performed measuring the effect of different values of $V_{gs.}$ The "output characteristics" are usually measured in the third quadrant of the I_{ds} vs V_{ds} plot, in which V_{ds} assumes negative values while V_{gs} is positive.

Fig.4.3 reports the typical output characteristics of an OECT system integrating a PMLG gate electrode, performed by varying V_{ds} in the range from 0 V to -0.6 V with steps of 0.05 V and a holding time of 5 s. The values of V_{gs} investigated were in the range -0.2 to 0.8 V and the electrolyte of choice has been PBS (pH 7.4) 10 mM.

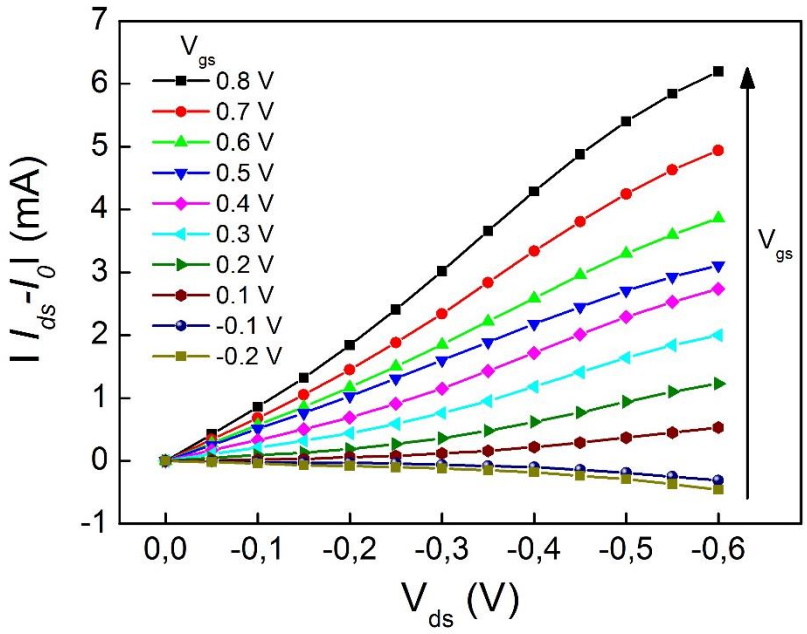

Figure 4.3: *PMLG gated OECT's output characteristics in PBS 10 mM. The* $|I_{ds} - I_0|$ *modulation is plotted against* V_{ds} *from 0 to -0.6 V. Each curve refers to a constant value of* V_{gs} *as reported in the label, ranging from -0.2 to 0.8 V.*

The modulation of the channel current is expressed as $|I_{ds} - I_0|$ where I_{ds} is the current measured for the corresponding value of V_{ds} while I_0 is the current measured at $V_{ds} = 0$ V.

The output characteristic displays the typical low voltage operation regime, which is one of the most important features for the applications of OECTs in the biological field. In fact, excluding the very low values of V_{ds} (< 0.1 V), there is a clear discrimination between the curves corresponding to different V_{gs}. This means that even low V_{gs} changes affect the intensity of the device output current, modulating efficiently transistor's properties.

In order to obtain a highly stable and fast responding OECT, it is necessary to characterize the temporal response of the drain current to any chemical or physical change into the device. The temporal response of an OECT depends on both the ions transport from the electrolyte to the channel and the transit time of holes in the PEDOT:PSS channel. The latter can be estimated by calculating the time response of the OECT when driven by a constant gate current, I_{gs}, according to the definition proposed by Khodagholy[105]:

$$dI_{ds}/_{dt} = {}^{-I_{gs}}/_{\tau_e} \tag{4.1}$$

where τ_e is the holes transit time, which in the OECT engineered for this work has been found equal to 52.20 µs. Fig. 4.4a shows dI_{ds}/d_t calculated for different I_{gs} values (black circles) and the corresponding linear fit (red dashed line) the slope of which corresponds to τ_e. The value obtained is low enough to indicate that the holes transport in the channel is not the limiting factor in the OECT temporal response.

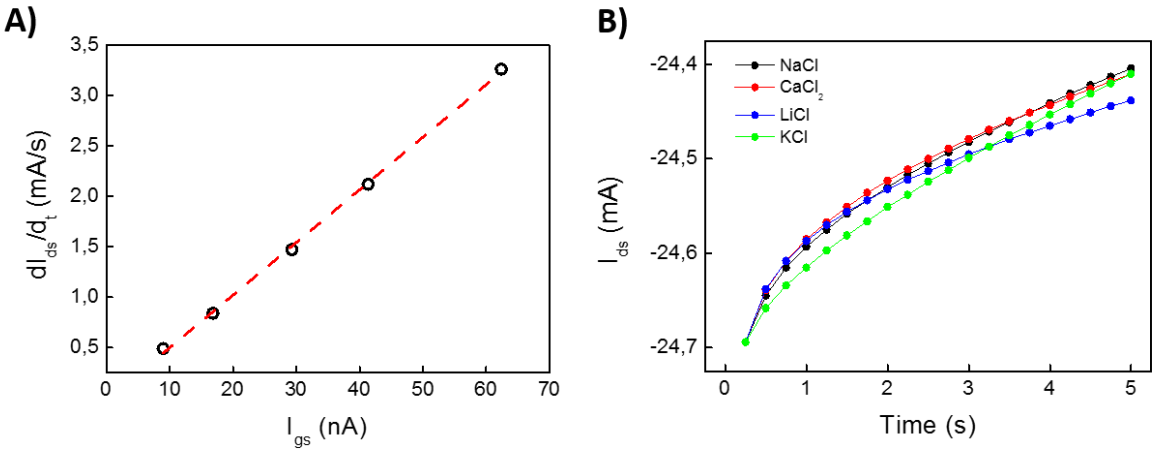

Figure 4.4: *a) Evaluation of the holes transit time τ_e which corresponds to the slope of the linear fit (red dashed line) calculated for different I_{gs} values (black circles). b) Evaluation of the effect of different salts on the OECT time response in terms of I_{ds} modulation.*

This means that the OECT temporal response is dominated by the ions transport from the electrolyte into the organic channel, according to the dependence of the drain current by the type of ion in the electrolyte solution, as shown in Fig. 4.4b. Four different solutions of LiCl, NaCl, KCl and $CaCl_2$, at a concentration of 10 mM, were used as electrolyte in the PMLG OECT and 1 V pulse was applied at the gate electrode for 5 seconds, while the I_{ds} was measured as a function of time. When NaCl and $CaCl_2$ solutions are used as electrolytes, OECT temporal responses (I_{ds} modulation against time) exhibit the same trend because the two cations (Na^+ and Ca^{2+}) have very similar values of hydrated ionic radius: respectively 154 pm and 174 pm. In contrast, when the electrolyte is KCl, the device response shows an initial I_{ds} modulation lower than in the case of NaCl and $CaCl_2$ that then reaches the same values of the other two solutions. This slower I_{ds} modulation can be justified once again by the hydrated ionic radius of K^+ that is bigger (196 pm) compared to the other two salts, leading to a slower ions permeation into the channel. Despite LiCl is the electrolyte where cations (Li^+) have the smallest hydrated ionic radius (134 pm), it leads to the lowest I_{ds} modulation. In this case the very small size of the Li^+ ions could give rise to absorption and intercalation into the gate made of

multilayers of graphene. In fact, this is one of the reasons why, together with graphite and several graphene nanostructures, MLG has been widely used as anode material in lithium ion batteries (LIB).[255–258] The relatively strong interaction between Li^+ and the PMLG inhibits their rapid diffusion in the electrolyte solution, leading to a lower amount of cations in the electrolyte bulk available for the channel de-doping.

The ions trapping into a PMLG gate electrode has been combined with the amplification typically provided by OECTs, for the development of a highly sensitive ions-sensor endowed with unique non-volatile characteristics allowing tracking continuously the presence of a specific compound, keeping memory of previous sensing results and accumulating sequential measurements.[250]

Graphene is also well known for its capacitive behavior, and recently, it has been proposed, together with some of its derivatives, as a very good candidate for developing highly effective supercapacitors.[259] The capacitance in the PMLG OECT has been studied by the **sensing characterization** in which the I_{ds} modulation is measured as a function of time, while at the gate electrode a series of potential pulses with growing amplitude were applied. Fig. 4.5a reports the result of a typical sensing experiment, in which the V_{gs} is varied between -0.2 V and 1 V with voltage pulses starting from 0 V and reaching increasing voltage amplitude of steps of 0.1 V and of 1 second.

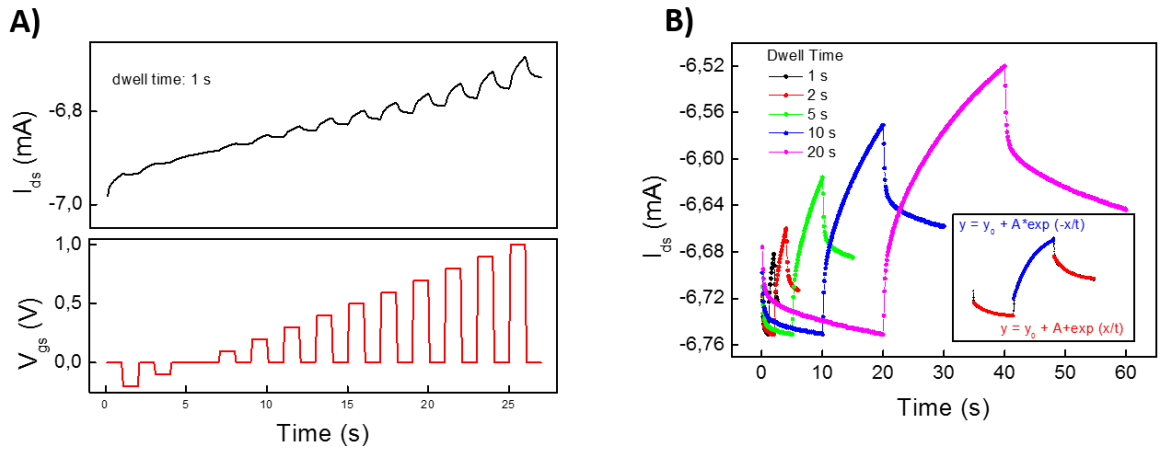

Figure 4.5: *a) typical sensing experiment: V_{gs} is applied as pulses with growing amplitude as shown in the graph at the bottom and an example of the I_{ds} as a function of time is shown in the graph at the top. b) V_{gs} pulses of 1 V with different duration times, in the inset is shown the OECT time response, which can be fitted with the typical equation ruling the charge-discharge of a capacitor.*

Different voltage application times were investigated, as shown in Fig 4.5b, but also for long dwell time (10 and 20 s) the I_{ds} modulation keep decreasing without reaching the saturation, steady state

value. As already pointed out, this effect could be associated with the ability of the graphene gate electrode to act as a capacitor. In fact, it is well known that the charge accumulated on a capacitor surface is directly proportional to the voltage applied and the constant of proportionality is known as capacitance C, as represented in the following equation:

$$Q = C\Delta V \tag{4.2}$$

The charge accumulated on the capacitor is also time-dependent, according to the following equation:

$$Q = Q_f \left[1 - e^{-(t/RC)}\right] \tag{4.3}$$

where Q_f is the final charge that accumulates on the capacitor and R is the circuit resistance. From equation 4.3, it can be seen that charge builds up exponentially during the charging process and theoretically, the capacitor takes an infinite amount of time to fully charge, where the typical time constant RC.

What appear clear at this point is that greater is the application time of a defined V_{gs}, greater is the charge accumulated on the PMLG gate electrode, which leads to the formation of an electrical double layer (EDL) at the electrolyte interface. The produced EDL induces an injection of cations into the PEDOT:PSS, dedoping it and hence reducing its conductivity with the consequent I_{ds} modulation. Furthermore, for every dwell time explored, the current modulation does not reach the saturation, meaning that the continuous channel dedoping is supported by the continuous charge accumulation at the surface of the PMLG gate electrode. The already discussed complicated morphology of our graphene electrode also comes in this picture coherently. When V_{gs} is brought back to 0 V, the PMLG surface starts discharging following an exponential decay, as shown by the subsequent equation:

$$Q = Q_0 e^{-(t/RC)} \tag{4.4}$$

where Q_0 is the initial charge of the capacitor at the beginning of the discharge.

As highlighted in the inset of Fig. 4.5b, I_{ds} follows an exponential growth during the application of 0 V at the gate electrode (red lines) and an exponential decay when V_{gs} is equal to 1 V (blue line), well reproducing the typical charge/discharge trend of a capacitor.

For implementing the PMLG OECTs as a biosensor, a combination of parameters extracted from the output and the sensing characteristics were selected. From the output characteristics is possible to extract the values of V_{ds}, hence V_{ds} was set at -0.25 V for all the following measurements in order to ensure a good discrimination and to limit the current flowing in the system, otherwise cations in the

electrolyte would not be affected only by the gate electrode but also by the channel. From the sensing experiments has been determined the application time of V_{gs} steps to influence the OECT response. The holding time was set to 5 s so that V_{gs} would stay constant for a time long enough to trigger a stable I_{ds} variation.

The final characterization has dealt with the "transfer curves" where the I_{ds} modulation is measured as a function of V_{gs}. Since V_{ds} was set to -0.25 V, V_{gs} was switched between -0.2 and 0.8 V with steps of 0.01 V to avoid the onset of a voltage difference greater than 1.25 V through the electrolyte which could generate electrolysis that should be carefully avoided in biological applications.

The results are reported in Fig 4.6a, in which the modulation of the I_{ds} is compared with the trend of the current through the gate electrode I_{gs}.

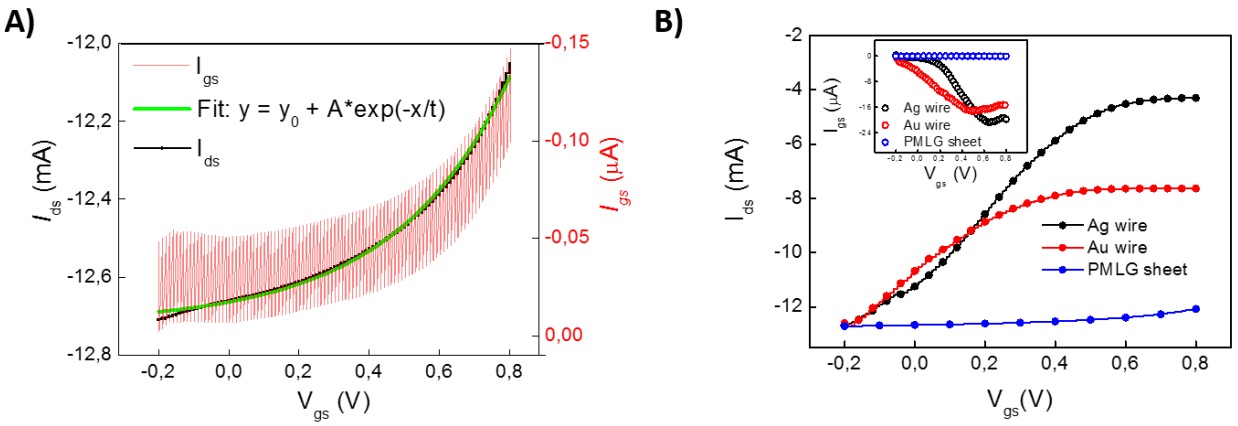

Figure 4.6: *a) PMLG OECT's transfer characteristics: comparison between I_{ds} (black line) and I_{gs} (red line) modulation in the same V_{gs} range. The same exponential trend is observed for both currents modulation. b) Comparison of I_{ds} modulation in presence of different types of gate electrodes. The shows I_{gs} related to the three different gate electrodes: Ag wire (black line), Au wire (red line) and PMLG sheet (blue line).*

I_{ds} and I_{gs} as a function of V_{gs} have the same trends, what changes are the current absolute values that in the case of the channel current are three orders of magnitude larger than the gate current. This result demonstrates that since OECTs are highly effective amplifier transducers, what occurs at the gate electrode is amplified through the channel, confirming what has been said so far. As discussed for the sensing characteristic, I_{gs} is originated by the accumulation of charges at the gate electrode, which for a general capacitor exhibits an exponential trend, according to the following equation:

$$i(t) = \frac{Q}{RC}\, e^{-(t/RC)} \tag{4.5}$$

The fitted curve in Fig. 4.5a highlights this exponential decay explaining the resulting negative I_{gs} contribution by the accumulation of negative charges (anions) at the gate electrode surface due to the application of positive voltages V_{gs}.

To confirm the hypothesis that the PMLG-OECT response, in terms of I_{ds} modulation, is due to the combination of the capacitive behavior of graphene and the amplification properties of the transistor, the device response was compared with the one obtained with metallic gate electrodes such as Ag and Au wires. The parameters used for the transfer characterization were the same reported before and the results are shown in Fig. 4.5 b where the three transfer curves are compared.

As could be expected, Ag wire displays the greatest I_{ds} modulation leading to a current saturation at about 0.5 V of V_{gs}. As discussed in the second chapter, this high current modulation is due to Faradaic processes at the gate electrode, because in the PBS buffer solution in addition to phosphate salts, are also present NaCl salts, the halide Cl^- of which interacts with the Ag gate electrode leading to a redox reaction ($Ag + X^- \leftrightarrow AgX + e^-$).

As discussed in the second chapter, the Au wire electrode induces a lower I_{ds} modulation with respect to the Ag wire since, because of its polarizable nature, it allows the formation of an EDL inducing a potential drop through the electrolyte in turn leading to a less effective current modulation,

In both the metallic cases, current modulation could be explained with two distinct and well documented mechanisms,[131] neither of which can be used to explain the PMLG gate electrode behavior. Our findings suggest instead that Graphene is acting as a capacitor, and that the very low I_{ds} modulation produced by PMLG is caused by the instauration of intercalation processes in the gate electrode that affect the channel current by a potential drops through the electrolyte. In this case, the establishment of a capacitive regime leads to a very low I_{gs}.

From the trends observed in the gate currents, metal electrodes could be disadvantageous in implementing OECT as a biosensor where saline buffers like PBS are widely used. In these cases, in fact, the greatest contribution to the I_{gs} variation and consequently to the I_{ds} modulation, comes from the interaction between metal electrodes and salts hiding any other event that could happen in the proximity of the gate electrode including the interaction between a target molecule and the bioreceptor deposited on the gate electrode. This is the principal reason that makes PMLG a good candidate as gate electrode in an OECT for biological applications. In fact, it results mostly inert against saline buffers enhancing the ability to detect any other event at the gate electrode proximity.

4.3 GOLD NANOPARTICLES (AUNPS)

The PMLG gate electrode has been modified through the surface decoration with gold nanoparticles (AuNPs). AuNPs were prepared in solution with a seed-induced growth method by reduction of chloroauric acid ($HAuCl_4$) according to the Frens protocol.[251]

AuNPs, like any nobel metal nanoparticles, show a surface plasmon resonance band (SPR), which is the result of the collective oscillation of the conduction electrons across the particles due to the resonant excitantion by an external electric field (light).[260] The SPR band intensity and wavelenght depend on several factors that affect the electron charge density on the particles surface such as particles size, shape, composition and the dielectric constant of the surroding medium.[261]

The production of AuNPs is confirmed by UV-vis absorbance measurement that shows the characteristic sharp absorbance peak around 520 nm, as reported in Fig. 4.7a. The narrow peak and the absence of other peaks above 550 nm indicates the monodispersivety of the nanoparticles. This result is further confirmed by the TEM analysis, in fact, as can be seen in Fig 4.7b the geometry of the AuNPs is mainly spherical and the size distribution calculated for a batch of 500 AuNPs shows a narrow dispersivity between 10 and 20 nm with a mean diameter of about 13 nm (Fig. 4.7c).

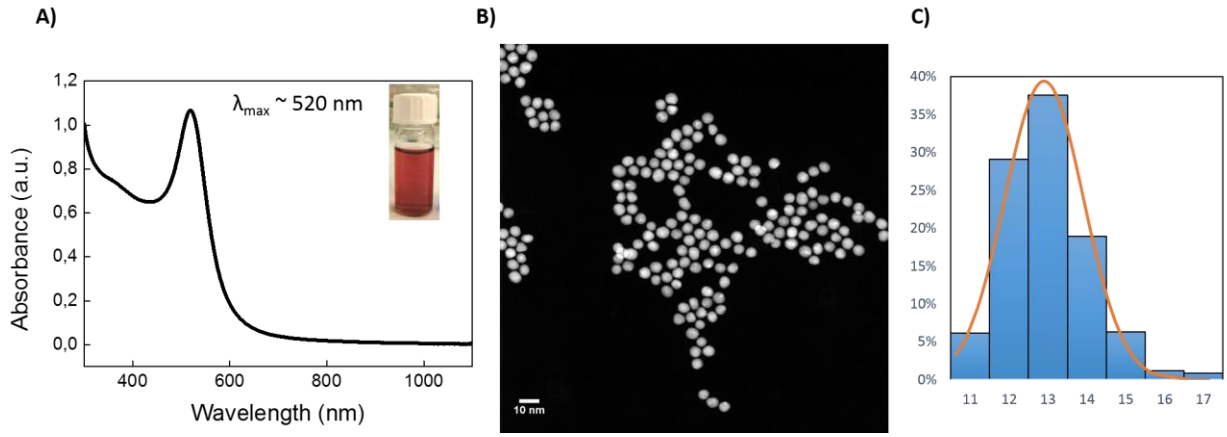

Figure 4.7: *a) Uv-vis spectra of AuNPs dispersion synthesized trough seed-induced growth method; the inset shows the final aspect of the colloidal solution that appears as a clear red solution. b) typical TEM micrograph of a portion of AuNPs where the principal geometry is spherical c) size distribution of AuNPs having a mean diameter of about 13 nm.*

Dynamic light scattering (DLS) has been performed to determinate the size of the AuNPs in solution and the results are reported in Fig. 4.8. The hydrodynamic diameter as obtained by DLS shows a

bimodal particles size distribution, which appears as two distinct peaks: a mode at small sizes (17-20 nm) related to a large number of particles and a second, less populated mode, at larger sizes (100-130 nm). The first mode with smaller size present a DLS diameter higher than the size measured with TEM because the DLS method is based on the measure of the diffusion rate that depends not only on the core size of the nanoparticles but also on any surface structures including the capping agent. The second mode with higher hydrodynamic diameter is due to the presence of AuNPs aggregates.

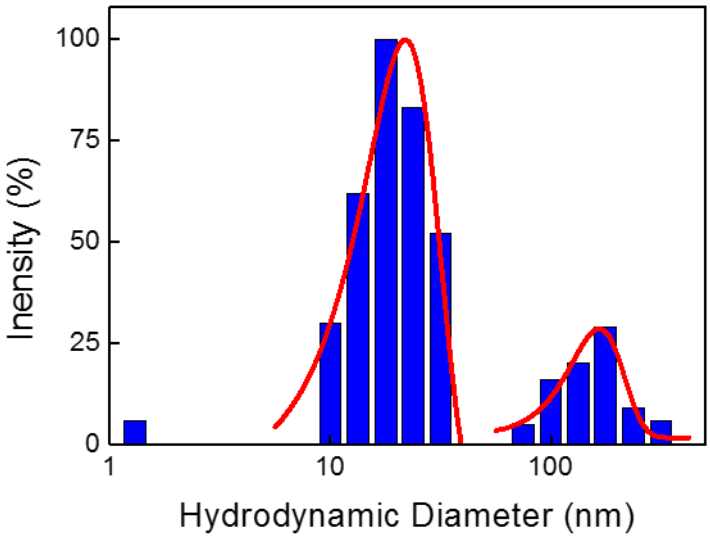

Figure 4.8: *Bimodal particles size distribution obtained for the analysis of the dynamic light scattering of the synthesized AuNPs in solution*

A Zeta-potential analysis has been performed in order to evaluate the nanoparticles charge and stability. The zeta potential cannot be measured directly, but is estimated from the electrophoretic mobility μ, which corresponds to the rate of migration of charged particles in a liquid medium with the application of an external electric field. The environment of the nanoparticles affects the electrophoretic mobility, which in turn influences the zeta potential ζ. The main factors in this context are the ionic strength and the NPs radius. Based on these parameters, the best representation of the correlation between μ and ζ can be given by the Smoluchowski[262] or by the Huckel[263] equations. The former must be used for the environment of large NPs and high ionic strength, while the latter is related to small NPs and low ionic strength.[264] The zeta potential for the citrate-capped AuNPs with a mean core diameter of 13 nm was calculate employing the Huckel equation:

$$\mu = \frac{2\zeta\varepsilon f(\kappa a)}{3\eta} \tag{4.6}$$

where ε is the dielectric constant, η the viscosity of the surrounding liquid and f(κa) is the Henry's function in which κ is the Debye length and the particle radius. The resulting effective surface charge of the citrate-capped AuNPs is -13.44 mV.

4.4 DECORATION OF A PMLG ELECTRODE WITH AUNPS

Since the citrate-capped AuNPs in solution possess a net negative charge, the electrophoretic deposition method (EPD) was exploited to deposit AuNPs on the surface of the PMLG electrode. In the EPD technique, charged nanoparticles are driven towards and deposited onto the surface of an electrode, dip-coated in a solution, with the application of an external electric field perpendicular to the substrate. To deposit the AuNPs, a positive potential of 40 V was applied constantly at the PMLG acting as anode electrode while a chrome electrode was used as cathode and grounded.

The AuNPs deposition on PLMG electrode was monitored recording the current flowing in the solution versus the time (see Fig. 4.9a).

The current measured in an EPD experiment is indicative of the motion and deposition of the charge-carrying nanoparticles. In fact when the positive potential is switched on an intense current is recorded the value of which depends on the AuNPs initial concentration. Subsequently, the current gradually drops down with the decreasing of the density of AuNPs in solution due to their deposition on the PMLG electrode until it reaches zero indicating the end of the reaction.

To investigate the morphology of the PMLG electrode surface after the AuNPs deposition, a scanning electron microscopy (SEM) was performed and it is shown in Fig. 4.9b. A well dispersed and homogenous distribution of AuNPs on the PMLG surface is observed, where the nanoparticles retain the shape and the size of the solution, proving that the EPD method does not affect the physical properties of the nanoparticles. The estimated coverage percentage of the PMLG surface is 42%.

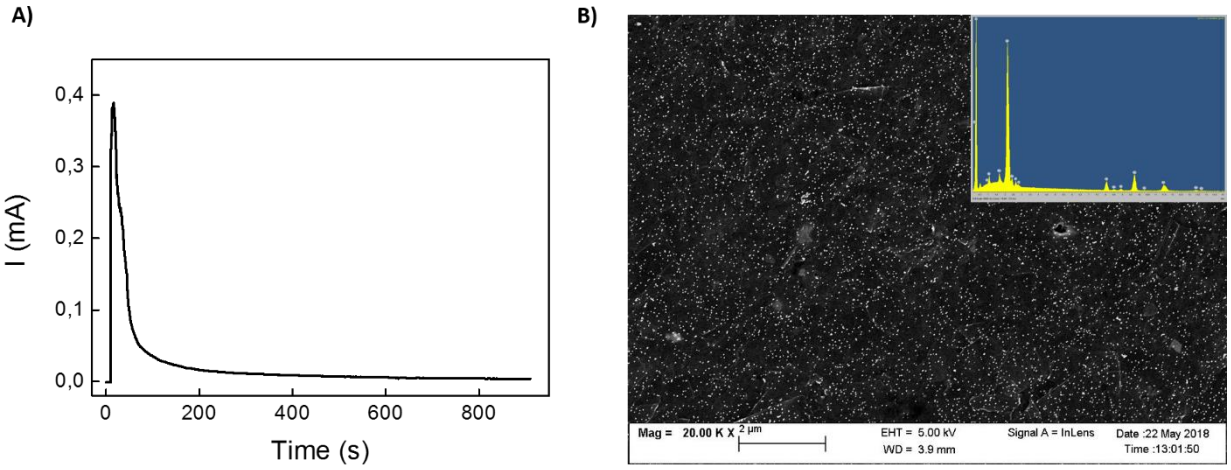

Figure 4.9: *a) The electric field between the anode and the cathode, drives AuNPs towards the PMLG surface where they are deposited producing a specific I vs time profile. b) SEM image of the PMLG gate electrode surface after an homogenous deposition of AuNPs; in the inset the EDX analysis of the as decorated gate electrode surface.*

A study of the elemental composition of the AuNPs-decorated PMLG electrode surface was carried out with the Energy Dispersive X-ray analysis (EDX) to further confirm the presence AuNPs. In the inset of Fig. 4.9b the spectrum is shown which clearly presents, in addition to the carbon signal 0.28 KeV (K line) related to the graphene substrate, the main gold signals at 1.87 KeV, 2.12 KeV (M Line) and 9.89 KeV (L Line) confirming the presence of AuNPs on the gate electrode surface. The peaks at 0.930 and 8.040 KeV are due to the copper emission, which is the constituent material of the sample holder.

4.5 RESPONSE OF AN OECT WITH AUNPS-PMLG AS GATE ELECTRODE

Transfer characteristics studies were performed to study how the presence of AuNPs on the PMLG gate electrode could change the OECT response,. To compare the OECT behavior with the one obtained in the case of the bare PMLG gate electrode, the transfer curve of the AuNPs-PMLG OECT has been carry out using the same parameters employed during the PMLG-OECT characterization. Therefore V_{ds} was set at -0.25 V, the holding time at 5 s while V_{gs} was switched between -0.2 to 0.8 V with steps of 0.01 V. The electrolyte, also in this case, was the PBS buffer solution with a concentration of 10 mM.

The comparison between the two OECT responses is reported in Fig. 4.10a where the both I_{ds} and I_{gs} are plotted in the analyzed V_{gs} range. As expected, the the different gate electrode nature leads to a

change of the gate current behavior that in turn affects the OECT response in terms of the channel current trend.

In addition to a slightly higher currents modulation, the AuNPs decorated PMLG gate electrode (AuNPs-PMLG) shows a profile completely different from the quasi-linear trend of the bare PMLG gate electrode (red line). The current associated to AuNPs-PMLG gate electrode (black line) shows a well-defined peak at 0.1 V proving the presence of an electron transfer between AuNPs and the graphene electrode. It has been demonstrated that AuNPs can lead to a p-dope of the graphene through electron transfer due to the difference in the work function of Au (5.1 eV) and graphene (4.5 eV). The p-dope of the graphene results in a reduction of its sheet resistance increasing the conductivity and the electron mobility of the graphene.[265,266] All this is reflected in the OECT response, in fact, the potential drop that is typical for the bare PMLG gate electrode, in this case is decreased because of the enhanced conductivity of the AuNPs-PMLG leading to a larger I_{ds} current modulation. The total current modulation, which is of about 600 µA in the case of the bare PMLG gate electrode, is enhanced to 2 mA when the PMLG gate electrode is decorated with AuNPs. The electron transfer between AuNPs and the PMLG electrode is not only reflected in the I_{ds} modulation but also on the shape of the transfer curves. The presence of a peak, related to the electron transfer, in the I_{gs} results with in the formation of a step in the transfer curve in the V_{gs} range between 0.2 and 0.6 V.

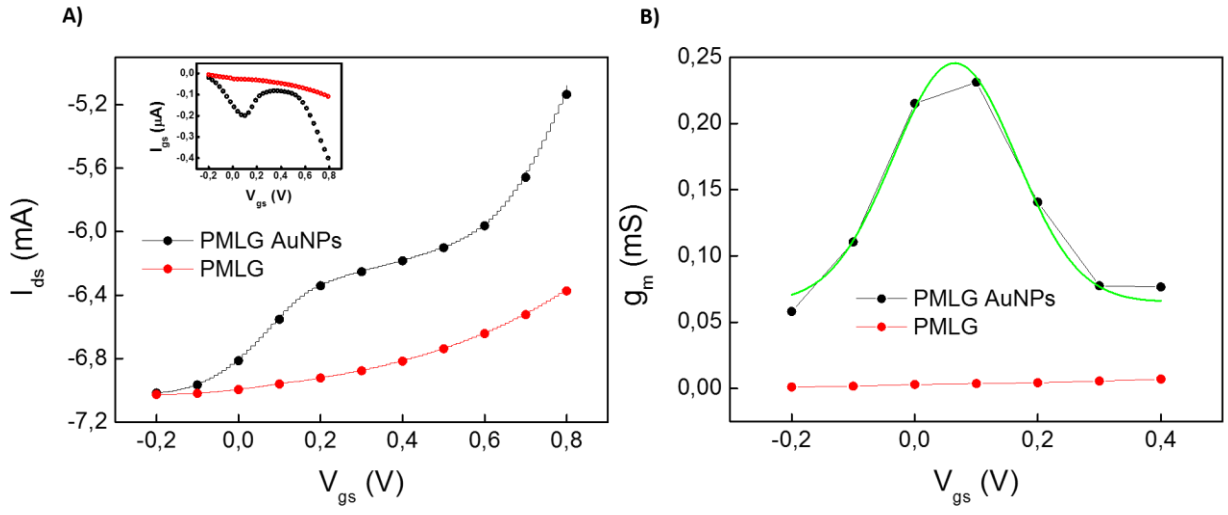

Figure 4.10: *a) Comparison between the transfer curves obtained in absence (red line) and in presence (black line) of gold nanoparticles on the PMLG gate electrode; in the inset is reported the comparison of I_{gs} between the same two gate electrodes. b) The transconductance obtained with the bare PMLG gate electrode (red line) is compared with the one obtained with AuNPs-PMLG gate electrode (black line)*

The larger I_{ds} modulation due to the enhanced conductivity and higher electron mobility of the AuNPs-PMLG gate electrode results also in a higher OECT amplification. The capability of OECTs to amplify the signal at the gate electrode through the polymeric channel is described with the transconductance, which has been defined as the ratio between the output current and the input voltage:

$$g_m = \frac{\Delta I_{ds}}{\Delta V_{gs}} \tag{4.7}$$

The transconductance of the bare PMLG gate electrode is compared with the corresponding one for the AuNPs-PMLG gate electrode in Fig. 4.10b. The transconductance for the bare PMLG gate electrode is a straight line (red line) close to 0 mS in the whole range of the explored gate voltage, indicating that in this case, as expected from the low I_{gs} (Fig. 4.10a), the PMLG OECT shows a quite moderate amplification. For the AuNPs-PMLG gate electrode, instead, the transconductance curve shows a well pronounced peak (black line) stably above 0.05 mS, in the whole range of the applied gate voltage, reaching the maximum value of about 0.25 mS at 0.1 V. Summarizing AuNPs provide the advantage of enhancing the transistor amplification without inducing a saturation of I_{ds} modulation as it occurs for metallic gate electrodes (Ag or Au wires). In this way, the channel current of the AuNPs-PMLG OECT can still be affected by any event that can change the impedance of the gate electrode.

4.6 Functionalization of AuNPs-PMLG Gate Electrode by Immobilization of Thrombin Binding Aptamer-15 (TBA-15)

After having demonstrated that AuNPs improve the conductivity and the sensing performance of the PMLG electrode, a sensitive and amplifying electrochemical biosensor has been developed using OECTs as the transducer platform.

In this PhD project, an anti-thrombin aptamer was employed as bioreceptor and it was combined with the AuNPs-PMLG OECT to engineer a biosensor capable of detecting quite low concentrations of thrombin (Thr). Actually, there are two distinct thrombin binding aptamers (TBA) able to selectively bind specific and different epitopes of human α-thrombin: TBA-15 and TBA-29. The aptamer of choice in this project was the TBA-15, which is a 15-mer oligonucleotide with the following sequence: 5'-G-G-T-T-G-G-T-G-T-G-G-T-T-G-G-3'. This single-stranded DNA interacts with

thrombin selectively binding the protein exosite I and changing its geometrical conformation during the recognition event.[267]

When the TBA-15 forms a complex with thrombin (Thr), its conformation switches from a random flexible structure to a rigid one. The structure of TBA-15/Thr complex, determined by nuclear magnetic resonance (NMR), reveals that it folds in a unimolecular antiparallel quadruplex, with a chair-like conformation.[268] The structure consists of two G-tetrads connected by three edge-wise loops two TT loops at one side and a single TGT loop on the other side and by four guanines in G-quartets stabilized by cyclic hydrogen bonds. Padmanabhan et al,[269] have solved the crystal structure of the TBA-Thr complex with a 2.9 Å but they found that the result was different with respect to the complex structure determined by NMR. In both models, the core formed by two G-quartets is the same, what changes is the way in which the central bases are connected. In particular, there is a difference concerning the position of the loops with respect to the grooves. Anyway, in both models, the TBA is sandwiched between two symmetry-related thrombin molecules and interacts with the fibrinogen-recognition site (exosite I) of a thrombin molecule and the heparin-binding site of a second molecule. In the X-ray model, the TGT loop is connected to exosite I while the TT loops are connected to exosite II.[270] The NMR model shows an inverted pattern of the protein-ligand interaction. The difference between the two models is sketched in Fig. 4.11 a and b, while in Fig. 4.Xc is shown the structure of the complex TBA-15 and thrombin.

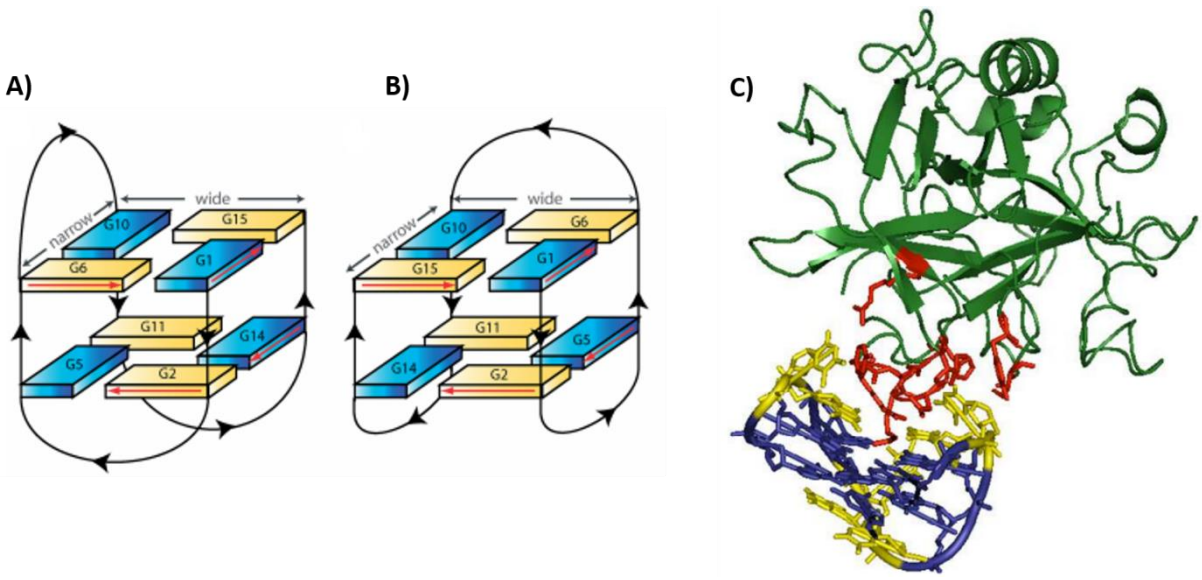

Figure 4.11: *Schematic illustration of a) X-ray model and b) NMR model of the TBA-15 structure. Black arrows indicate 5'→ 3' polarity of the strand. c) Overall structure of the TBA-15/Thr complex: the TBA-15 aptamer is represented as sticks and it is colored in blue except the two TT loops and the TGT loop that are colored in yellow. Thrombin molecule is represented as cartoon and it is colored in green except the red part which represents the amino acid residues that belongs to the exosite I in contact with TBA-15. (Adopted with the permission of [21]).*

This conformational change before and after the formation of the TBA-15/Thr complex can be exploited as the base for the fabrication of an electrochemical aptamer-based biosensor. In fact, when the aptamer is immobilized onto the surface of an electrode through one of its ends, its conformational switch leads to the changes of the position of the second end, which can move away or approach the electrode surface. Therefore, if a signal moiety, such as a redox-probe, is linked to the end of the aptamer, the conformational switch would change the relative position of the signal moiety towards the electrode leading to changes of the electrochemical signals.

This strategy was used for developing a thrombin aptasensors based on OECTs in which TBA-15 aptamers have been immobilized on the surface of the PMLG gate electrode and one of their extremity was modified with ferrocene (Fc) as redox probe. The ferrocene has been covalently linked at the side 3'of the TBA aptamers, while the other 5'side was modified with a thiol group separated from the oligonucleotides sequence by a linear chain of six carbons. The final sequence is: 5' Fc-G-G-T-T-G-G-T-G-T-G-G-T-T-G-G- SH-C_6 3'.

The thiol group was used to link aptamers onto the AuNPs-PMLG gate electrode exploiting the great well known affinity between sulfur and gold in terms of bond strength where the sulfur-gold interaction is considered as a "semi-covalent" bond since its strength is in the order of 45 kcal/mol.[271]

Ferrocene was accidently discovered in 1951 by T.J. Kealy and P.L. Paulson at the Duquesne University in Pittsburgh.[272] An year later G. Wilkinson and R.B. Woodward[273] analyzed its structure with X-ray crystallography proving that ferrocene consists of an iron (II) ion sandwiched between two parallel cyclopentadienyl (Cp) rings each donating 6 π electrons to Fe^{2+} ion. Ferrocene is a redox-active material, which is commonly used as electron transfer mediator and electrochemical tag in several types of biosensors. These type of biosensors are based on the principle that when the Fc is near the electrode surface, before or as a consequence of the binding with the molecule target, an electron transfer between them occurs leading to an electrochemical signal.[274]

For sensing purposes, it is crucial to determine the best concentration of aptamers to be immobilized on the AuNPs-PMLG gate electrode surface, since it may affect the total sensitivity of the system. Thus, solutions of aptamers with different concentrations were prepared in sterilized water and then, after the deposition on different gate electrodes through drop casting, OECT- AuNPs-PMLG devices were characterized by transfer curves. Together with aptamers, a fixed concentration of 6-mercapto-1-hexanol (MCH) has been deposited on the AuNPs-PMLG gate electrode surface as post-blocking agent in order to saturate the unbounded sites preventing non-specific interaction between thrombin

and the gate electrode.[275] This molecule, in fact, is an alkanethiol that contains a sulfur head, which can interact with AuNPs on the gate electrode surface and six carbon atoms in an alkyl chain with a hydroxyl group at the end.

Transfer curves were measured using the same parameters and the same electrolyte (PBS10 mM) employed for the bare PMLG and the AuNPs-PMLG gate electrodes characterizations. The aptamers investigated concentrations were: 0.1, 0.2, 0.4, 1, 5 and 10 µM. For the sake of an easy reading, in Fig. 4.12a has been reported only the transfer curve relative to the 1µM concentration (green line) to be compared with the transfer curves obtained with the bare (red line) and the AuNPs decorated (black line) PMLG gate electrode. In the inset of Fig. 4.12a are also shown the I_{gs} variation related to the three gate electrodes.

As already stated, transfer curves obtained in different cases present different profiles as a function of the chemical-physical modifications of the gate electrode. In this case, where the modifications are related to aptamers concentrations is not an exception. In this context, it is from the direct comparison between modifications that we can get major information.

I_{ds} and I_{gs} curves of the bare and AuNPs PMLG gate electrode show trends well in agreement with what already discussed before. However, the immobilization of aptamers TBA-15 on the gate electrode surface deeply affect I_{gs} profile that must be compared with the decorated electrode (AuNPs PMLG). The intensity of the peak presents in the AuNPs PMLG is decreased and its position is switched from 0.1 V to 0.3 V. This result can be ascribed to the electron transfer between the ferrocene and the graphene mediated by the AuNPs. This result can be ascribed to a combination of effects occurring at the gate electrode and in the conductive channel. The well-known electron transfer property of the Fc in this system is mediated by the AuNPs, but even the gold decorated gate electrode exhibits the same transfer mechanism inducing strong modulation in the device total current. So, the decrease of the peak intensity and the shift of the its position to higher V_{gs} represents the quenching of the transfer mediated by AuNPs on the gate electrode as a consequence of the immobilization of aptamers on it and the promotion of the ferrocene mediated transfer.

This combination of effects is quite likely related to the spatial organization of the aptamers in which the distance between the PMLG electrode and the ferrocene molecule requires more energy to be activated or the result of electrostatic forces interfering with device's EDL, probably caused by the aptamer conformational. This effect, in turns, leads to a lower I_{ds} modulation which becomes comparable with the bare PMLG gate electrode.

It is worth noting that I_{ds} modulation in the case of the aptameric functionalization depends from the concentration of the initial oligonucleotides solution, used in the incubation process. The intensity of the residual peak in the transfer curve due to the gold electron transfer is inversely dependent on the concentration used and, as a consequence, on the aptameric coverage on the gate electrode.

This trend on the one hand confirms the already reported shielding mechanism of the aptamers on the electron transfer induced by AuNPs and on the other hand, leads the opportunity to look for the optimal aptameric concentration/coverage for sensing optimization.

To optimize the gate electrode surface, different aptamers concentrations have been investigated looking for the one for which the I_{ds} modulation overlaps the one recorded with the bare graphene. This, in fact, would indicate that all the AuNPs have been linked by aptamers saturating the entire gate electrode surface and that the only contribution to the OECT response is due to the electron transfer induced by aptamers. In Fig. 4.12b is reported the difference between the I_{ds} current recorded with a defined aptamers concentration (I_{apt}) and the I_{ds} current recorded with the bare PMLG gate electrode (I_{blank}) both at V_{gs} 0.8 V in function of the aptamers concentration.

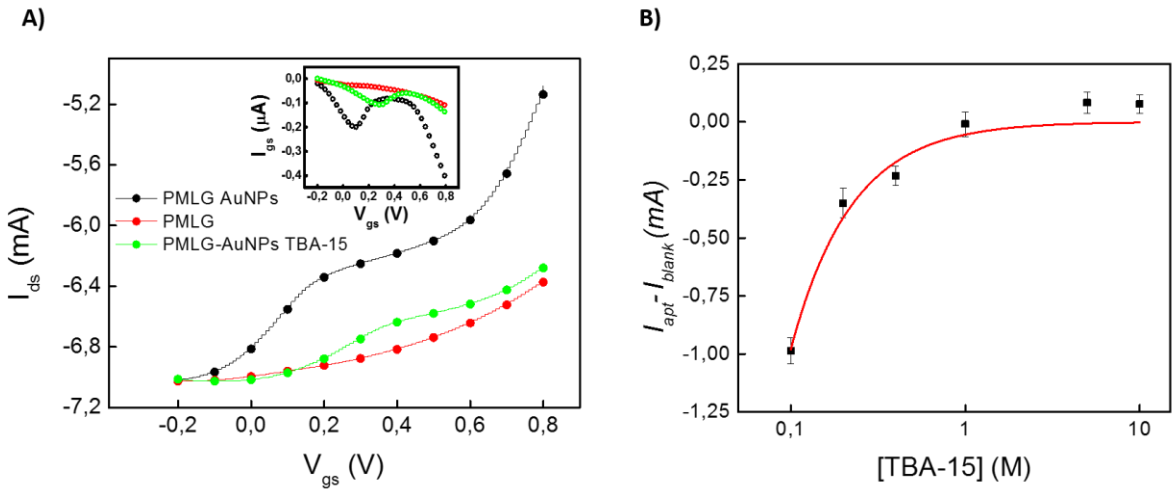

Figure 4.12: *a) I_{gs} (in the inset) and I_{ds} variation performed by the un-folded TBA-15 modified AuNPs-PMLG gate electrode (green lines) compared with the I_{gs} and I_{ds} modulation obtained with the bare PMLG (red lines) and the AuNPs-PMLG (black lines) gate electrodes. b) Optimization of the TBA-15 aptamers concentration reporting the variation of I_{apt}-I_{blank} as a function of the aptamers concentration: the fitting was performed through the Langmuir isotherm (red line).*

The curve resulting by the binding between aptamers and AuNPs can be fitted as a Langmuir isotherm over the concentration range 0.1-10 µM according to the following equation:

$$y = \frac{abx^{1-c}}{1+bx^{1-c}} \quad (4.8)$$

here y corresponds to I_{apt}-I_{blank}, x is the TBA-15 aptamers concentration and a,b and c are coefficient of the equation determinate directly by the fit.

On the basis of the physical meaning of the Langmuir isotherm, this type of fit demonstrates the formation of a mono-layer of non-interacting aptamers on the PMLG gate electrode surface.[276] Moreover, the difference between I_{apt} and I_{blank} decreases with the increase of the concentration of the aptamers solution drop casted on the gate electrode surface, indicating that a greater numbers of AuNPs is bonded with the oligonucleotides shielding the nanoparticles effect on the I_{ds} modulation, as expected. The final curve plateau corresponds to the saturation of the electrode surface indicating that no AuNPs binding sites are available for linking others aptamers. The aptamers optimal concentration has been chosen at the beginning of the saturation and it corresponds to an aptamer's concentration of 1 µM.

An X-ray photoelectron spectroscopy (XPS) analysis has been also performed to study in more details the formation of the gold-thiol binding between aptamers and AuNPs on the PMLG gate electrode surface. This is a powerful technique since allows to get information about the chemical properties and the elemental composition of the studied surfaces and interfaces.

The XPS studies have been performed on three samples: the bare PMLG electrode, the AuNPs-PMLG electrode and the AuNPs-PMLG that has been functionalized with an aptamer solution having the chosen oligonucleotides concentration of 1 µM prepared with the same approach used for the gate electrode preparation.

As can be seen from the wide range spectra for all samples (4.13), graphene has shown presence of only carbon and oxygen species, while for the AuNPs modified gate electrode also gold have been found. Concerning the samples functionalized with aptamers, presence of small amounts of several other elements were detected, such as nitrogen, phosphorous and sulphur. As a first result, the deposition of gold nanoparticles on graphene has been successfully achieved as well as the functionalization of this surface by means of modified aptamers, as evidenced by presence of the typical fingerprints of the organic compounds. It is noteworthy the presence of Silicon (2p and 2s) signals, that are due to the substrate holder, not to the analyzed samples and thus will not be considered in the following.

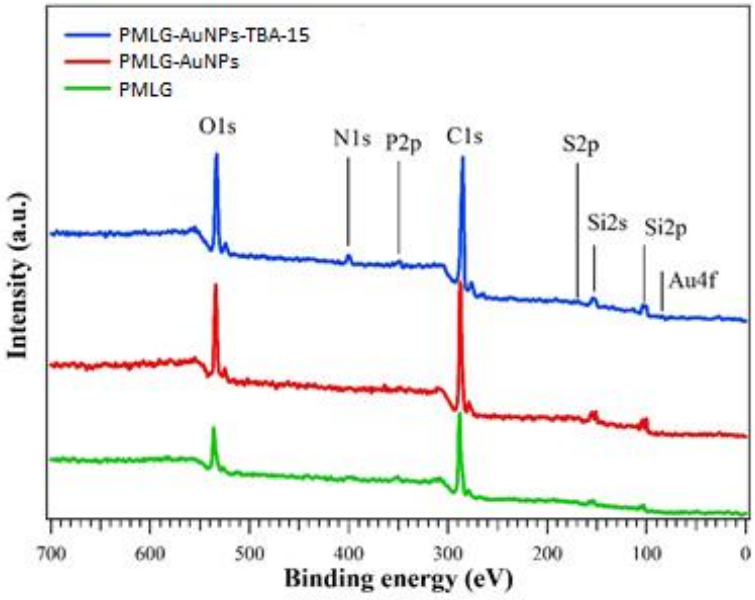

Figure 4.13: *wide range XPS spectra for all samples. Core levels are identified. Silicon (2p and 2s) signals are due to the substrate holder and not to the analyzed samples*

Table 1: *atomic percentages for all elements in the three samples, as evaluated by XPS analysis.*

	C graphene	Au	C Aptamer	O	N	P	S
PMLG	95.5	-	-	4.5	-	-	-
PMLG-AuNPs	95.3	0.04	-	4.4	-	-	-
PMLG-AuNPs-TBA-15	19.8	0.08	64.6	11.4	2.7	1.1	0.4

The atomic percentages of all elements present on the three gate electrodes were evaluated and the relative data are shown in Table 1. In the first two samples, the main element is carbon (C1s core level), as expected due to the presence of graphene as substrate, while, in the aptamers functionalized electrode, it is possible to distinguish carbon core C1s core level signals coming from the graphene and organics compounds. In this case, the attenuation of the graphene signal suggests that the mean thickness of the organic over-layer could be around 6nm in case of a complete and homogeneous coverage of the graphene substrate by the aptamers layer.[277] Presence of aptamers fingerprints confirms the achieved functionalization process, while it is difficult to discuss the absolute C, O, N, P and S atomic percentages due to the low signal to noise ratio of the last three elements. Indeed, this is a common issue as suggested by the large variability reported in literature for aptamers.[278–280]

By studying in details the different core level lineshapes, information regarding the chemical/physical properties of the three surfaces are achieved. Table 2 summarizes the results for all core levels analysis, where single components binding energy and description are shown.

		Peak binding energy, BE (eV)		
Core level	**Chemical species**	**PMLG**	**PMLG-AuNPs**	**PMLG-AuNPS-TBA-15**
C1s				
	Graph. C-C	288.44	287.75	284.62
	Graph. C-O	289.31	288.65	285.52
	Apt. C-C, C-H			285.21
	Apt. C-N, C-O			286.16
	Apt. N-C=O			287.00
	Apt. C-NH2			287.79
	Apt. satellite			288.71
O1s				
	Graph. C-O	534.93	534.51	
	Apt. C=O, N-C=O, P-O, C-O			532.04
	Apt. C-O-C, C-OH			533.54
Au 4f				
	Au 4f 7/2		86.70	84.00
	Au 4f 5/2		90.40	87.66
N1s				
	Apt. N-C			399.6
	Apt. N-H, N-H2			400.82
	Apt. N-$(C)_3$			401.82
P2p 3/2				
	Apt. P-O			134.29
S2p 3/2				
	Apt. S-Au			161.80

Table 2: *Core level components for C1s, O1s, Au4f, N1s, P2p, S2p in all samples. Each component is identified by its chemical origin and binding energy, BE, in eV.*

In the PMLG sample, C1s main peak is broad (1.3eV) and located at 288.44 eV (Fig. 4.14a), about +4 eV from the expected ~284.7eV value for sp^2-hydbridized graphitic carbon. As previously stated, this is due to the insulating character of the LDPE substrate that leads to formation of charging during XPS analysis. A second peak at 289.31eV is also present and it is related to C-O species on graphene.[281,282] The corresponding oxygen species for O1s emission is located at 534.93eV (Fig. 4.14b). The absence of any C1s peak asymmetry, typical of a single or of a few layer graphene,[281,283]

confirms the multilayer nature of the electrode, also taking into account the broadening due to charging.

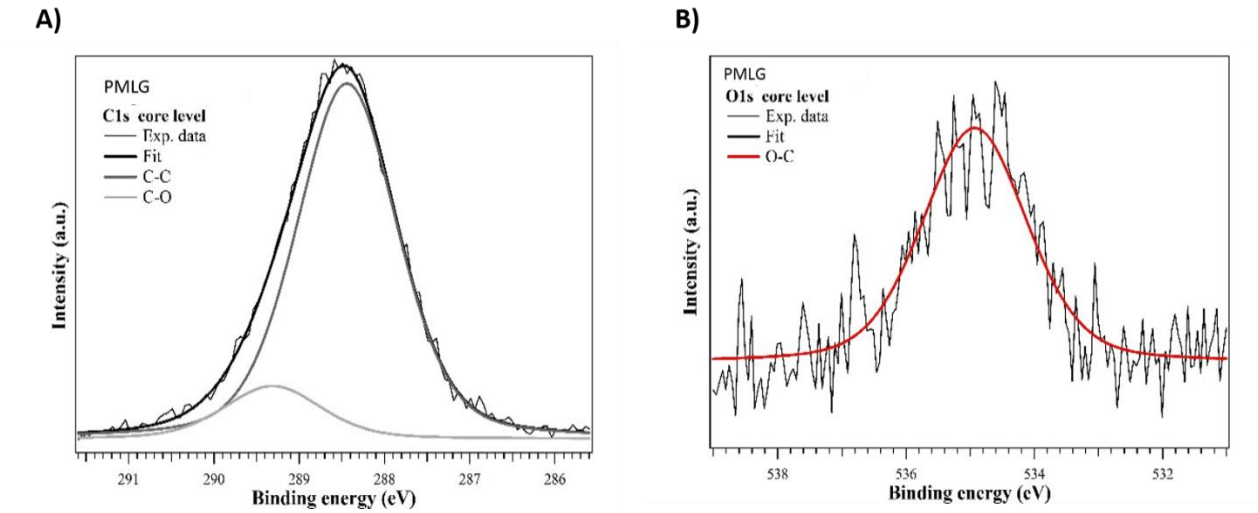

Figure 4.14: *C1s and O1s core levels (left, right) for Graphene on LDPE sample. Single components are described in the legends.*

Similar results have been found for PMLG-AuNPs electrode, with a slightly lower BE shift of about +3.5eV. C1s and O1s show same features of pure graphene (4.15 a and b), while Au4f is characterized by a doublet (Fig. 4.15c), i.e. two peaks separated by 3.6eV as expected for gold. The very low signal to noise ratio is related to the low atomic percentage for gold, about 0.04% close to the XPS detection limit.

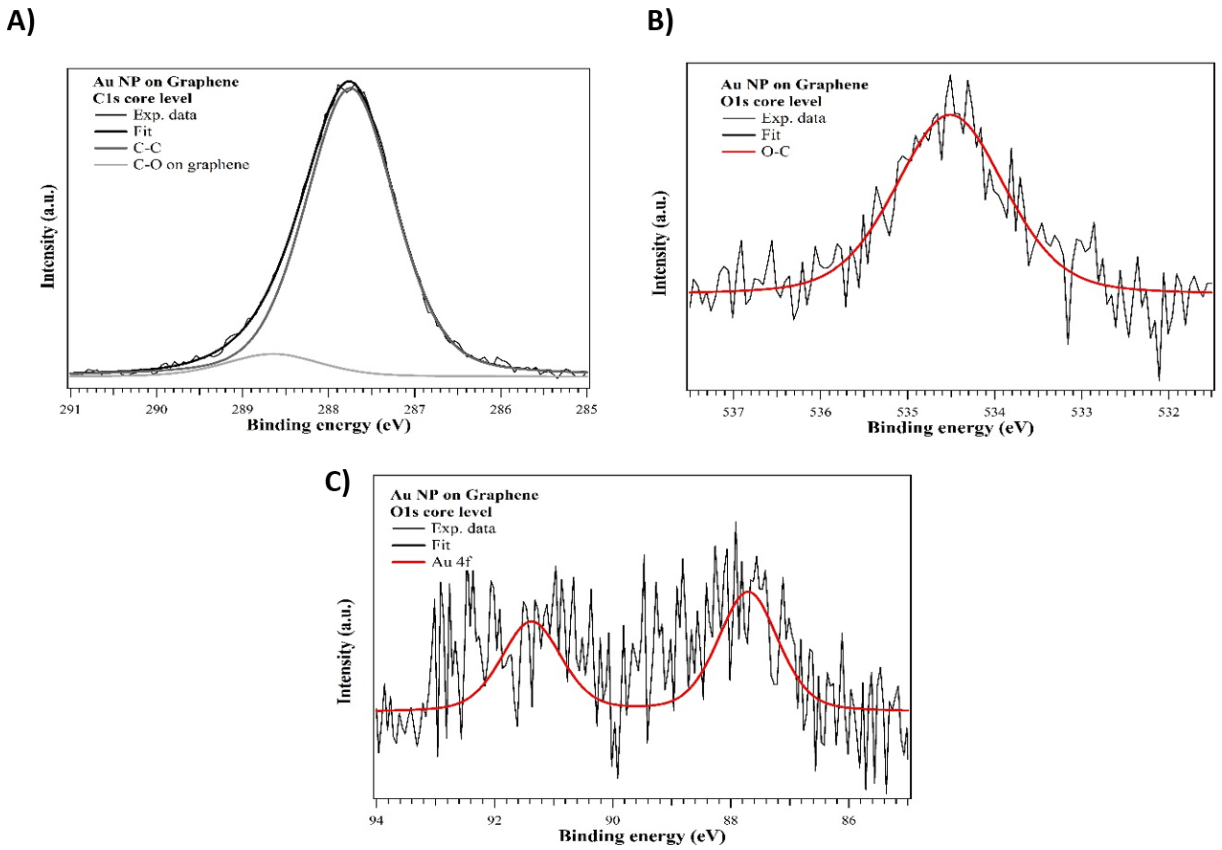

Figure 4.15: *a) C1s, b) O1s and c) Au4f core levels for PMLG-AuNPs electrode. Single components are described in the legends.*

Results for PMLG-AuNPs-TBA-15 gate electrode are very different, as stated before, are present fingerprints of all expected elements in the aptamer composed of a chain of phosphates (P) and sugar with a sequence of 9 guanine and 6 thymine basis (C, O, N), linked with a thiol group (S). As can be seen from comparison with previous results lineshape of C1s and O1s peak is quite different, suggesting presence of different chemical species (Figure 4.16).

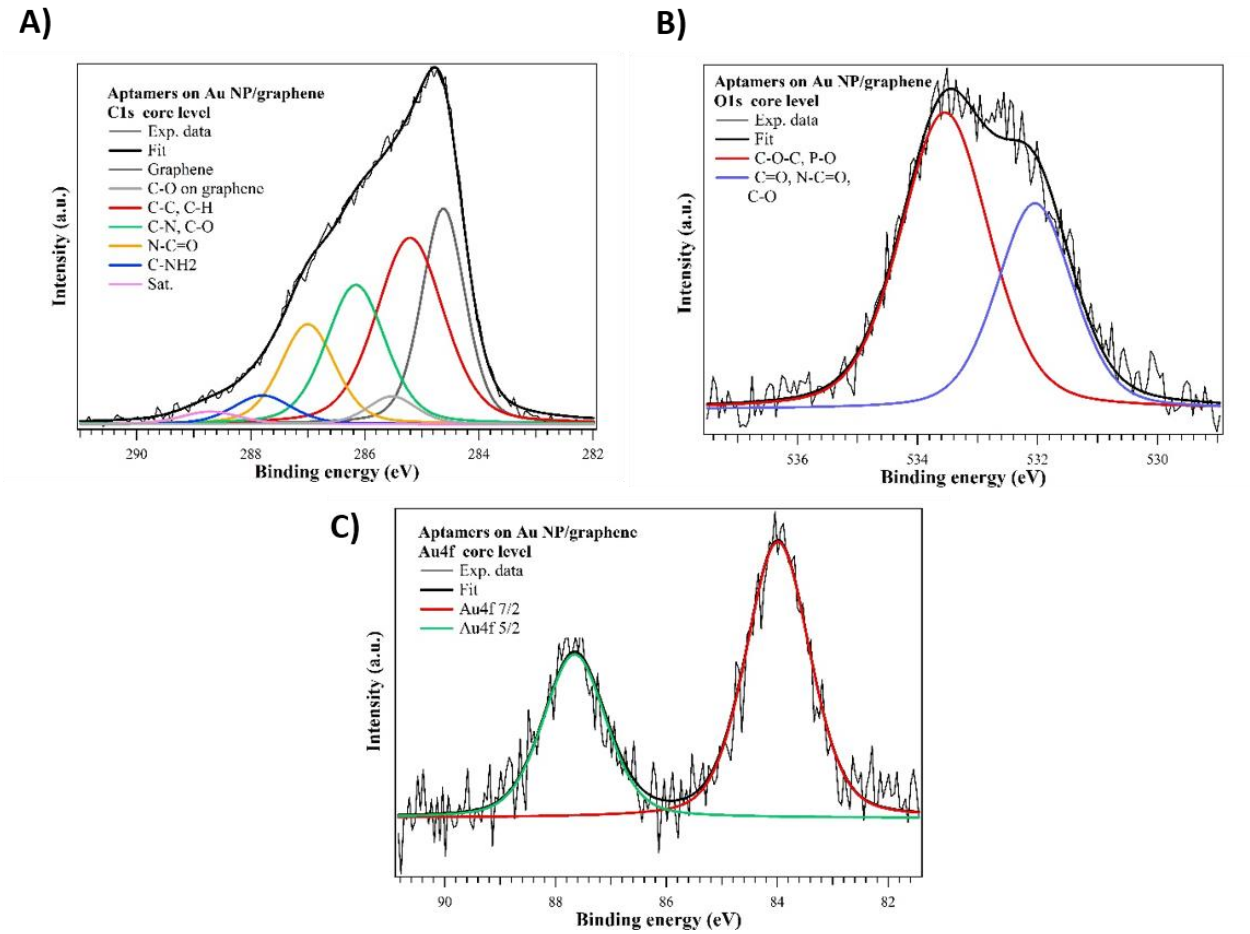

Figure 4.16: *a) C1s, b) O1s and c) Au4f core levels for PMLG-AuNPs-TBA-15. Single components are described in the legends.*

C1s peak has a complex lineshape, suggesting presence of several chemical species (Fig. 4.16a). A signal coming from the graphene layer is still detectable at 284.62eV, at the expected BE value in absence of charging effects, as well as a small component from C-O species on graphene at 285.52eV. Peak full width at half maximum (FWHM) is about 0.9eV for both features, thus significantly lower than for virgin graphene on LDPE sample. A large (1.3eV) and intense structure is located at 285.21eV, it can be attributed to C-C and C-H species present in the alkyl chain, sugar groups, thymine and guanine basis. Their different chemical properties lead in C1s to the most intense component, as expected from the large number of these carbon atoms, but broad, due to the impossibility to discriminate the small BE differences of C-C and C-H in all groups.[284] A second feature is present at 286.16eV, located at about +1eV from the main C-C/C-H peak and thus related to C-N species in the two basis,[285] and C-O in sugar.[286] Other two peaks, with decreasing intensity, are located at 287.00 and 287.79eV, they can be attribute to carbon in N-C=O bond in guanine and

thymine[287] and in C-NH2 in guanine.[278] A last peak is located at 288.71eV and it could be to a shake up electron promotion process typical of large molecules.

O1s peak analysis (Fig. 4,16b) shows to broad (FWHM ~1.6eV) components located at 532.04 and 533.54eV. Differently from C1s peak, the deconvolution of O1s peak is always more difficult and suddenly not discussed in details in literature.[288,289] However, the two peaks are due to the superposition of the different oxygen chemical species, showing similar BE. In particular, the component at 532.04eV can be due to oxygen in C=O and N-C=O in guanine and thymine, while a very small contribution from C-O on graphene can not be excluded. Peak at higher BE can be identified as oxygen in C-O-C bond and in phosphates group.[290]

Concerning gold main XPS signal, the higher concentration with respect to the previous sample leads to a better signal to noise ratio, with the two doublet peaks well defined at the expected BE of 84eV for Au4f 7/2 (Fig. 4.16c). In fact, the functionalized surface does not show any charging effect during XPS analysis, probably due to the higher gold content improving electrical conductivity with respect to previous sample.

Aptamers functionalization process should occur by interaction of gold with the thiol group. The S2p 3/2 peak (S2p is a doublet with a spin orbit splitting of 1.16eV) is located at 161.80eV and very broad (1.8eV), as shown in Fig. 4.17a. Although the presence of a second doublet around 162.5eV can not be excluded due to the low signal to noise ratio, the measured BE is typical of a surface bound Au-thiolate species,[291] while unbound thiols should be around 163eV. This means that all or, at least, most of aptamers are covalently bound to Au NPs, a further evidence of an achieved functionalization process.

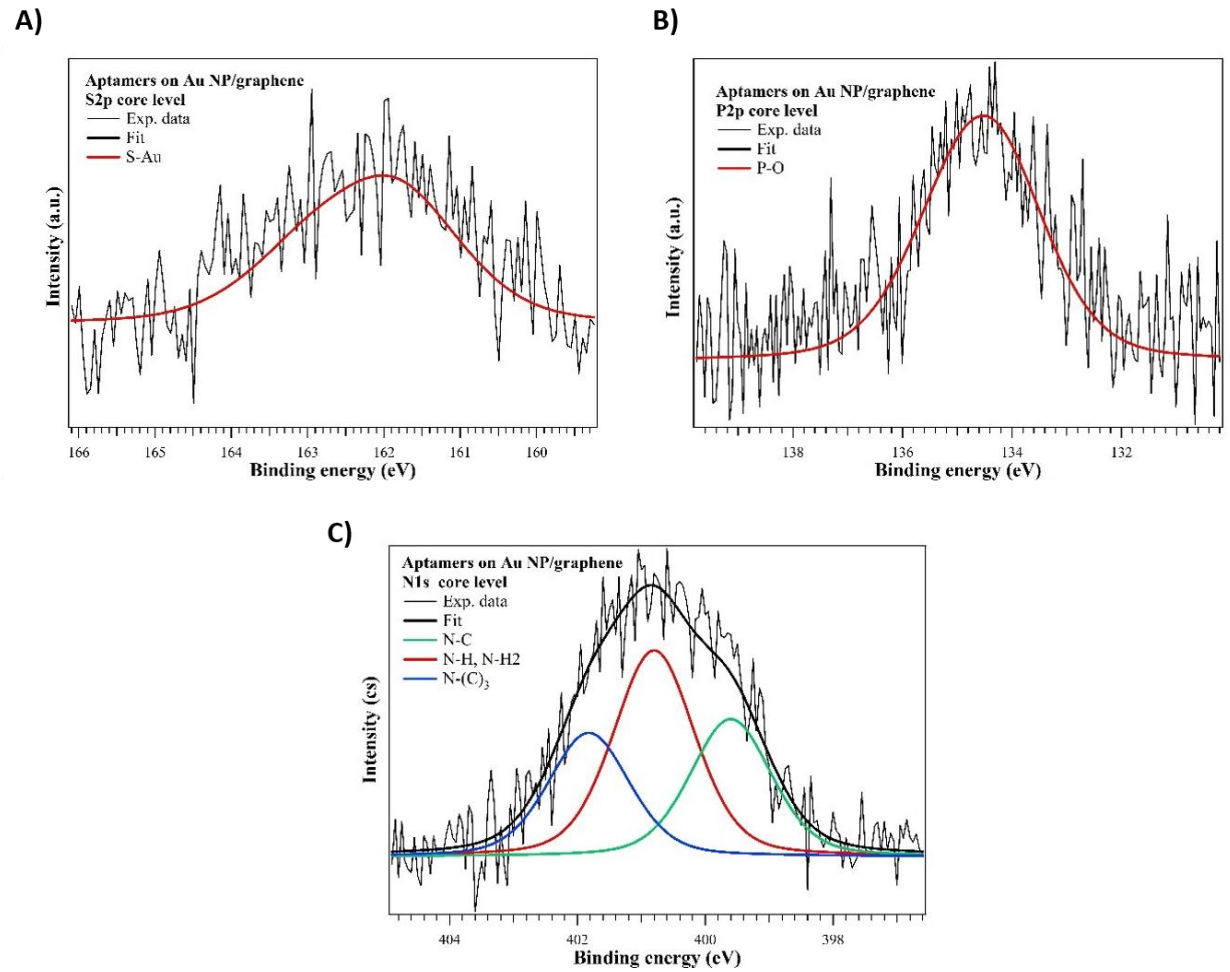

Figure 4.17: *a) S2p, b) P2p and c) N1s core levels for PMLG-AuNPs-TBA-15. Single components are described in the legends.*

P2p core level (Fig. 4.17b) is characterized by a single peak, a doublet with spin orbit splitting of 0.84eV, located at 134.29eV and related to phosphates groups.[290,292]

N1s core level shows presence of three main features (Fig. 4.17c), all being representative of chemical species in guanine and thymine. A first one is located at 399.6eV and is typical for nitrogen in aromatic rings, the most intense peak at 400.82 is representative of N-H and N-H2 groups, the most frequent type of nitrogen atom. The third one at 401.82eV can be attributed to nitrogen atom in graphitic environment, i.e. atoms linking each basis with the sugar group.[293,294]

4.7 DETECTION OF THROMBIN

After the optimization of aptamers concentration on the gate electrode surface, the aptasensor response was evaluated performing transfer characterizations after the interaction between aptamers and thrombin. Transfer curves have been carried out with the same parameters and electrolyte (PBS 10 mM) employed for the previous characterizations and a calibration curve was built testing different thrombin concentrations. One example of the obtained OECT response after the thrombin binding by aptamers on the gate electrode is reported in Fig. 4.18 where it is compared with the OECT responses recorded in each steps required for the biosensor construction.

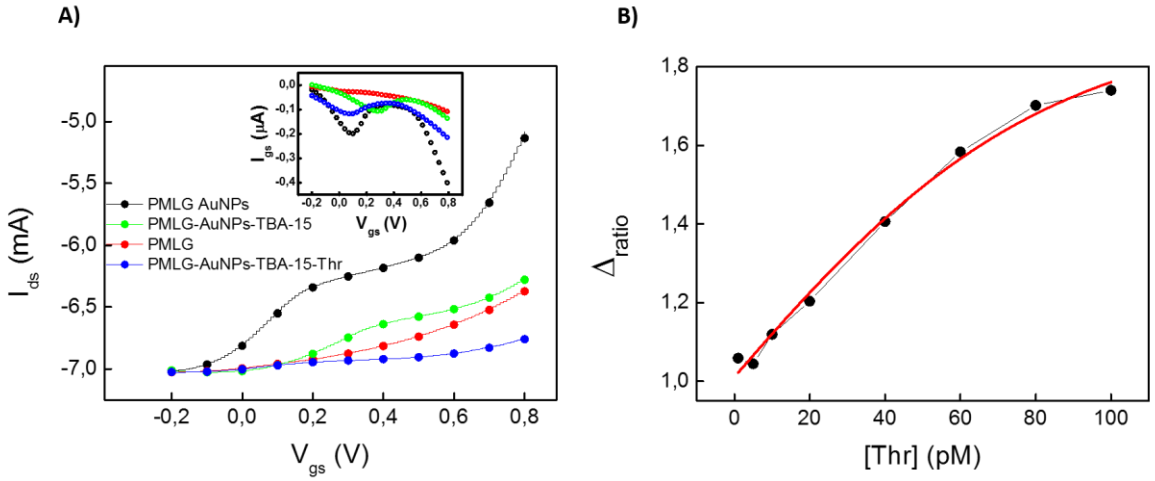

Figure 4.18: *a) I_{gs} (in the inset) and I_{ds} variation performed by the thrombin-incubated TBA-15 modified AuNPs-PMLG electrode (blue lines), compared with the I_{gs} and I_{ds} modulation obtained with the bare PMLG (red lines), the AuNPs-PMLG (black lines) and the un-folded TBA-15 modified AuNPs-PMLG gate electrode (green lines) gate electrodes. b) Calibration curve reported as the variation of the Δ_{ratio} in function of different Thr concentrations: : the fitting was performed through a four parameters logistic equation (red line).*

As it is shown in the inset, the I_{gs} curve (blue line), recorded after the thrombin interaction, shows the same trend of the one measured with the AuNPs-PMLG gate electrode (black line). The gate current, in fact, shows a peak centered at 0.1 V, as in the case of AuNPs-PMLG electrode, but with a definitely lower intensity. As mentioned before, this is possibly due to the change of the aptamers conformation during the recognition event where they undergo a transformation from a random flexible structure to a rigid one. During the folding, weak interactions between aptamers and thrombin leading to a complex TBA-15-Thr and moving the ferrocene linked to one of aptamer end away from the gate electrode surface. The removal of the redox label from the surface of the gate electrode blocks the electron transfer between them and this in turns leads to the disappearance of the I_{gs} peak at 0.3 V,

which in the previous characterization was ascribed to the charge transfer between TBA-15 and AuNPs-PMLG gate electrode. As a result, the resulting I_{ds} modulation (blue line) decreases from the one of the bare PMLG gate electrode and drives the OECT response (red line) and this is due to the steric hindrance, caused by the presence of thrombin, which reduces the exposition of the gate electrode surface to the electrolyte making the communication with the channel difficult. This marked variation in the transfer curves in terms of both shape and I_{ds} modulation can be considered as the marker of the thrombin detection giving the wanted detection of the molecules of interest.

To evaluate the linear range and the detection limit of the OECT based biosensor against thrombin, the calibration curve was built testing different thrombin concentrations (from 1 to 100 pM). It is shown in Fig. 4.18b, where the device response, expressed as Δ_{ratio} is reported as function of the thrombin concentration.

The Δ_{ratio} was defined according the following equations:

$$\Delta_{ratio} = {}^{\Delta_s}\!/_{\Delta_p} \tag{4.9}$$

$$\Delta_s = I_{ds}\,(TBA_{15} - Thr) - I_{ds}\,(AuNPs - PMLG) \tag{4.10}$$

$$\Delta_p = I_{ds}\,(TBA_{15}) - I_{ds}\,(AuNPs - PMLG) \tag{4.11}$$

where I_{ds} is the channel current measured at V_{gs} = 0.8 V, I_{ds} (TBA-15-Thr) is the current channel measured after the incubation of thrombin, I_{ds} (TBA-15) is the current channel measured after aptamers immobilization and I_{ds} (AuNPs-PMLG) is the current channel measured with the AuNPs-PMLG electrode in absence of TBA-15 and it represents the blank measure. From its definition, Δ_{ratio} is the most precise representation of the thrombin coordination contribution to the OECT sensor current since it excludes from the analysis effects coming from aptamers, AuNps and gate substrate. As can be seen a sigmoidal trend is obtained and it is fitted using a four parameters logistic equation according to the following formula:

$$y = A_2 + \left[\frac{(A_1 - A_2)}{1 + \left(\frac{x}{Ec50}\right)^b}\right] \tag{4.12}$$

here y corresponds to Δ_{ratio}, x is the thrombin concentration, A_1 and A_2 are the minima and the maximum analytical response, b represents the slope of the inflection point and Ec50 is the concentration leading to 50% of the maximum signal. This fit show a correlation R^2 of 0.99154 and Ec50 equal to 48.91 M. The limit of detection (LoD) of the device was calculated following the

IUPAC recommendations and applying the formula $\Delta_{blank} + 3\sigma$, where Δ_{blank} is the average of the OECT response for blank signal (obtained in absence of aptamers), σ is the standard deviation related to the blank measures and 3 is a numerical factor chosen in order to have a confidence level of 99.86%. According to the IUPAC definition the LoD value that our systems can express and with confidence detect is 5.000 ± 0.087 pM. This value, despite is not the absolute best value reported in literature of for thrombin detection, represents a LoD well below the the physiological concentration of thrombin that can vary from 1 nM to over 500 nM.

To further prove the quality our sensor, its selectivity was tested with the most abundant plasma protein, namely the bovine serum albumin (BSA) that co-exist with thrombin in blood and it is normally present with concentration of about 500 µM. To evaluate the selectivity of the aptasensor in the worst conditions, thus when the interfering protein is present at high concentration, the relative response of OECT was tested in presence of BSA with a concentration of 1 mM. The Δ_{ratio} in presence of BSA was estimated and it was divided by the Δ_{ratio} relative to 100 pM of thrombin and it was multiplied per 100. In addition to the BSA and thrombin relative responses, shown in the histogram reported in Fig. 4.19, a blank measure was performed after the interaction of 100 pM of thrombin with an AuNPs-PMLG gate electrode without aptamers functionalization. The evaluated OECT response for the blank measure reported as Δ_{ratio} was divided by the Δ_{ratio} relative to 100 pM of thrombin and it was multiplied per 100.

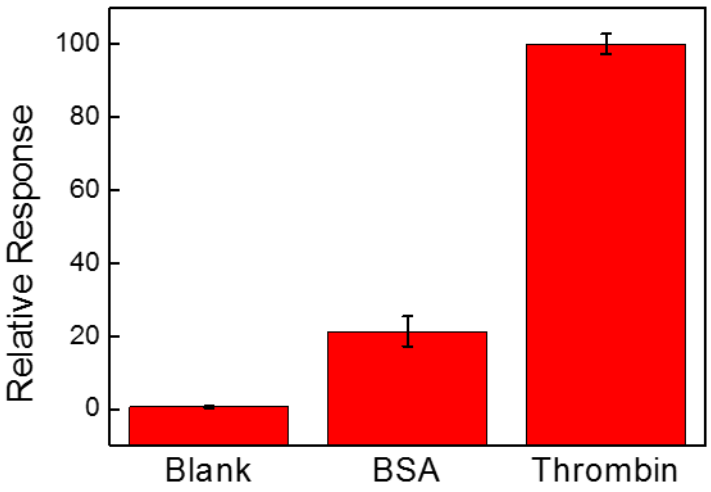

Figure 4.19: *Evaluation of the selectivity of the OECT-based aptasensor: the signal recorded in presence of higher concentration of BSA (1 mM) is compared with the electrical response obtained in presence of very low concentration of Thr (100 pM). An evaluation of possible no-specific interactions between Thr and the AuNPs-PMLG gate electrode surface is also evaluated performing a blank measure.*

In conclusion, OECT aptasensor selectively recognize thrombin, with a relative response of almost 100% even if some non-specific binding of BSA can be observed with a relative response of about 20%. However, it is worth noting that this very small contribution has been obtained considering a BSA concentration is double with respect to the physiological conditions and in general is several orders of magnitude higher than the thrombin concentration. Moreover, as expected, the blank measure shows a very small signal related to un-specific interaction between thrombin with the surface of the AuNPs-PMLG gate electrode in absence of aptamers giving a relative response of about 0.4 %. This, in turns, demonstrates the absence of no-specific interactions with the protein and the gate electrode, ensuring once more that the signals obtained from this biosensor are due by far to the selective recognition and interaction between the TBA-15 aptamers and the thrombin.

CONCLUSIONS

Within the fast growing field of Organic Electronics, this work explores electrochemical devices based on organic conductors for the detection of molecules and biologically systems of interest for medical diagnosys and possibly in the perspective of theragnostics. The idea of fabricating biosensors based on this type of transistors aims at exploiting several advantages related to their distinctive features. First of all, the biocompatibility and mechanical flexibility of PEDOT:PSS, which is the key material for these devices, guarantees their integration to biological systems having a negligible impact on cells and tissues. Furthermore, OECTs have an electrical response to both ionic and electronic transport that enables interfacing the biological universe, where ions play a dominant role, with the world of electronics. Another fundamental property is, together with the transduction, they provide anhigh amplification performance, which responds to the basic need of increasing the signal to noise ratio while lowering the detection limit, hence achieving increased sensitivity. All together this approach is promising to give a quite relevant contribution to the growth of the innovative field of Organic Bioelectronic. The aim of this work has been to contribute with an innovative approach to the eminent role of organic bioelectronics in diagnostic and actuator applications.

In particular this project was simultaneously focused on both enhancing the OECTs performance as transduction systems in monitoring biomarkers and reducing nonspecific response or limitation in recognition. In this respect, a significant innovation is the employment, of aptamers, for the first time in combination with OECTs, instead of antibodies for the specific binding of proteins. Even if aptamer based technologies have been only recently explored, they will gain more and more attention as they entails the use of synthetically generated reagents in place of highly complex biomolecules obtained by living organisms and therefore often variable and requiring quite complicated bio-processes.

Keeping all this in mind, for the first time in this work, we have combined OECTs have been combined for the first time with aptamers, which show several advantages such as being highly selective to a wide range of specific targets thanks to the possibility of an *in-vitro* synthesis of aptamers specific for any given molecule. Both their chemical synthesis and the *in-vitro* selection has

been successfully exploited in this project to modify the oligonucleotides sequence with a redox label, allowing a conformation change aptasensors having a “signal off” mechanism.

Furthermore, we developed the innovative idea of combining in the gate electrode the capacitive effect of graphene with the electrocatalytic activity of gold nanoparticles paving the way to highly sensitive OECTs eliminating the limits typical of the interactions between metal electrodes and biological systems. The large specific surface area of nanoparticles provides also the immobilization of a larger numbers of aptamers as signal molecules on the surface of the electrode, making them a useful alternative for signal amplification.

These relevant device innovations were critical to successfully monitoring thrombin, used as a significant test case, down to limit of detections recognizing it in physiological environment showing a highest selectivity and the absence of nonspecific interactions.

These relevant results qualify OECTs as very promising for biomedical applications in a perspective of biocompatible, cheap and easy to handle systems that could contribute to the development of point-of-care diagnostics and possibly theragnostics. We believe that our approach could be now expanded to a variety of different biomarkers and hence paving the way to a variety of different bio-medical applications.

BIBLIOGRAPHY

1. Atkinson, A. J., Colburn, W. A., DeGruttola, V. G., DeMets, D. L., Downing, G. J., Hoth, D. F., Oates, J. A., Peck, C. C., Schooley, R. T., Spilker, B. A., Woodcock, J. & Zeger, S. L. Biomarkers and surrogate endpoints: Preferred definitions and conceptual framework. *Clinical Pharmacology and Therapeutics* (2001).

2. Frank, R. & Hargreaves, R. Clinical biomarkers in drug discovery and development. *Nature Reviews Drug Discovery* (2003).

3. FDA-NIH Biomarker Working Group. BEST (Biomarkers, EndpointS, and other Tools) Resource. *BEST (Biomarkers, EndpointS, other Tools) Resour.* (2016).

4. De La Rica, R. & Stevens, M. M. Plasmonic ELISA for the ultrasensitive detection of disease biomarkers with the naked eye. *Nat. Nanotechnol.* (2012).

5. Alberti, D., van't Erve, M., Stefania, R., Ruggiero, M. R., Tapparo, M., Geninatti Crich, S. & Aime, S. A Quantitative Relaxometric Version of the ELISA Test for the Measurement of Cell Surface Biomarkers. *Angew. Chemie Int. Ed.* **53**, 3488–3491

6. Chiswick, E. L., Duffy, E., Japp, B. & Remick, D. Detection and Quantification of Cytokines and Other Biomarkers. *Methods Mol. Biol.* **844**, 15–30 (2012).

7. Lee, H., Park, J.-E. & Nam, J.-M. Bio-barcode gel assay for microRNA. *Nat. Commun.* **5**, 3367 (2014).

8. Garcia-Schwarz, G. & Santiago, J. G. Rapid High-Specificity microRNA Detection Using a Two-stage Isotachophoresis Assay. *Angew. Chemie Int. Ed.* **52**, 11534–11537

9. Bakry, R., Huck, C. W., Najam-ul-Haq, M., Rainer, M. & Bonn, G. K. Recent advances in capillary electrophoresis for biomarker discovery. *J. Sep. Sci.* **30**, 192–201

10. Goldsmith, S. Radioimmunoassay: Review of basic principles. *Semin. Nucl. Med.* **5**, 125–152 (1975).

11. Thévenot, D. R., Toth, K., Durst, R. A. & Wilson, G. S. Electrochemical biosensors: recommended definitions and classification1International Union of Pure and Applied Chemistry: Physical Chemistry Division, Commission I.7 (Biophysical Chemistry); Analytical Chemistry Division, Commission V.5 (Electroanalytical. *Biosens. Bioelectron.* **16**, 121–131 (2001).

12. Clark, L. C. & Lyons, C. Electrode systems for continuous monitoring in cardiovascular surgery. *Ann. N. Y. Acad. Sci.* (1962).

13. Turner, Anthony PF; Wilson, G. S. *Biosensors Fundamentals and Applications*. *Journal of Chemical Information and Modeling* (1989).

14. Morrison, D. W. G., Dokmeci, M. R., Demirci, U. & Khademhosseini, A. Clinical Applications of Micro- and Nanoscale Biosensors. in *Biomedical Nanostructures* (2007).

15. Karunakaran, C., Rajkumar, R. & Bhargava, K. Introduction to Biosensors. *Biosensors and Bioelectronics* (2015).

16. Perumal, V. & Hashim, U. Advances in biosensors: Principle, architecture and applications. *Journal of Applied Biomedicine* (2014).

17. Karlsson, R., Michaelsson, A. & Mattsson, L. Kinetic analysis of monoclonal antibody-antigen

interactions with a new biosensor based analytical system. *J. Immunol. Methods* **145**, 229–240 (1991).

18. Bush, D. L. & Rechnitz, G. A. Monoclonal antibody biosensor for antigen monitoring. *Anal. Lett.* **20**, 1781–1790 (1987).

19. Katz, E., Bückmann, A. F. & Willner, I. Self-powered enzyme-based biosensors. *J. Am. Chem. Soc.* **123**, 10752–10753 (2001).

20. Wilson, G. S. & Hu, Y. Enzyme-based biosensors for in vivo measurements. *Chem. Rev.* **100**, 2693–2704 (2000).

21. Amine, A., Mohammadi, H., Bourais, I. & Palleschi, G. Enzyme inhibition-based biosensors for food safety and environmental monitoring. *Biosens. Bioelectron.* **21**, 1405–1423 (2006).

22. Zhai, J., Cui, H. & Yang, R. DNA based biosensors. *Biotechnol. Adv.* **15**, 43–58 (1997).

23. Labuda, J., Brett, A. M. O., Evtugyn, G., Fojta, M., Mascini, M., Ozsoz, M., Palchetti, I., Paleček, E. & Wang, J. Electrochemical nucleic acid-based biosensors: concepts, terms, and methodology (IUPAC Technical Report). *Pure Appl. Chem.* **82**, 1161–1187 (2010).

24. Wang, P., Xu, G., Qin, L., Xu, Y., Li, Y. & Li, R. Cell-based biosensors and its application in biomedicine. in *Sensors and Actuators, B: Chemical* (2005).

25. Ziegler, C. Cell-based biosensors. *Fresenius' Journal of Analytical Chemistry* (2000).

26. Hermann, T. & Patel, D. J. Adaptive recognition by nucleic acid aptamers. *Science* (2000).

27. Scheller, F. W., Wollenberger, U., Warsinke, A. & Lisdat, F. Research and development in biosensors. *Current Opinion in Biotechnology* (2001).

28. Marazuela, D. & Moreno-Bondi, M. C. Fiber-optic biosensors--an overview. *Anal. Bioanal. Chem.* (2002).

29. Robertson, D. L. & Joyce, G. F. Selection in vitro of an RNA enzyme that specifically cleaves single-stranded DNA. *Nature* (1990).

30. Ellington, A. D. & Szostak, J. W. In vitro selection of RNA molecules that bind specific ligands. *Nature* (1990).

31. Tuerk, C. & Gold, L. Systematic evolution of ligands by exponential enrichment: RNA ligands to bacteriophage T4 DNA polymerase. *Science (80-.).* (1990).

32. Nimjee, S. M., Rusconi, C. P. & Sullenger, B. A. Aptamers: An Emerging Class of Therapeutics. *Annu. Rev. Med.* (2005).

33. Sun, H. & Zu, Y. A Highlight of recent advances in aptamer technology and its application. *Molecules* (2015).

34. Song, S., Wang, L., Li, J., Fan, C. & Zhao, J. Aptamer-based biosensors. *TrAC - Trends Anal. Chem.* (2008).

35. O'Sullivan, C. K. Aptasensors – the future of biosensing? *Anal. Bioanal. Chem.* (2002).

36. Song, K. M., Lee, S. & Ban, C. Aptamers and their biological applications. *Sensors* (2012).

37. Cox, J. C., Rudolph, P. & Ellington, A. D. Automated RNA selection. *Biotechnol. Prog.* (1998).

38. Thiviyanathan, V. & Gorenstein, D. G. Aptamers and the Next Generation of Diagnostic Reagents. *Proteomics. Clin. Appl.* **6**, 563–573 (2012).

39. Gebhardt, K., Shokraei, A., Babaie, E. & Lindqvist, B. H. RNA aptamers to S-adenosylhomocysteine: Kinetic properties, divalent cation dependency, and comparison with anti-S-adenosylhomocysteine antibody. *Biochemistry* (2000).

40. Wilson, D. S., Keefe, A. D. & Szostak, J. W. The use of mRNA display to select high-affinity protein-binding peptides. *Proc. Natl. Acad. Sci.* (2001).

41. Shangguan, D., Li, Y., Tang, Z., Cao, Z. C., Chen, H. W., Mallikaratchy, P., Sefah, K., Yang, C. J. & Tan, W. Aptamers evolved from live cells as effective molecular probes for cancer study. *Proc. Natl. Acad. Sci.* (2006).

42. Liu, M., Yu, X., Chen, Z., Yang, T., Yang, D., Liu, Q., Du, K., Li, B., Wang, Z., Li, S., Deng, Y. & He, N. Aptamer selection and applications for breast cancer diagnostics and therapy. *Journal of Nanobiotechnology* (2017).

43. Musumeci, D., Platella, C., Riccardi, C., Moccia, F. & Montesarchio, D. Fluorescence Sensing Using DNA Aptamers in Cancer Research and Clinical Diagnostics. *Cancers (Basel).* **9**, 174 (2017).

44. Cerchia, L. & de Franciscis, V. Targeting cancer cells with nucleic acid aptamers. *Trends in Biotechnology* (2010).

45. Riccardi, C., Russo Krauss, I., Musumeci, D., Morvan, F., Meyer, A., Vasseur, J. J., Paduano, L. & Montesarchio, D. Fluorescent Thrombin Binding Aptamer-Tagged Nanoparticles for an Efficient and Reversible Control of Thrombin Activity. *ACS Appl. Mater. Interfaces* (2017).

46. Abdulhalim, I., Zourob, M. & Lakhtakia, A. Overview of Optical Biosensing Techniques. in *John Wiley & Sons, Ltd.* 34 (American Cancer Society, 2007).

47. Damborský, P., Švitel, J. & Katrlík, J. Optical biosensors. *Essays Biochem.* **60**, 91–100 (2016).

48. Fan, X., White, I. M., Shopova, S. I., Zhu, H., Suter, J. D. & Sun, Y. Sensitive optical biosensors for unlabeled targets: A review. *Analytica Chimica Acta* (2008).

49. Charlton, S. C., Johnson, L. D., Musho, M. K. & Slomski, D. Electrochemical biosensor. (1998).

50. Skotheim, T. A., Okamoto, Y. & Hale, P. D. Electrochemical biosensor based on immobilized enzymes and redox polymers. (1992).

51. Say, J., Tomasco, M. F., Heller, A., Gal, Y., Aria, B., Heller, E., Plante, P. J. & Vreeke, M. S. Process for producing an electrochemical biosensor. (2000).

52. Vo-Dinh, T. & M. Cullum, B. *Biosensors and Biochips: Advances in Biological and Medical Diagnostics*. *Fresenius' journal of analytical chemistry* **366**, (2000).

53. Liu, J. & Lu, Y. Adenosine-dependent assembly of aptazyme-functionalized gold nanoparticles and its application as a colorimetric biosensor. *Anal. Chem.* **76**, 1627–1632 (2004).

54. Liu, Y., Yuan, M., Qiao, L. & Guo, R. An efficient colorimetric biosensor for glucose based on peroxidase-like protein-Fe3O4 and glucose oxidase nanocomposites. *Biosens. Bioelectron.* **52**, 391–396 (2014).

55. Park, J. H., Byun, J. Y., Mun, H., Shim, W. B., Shin, Y. B., Li, T. & Kim, M. G. A regeneratable, label-free, localized surface plasmon resonance (LSPR) aptasensor for the detection of ochratoxin A. *Biosens. Bioelectron.* (2014).

56. Ostatná, V., Vaisocherová, H., Homola, J. & Hianik, T. Effect of the immobilisation of DNA aptamers on the detection of thrombin by means of surface plasmon resonance. *Anal. Bioanal. Chem.* (2008).

57. Chang, K., Pi, Y., Lu, W., Wang, F., Pan, F., Li, F., Jia, S., Shi, J., Deng, S. & Chen, M. Label-free and high-sensitive detection of human breast cancer cells by aptamer-based leaky surface acoustic wave biosensor array. *Biosens. Bioelectron.* (2014).

58. Yao, C., Zhu, T., Qi, Y., Zhao, Y., Xia, H. & Fu, W. Development of a quartz crystal microbalance biosensor with aptamers as bio-recognition element. *Sensors* (2010).

59. Dong, Z.-M. & Zhao, G.-C. Quartz Crystal Microbalance Aptasensor for Sensitive Detection of Mercury(II) Based on Signal Amplification with Gold Nanoparticles. *Sensors* (2012).

60. Lim, Y. C., Kouzani, A. Z., Duan, W., Dai, X. J., Kaynak, A. & Mair, D. A surface-stress-based microcantilever aptasensor. *IEEE Trans. Biomed. Circuits Syst.* (2014).

61. Radi, A. E., Acero Sánchez, J. L., Baldrich, E. & O'Sullivan, C. K. Reagentless, reusable, ultrasensitive electrochemical molecular beacon aptasensor. *J. Am. Chem. Soc.* (2006).

62. Sassolas, A., Blum, L. J. & Béatrice, D. L. B. Electrochemical aptasensors. *Electroanalysis* **21**, 1237–1250 (2009).

63. Willner, I. & Zayats, M. Electronic aptamer-based sensors. *Angewandte Chemie - International Edition* (2007).

64. Zhang, Y. & Sun, X. A novel fluorescent aptasensor for thrombin detection: Using poly(m-phenylenediamine) rods as an effective sensing platform. *Chem. Commun.* (2011).

65. Li, T., Wang, E. & Dong, S. Chemiluminescence thrombin aptasensor using high-activity DNAzyme as catalytic label. *Chem. Commun.* (2008).

66. Hong, P., Li, W. & Li, J. Applications of aptasensors in clinical diagnostics. *Sensors* (2012).

67. Ikebukuro, K., Kiyohara, C. & Sode, K. Electrochemical detection of protein using a double aptamer sandwich. *Anal. Lett.* (2004).

68. Pasinszki, T., Krebsz, M., Tung, T. T. & Losic, D. Carbon Nanomaterial Based Biosensors for Non-Invasive Detection of Cancer and Disease Biomarkers for Clinical Diagnosis. *Sensors* (2017).

69. Grieshaber, D., MacKenzie, R., Vörös, J. & Reimhult, E. Electrochemical biosensors - Sensor principles and architectures. *Sensors* (2008).

70. Strakosas, X., Bongo, M. & Owens, R. M. The organic electrochemical transistor for biological applications. *Journal of Applied Polymer Science* (2015).

71. Simon, D. T., Gabrielsson, E. O., Tybrandt, K. & Berggren, M. Organic Bioelectronics: Bridging the Signaling Gap between Biology and Technology. *Chemical Reviews* (2016).

72. Rivnay, J., Owens, R. M. & Malliaras, G. G. The rise of organic bioelectronics. *Chemistry of Materials* (2014).

73. Berggren, M. & Richter-Dahlfors, A. Organic bioelectronics. *Adv. Mater.* (2007).

74. Pope, M. & Swenberg, C. E. *Electronic Processes in Organic Crystals and Polymers*. *Oxford University Press USA 2nd edition* (1999).

75. Shirakawa, H., Louis, E. J., MacDiarmid, A. G., Chiang, C. K. & Heeger, A. J. Synthesis of electrically conducting organic polymers: Halogen derivatives of polyacetylene, (CH)x. *J. Chem. Soc. Chem. Commun.* (1977).

76. Borsenberger, P. M. *Organic photoreceptors for xerography*. **59**, (CRC Press, 1998).

77. Tang, C. W. & Vanslyke, S. A. Organic electroluminescent diodes. *Appl. Phys. Lett.* (1987).

78. Friend, R. H., Gymer, R. W., Holmes, A. B., Burroughes, J. H., Marks, R. N., Taliani, C., Bradley, D. D. C., Dos Santos, D. A., Brédas, J. L., Lögdlund, M. & Salaneck, W. R. Electroluminescence in conjugated polymers. *Nature* (1999).

79. Owens, R. M. & Malliaras, G. G. Organic electronics at the interface with biology. *MRS Bull.* (2010).

80. Tyler McQuade, D., Pullen, A. E. & Swager, T. M. Conjugated polymer-based chemical sensors. *Chem. Rev.* (2000).

81. Gerard, M., Chaubey, A. & Malhotra, B. D. Application of conducting polymers to biosensors. *Biosensors and Bioelectronics* (2002).

82. Bartlett, P. N. & Birkin, P. R. The application of conducting polymers in biosensors. *Synth. Met.* **61**,

15–21 (1993).

83. Yu, Z., Li, H., Zhang, X., Liu, N., Tan, W., Zhang, X. & Zhang, L. Facile synthesis of NiCo2O4@Polyaniline core-shell nanocomposite for sensitive determination of glucose. *Biosens. Bioelectron.* (2016).

84. Fusco, G., Gallo, F., Tortolini, C., Bollella, P., Ietto, F., De Mico, A., D'Annibale, A., Antiochia, R., Favero, G. & Mazzei, F. AuNPs-functionalized PANABA-MWCNTs nanocomposite-based impedimetric immunosensor for 2,4-dichlorophenoxy acetic acid detection. *Biosens. Bioelectron.* (2017).

85. Spain, E., Keyes, T. E. & Forster, R. J. Polypyrrole-gold nanoparticle composites for highly sensitive DNA detection. *Electrochim. Acta* (2013).

86. Jiang, H., Zhang, A., Sun, Y., Ru, X., Ge, D. & Shi, W. Poly(1-(2-carboxyethyl)pyrrole)/polypyrrole composite nanowires for glucose biosensor. *Electrochim. Acta* **70**, 278–285 (2012).

87. Shrestha, B. K., Ahmad, R., Mousa, H. M., Kim, I. G., Kim, J. I., Neupane, M. P., Park, C. H. & Kim, C. S. High-performance glucose biosensor based on chitosan-glucose oxidase immobilized polypyrrole/Nafion/functionalized multi-walled carbon nanotubes bio-nanohybrid film. *J. Colloid Interface Sci.* (2016).

88. Kergoat, L., Piro, B., Simon, D. T., Pham, M.-C., Noël, V. & Berggren, M. Detection of Glutamate and Acetylcholine with Organic Electrochemical Transistors Based on Conducting Polymer/Platinum Nanoparticle Composites. *Adv. Mater.* **26**, 5658–5664

89. Sotzing, G. A., Briglin, S. M., Grubbs, R. H. & Lewis, N. S. Preparation and Properties of Vapor Detector Arrays Formed from Poly(3,4-ethylenedioxy)thiophene−Poly(styrene sulfonate)/Insulating Polymer Composites. *Anal. Chem.* **72**, 3181–3190 (2000).

90. Abas\iyan\ik, M. F. & \cSenel, M. *Immobilization of glucose oxidase on reagentless ferrocene-containing polythiophene derivative and its glucose sensing application*. *Journal of Electroanalytical Chemistry* **639**, (Elsevier, 2010).

91. Wang, W., Cui, M., Song, Z. & Luo, X. An antifouling electrochemical immunosensor for carcinoembryonic antigen based on hyaluronic acid doped conducting polymer PEDOT. *RSC Adv.* (2016).

92. Uzun, S. D., Unlu, N. A., Sendur, M., Kanik, F. E., Timur, S. & Toppare, L. A novel promising biomolecule immobilization matrix: Synthesis of functional benzimidazole containing conducting polymer and its biosensor applications. *Colloids Surfaces B Biointerfaces* (2013).

93. Elkington, D., Cooling, N., Belcher, W., Dastoor, P. C. & Zhou, X. Organic Thin-Film Transistor (OTFT)-Based Sensors. *Electronics* **3**, 234–254 (2014).

94. Liao, C. & Yan, F. Organic semiconductors in organic thin-film transistor-based chemical and biological sensors. *Polym. Rev.* (2013).

95. Horowitz, G. Organic field-effect transistors. *Adv. Mater.* (1998).

96. Bao, Z. & Locklin, J. *Organic field-effect transistors*. (CRC press, 2007).

97. Nilsson, D., Chen, M., Kugler, T., Remonen, T., Armgarth, M. & Berggren, M. Bi-stable and dynamic current modulation in electrochemical organic transistors. *Adv. Mater.* (2002).

98. Khodagholy, D., Doublet, T., Quilichini, P., Gurfinkel, M., Leleux, P., Ghestem, A., Ismailova, E., Hervé, T., Sanaur, S., Bernard, C. & Malliaras, G. G. In vivo recordings of brain activity using organic transistors. *Nat. Commun.* (2013).

99. Kergoat, L., Piro, B., Berggren, M., Horowitz, G. & Pham, M. C. Advances in organic transistor-based biosensors: From organic electrochemical transistors to electrolyte-gated organic field-effect transistors. *Analytical and Bioanalytical Chemistry* (2012).

100. Nilsson, D., Kugler, T., Svensson, P. O. & Berggren, M. An all-organic sensor-transistor based on a novel electrochemical transducer concept printed electrochemical sensors on paper. *Sensors Actuators, B Chem.* (2002).

101. Parlak, O., Keene, S. T., Marais, A., Curto, V. F. & Salleo, A. Molecularly selective nanoporous membrane-based wearable organic electrochemical device for noninvasive cortisol sensing. *Sci. Adv.* (2018).

102. Gualandi, I., Marzocchi, M., Achilli, A., Cavedale, D., Bonfiglio, A. & Fraboni, B. Textile Organic Electrochemical Transistors as a Platform for Wearable Biosensors. *Sci. Rep.* (2016).

103. Zhang, S., Hubis, E., Tomasello, G., Soliveri, G., Kumar, P. & Cicoira, F. Patterning of Stretchable Organic Electrochemical Transistors. *Chem. Mater.* (2017).

104. Tarabella, G., Villani, M., Calestani, D., Mosca, R., Iannotta, S., Zappettini, A. & Coppede, N. A single cotton fiber organic electrochemical transistor for liquid electrolyte saline sensing. *J. Mater. Chem.* **22**, 23830–23834 (2012).

105. Khodagholy, D., Rivnay, J., Sessolo, M., Gurfinkel, M., Leleux, P., Jimison, L. H., Stavrinidou, E., Herve, T., Sanaur, S., Owens, R. M. & Malliaras, G. G. High transconductance organic electrochemical transistors. *Nat. Commun.* (2013).

106. Rivnay, J., Leleux, P., Ferro, M., Sessolo, M., Williamson, A., Koutsouras, D. A., Khodagholy, D., Ramuz, M., Strakosas, X., Owens, R. M., Benar, C., Badier, J. M., Bernard, C. & Malliaras, G. G. High-performance transistors for bioelectronics through tuning of channel thickness. *Sci. Adv.* (2015).

107. Matsue, T., Nishizawa, M., Sawaguchi, T. & Uchida, I. An enzyme switch sensitive to NADH. *J. Chem. Soc. Chem. Commun.* (1991).

108. Bolin, M. H., Svennersten, K., Nilsson, D., Sawatdee, A., Jager, E. W. H., Richter-Dahlfors, A. & Berggren, M. Active control of epithelial cell-density gradients grown along the channel of an organic electrochemical transistor. *Adv. Mater.* (2009).

109. Jimison, L. H., Tria, S. A., Khodagholy, D., Gurfinkel, M., Lanzarini, E., Hama, A., Malliaras, G. G. & Owens, R. M. Measurement of barrier tissue integrity with an organic electrochemical transistor. *Adv. Mater.* (2012).

110. Tria, S. A., Ramuz, M., Huerta, M., Leleux, P., Rivnay, J., Jimison, L. H., Hama, A., Malliaras, G. G. & Owens, R. M. Dynamic Monitoring of Salmonella typhimurium Infection of Polarized Epithelia Using Organic Transistors. *Adv. Healthc. Mater.* (2014).

111. Romeo, A., Tarabella, G., D'Angelo, P., Caffarra, C., Cretella, D., Alfieri, R., Petronini, P. G. & Iannotta, S. Drug-induced cellular death dynamics monitored by a highly sensitive organic electrochemical system. *Biosens. Bioelectron.* **68**, 791–797 (2015).

112. Romeo, A., Tarabella, G., D'Angelo, P., Caffarra, C., Cretella, D., Alfieri, R., Petronini, P. G. & Iannotta, S. Drug-induced cellular death dynamics monitored by a highly sensitive organic electrochemical system. *Biosens. Bioelectron.* (2015).

113. D'Angelo, P., Tarabella, G., Romeo, A., Giodice, A., Marasso, S., Cocuzza, M., Ravanetti, F., Cacchioli, A., Petronini, P. G. & Iannotta, S. Monitoring the adaptive cell response to hyperosmotic stress by organic devices. *MRS Commun.* (2017).

114. Lin, P., Yan, F., Yu, J., Chan, H. L. W. & Yang, M. The application of organic electrochemical transistors in cell-based biosensors. *Adv. Mater.* (2010).

115. Ramuz, M., Hama, A., Huerta, M., Rivnay, J., Leleux, P. & Owens, R. M. Combined optical and electronic sensing of epithelial cells using planar organic transistors. *Adv. Mater.* (2014).

116. Tarabella, G., D'Angelo, P., Cifarelli, A., Dimonte, A., Romeo, A., Berzina, T., Erokhin, V. & Iannotta, S. A hybrid living/organic electrochemical transistor based on the Physarum polycephalum cell endowed with both sensing and memristive properties. *Chem. Sci.* **6**, 2859–2868 (2015).

117. Nishizawa, M., Matsue, T. & Uchida, I. Penicillin Sensor Based on a Microarray Electrode Coated with pH-Responsive Polypyrrole. *Anal. Chem.* (1992).

118. Zhu, Z.-T., Mabeck, J. T., Zhu, C., Cady, N. C., Batt, C. A. & Malliaras, G. G. A simple poly(3{,}4-ethylene dioxythiophene)/poly(styrene sulfonic acid) transistor for glucose sensing at neutral pH. *Chem. Commun.* 1556–1557 (2004).

119. Tarabella, G., Pezzella, A., Romeo, A., D'Angelo, P., Coppedè, N., Calicchio, M., D'Ischia, M., Mosca, R. & Iannotta, S. Irreversible evolution of eumelanin redox states detected by an organic electrochemical transistor: En route to bioelectronics and biosensing. *J. Mater. Chem. B* (2013).

120. Tang, H., Yan, F., Lin, P., Xu, J. & Chan, H. L. W. Highly sensitive glucose biosensors based on organic electrochemical transistors using platinum gate electrodes modified with enzyme and nanomaterials. *Adv. Funct. Mater.* (2011).

121. Shim, N. Y., Bernards, D. A., Macaya, D. J., DeFranco, J. A., Nikolou, M., Owens, R. M. & Malliaras, G. G. All-plastic electrochemical transistor for glucose sensing using a ferrocene mediator. *Sensors* **9**, 9896–9902 (2009).

122. Cicoira, F., Sessolo, M., Yaghmazadeh, O., Defranco, J. A., Yang, S. Y. & Malliaras, G. C. Influence of device geometry on sensor characteristics of planar Organic electrochemical transistors. *Adv. Mater.* (2010).

123. He, R. X., Zhang, M., Tan, F., Leung, P. H. M., Zhao, X. Z., Chan, H. L. W., Yang, M. & Yan, F. Detection of bacteria with organic electrochemical transistors. *J. Mater. Chem.* (2012).

124. Kim, D.-J., Lee, N.-E., Park, J.-S., Park, I.-J., Kim, J.-G. & Cho, H. J. Organic electrochemical transistor based immunosensor for prostate specific antigen (PSA) detection using gold nanoparticles for signal amplification. *Biosens. Bioelectron.* (2010).

125. Lin, P., Luo, X., Hsing, I.-M. & Yan, F. Organic electrochemical transistors integrated in flexible microfluidic systems and used for label-free DNA sensing. *Adv. Mater.* **23**, 4035–4040 (2011).

126. Lin, P., Luo, X., Hsing, I. M. & Yan, F. Organic electrochemical transistors integrated in flexible microfluidic systems and used for label-free DNA sensing. *Adv. Mater.* (2011).

127. Liao, J., Lin, S., Liu, K., Yang, Y., Zhang, R., Du, W. & Li, X. Organic electrochemical transistor based biosensor for detecting marine diatoms in seawater medium. *Sensors Actuators, B Chem.* (2014).

128. So, H. M., Won, K., Kim, Y. H., Kim, B. K., Ryu, B. H., Na, P. S., Kim, H. & Lee, J. O. Single-walled carbon nanotube biosensors using aptamers as molecular recognition elements. *J. Am. Chem. Soc.* (2005).

129. Hammock, M. L., Knopfmacher, O., Naab, B. D., Tok, J. B.-H. & Bao, Z. Investigation of protein detection parameters using nanofunctionalized organic field-effect transistors. *ACS Nano* (2013).

130. Hagen, J. A., Kim, S. N., Bayraktaroglu, B., Leedy, K., Chávez, J. L., Kelley-Loughnane, N., Naik, R. R. & Stone, M. O. Biofunctionalized zinc oxide field effect transistors for selective sensing of riboflavin with current modulation. *Sensors* (2011).

131. Tarabella, G., Santato, C., Yang, S. Y., Iannotta, S., Malliaras, G. G. & Cicoira, F. Effect of the gate electrode on the response of organic electrochemical transistors. *Appl. Phys. Lett.* **97**, (2010).

132. He, R.-X., Zhang, M., Tan, F., Leung, P. H. M., Zhao, X.-Z., Chan, H. L. W., Yang, M. & Yan, F. Detection of bacteria with organic electrochemical transistors. *J. Mater. Chem.* **22**, 22072–22076 (2012).

133. Gualandi, I., Scavetta, E., Mariani, F., Tonelli, D., Tessarolo, M. & Fraboni, B. All poly(3,4-ethylenedioxythiophene) organic electrochemical transistor to amplify amperometric signals. *Electrochim. Acta* (2018).

134. Gualandi, I., Marzocchi, M., Scavetta, E., Calienni, M., Bonfiglio, A. & Fraboni, B. A simple all-

PEDOT: PSS electrochemical transistor for ascorbic acid sensing. *J. Mater. Chem. B* **3**, 6753–6762 (2015).

135. Kuila, T., Bose, S., Khanra, P., Mishra, A. K., Kim, N. H. & Lee, J. H. Recent advances in graphene-based biosensors. *Biosensors and Bioelectronics* (2011).

136. Novoselov, K. S., Geim, A. K., Morozov, S. V, Jiang, D., Zhang, Y., Dubonos, S. V, Grigorieva, I. V & Firsov, A. A. Electric field effect in atomically thin carbon films. *Science* (2004).

137. Novoselov, K. S., Fal'Ko, V. I., Colombo, L., Gellert, P. R., Schwab, M. G. & Kim, K. A roadmap for graphene. *Nature* (2012).

138. Bolotin, K. I., Sikes, K. J., Jiang, Z., Klima, M., Fudenberg, G., Hone, J., Kim, P. & Stormer, H. L. Ultrahigh electron mobility in suspended graphene. *Solid State Commun.* (2008).

139. Lee, C., Wei, X., Kysar, J. W. & Hone, J. Measurement of the elastic properties and intrinsic strength of monolayer graphene. *Science (80-.).* (2008).

140. Balandin, A. A., Ghosh, S., Bao, W., Calizo, I., Teweldebrhan, D., Miao, F. & Lau, C. N. Superior thermal conductivity of single-layer graphene. *Nano Lett.* (2008).

141. Cai, W., Zhu, Y., Li, X., Piner, R. D. & Ruoff, R. S. Large area few-layer graphene/graphite films as transparent thin conducting electrodes. *Appl. Phys. Lett.* **95**, 123115 (2009).

142. Li, X., Zhu, Y., Cai, W., Borysiak, M., Han, B., Chen, D., Piner, R. D., Colomba, L. & Ruoff, R. S. Transfer of large-area graphene films for high-performance transparent conductive electrodes. *Nano Lett.* (2009).

143. Huang, X., Yin, Z., Wu, S., Qi, X., He, Q., Zhang, Q., Yan, Q., Boey, F. & Zhang, H. Graphene-based materials: Synthesis, characterization, properties, and applications. *Small* (2011).

144. Reina, A., Jia, X., Ho, J., Nezich, D., Son, H., Bulovic, V., Dresselhaus, M. S. & Jing, K. Large area, few-layer graphene films on arbitrary substrates by chemical vapor deposition. *Nano Lett.* (2009).

145. Strupinski, W., Grodecki, K., Wysmolek, A., Stepniewski, R., Szkopek, T., Gaskell, P. E., Grüneis, A., Haberer, D., Bozek, R., Krupka, J. & Baranowski, J. M. Graphene epitaxy by chemical vapor deposition on SiC. *Nano Lett.* (2011).

146. Kim, K. S., Zhao, Y., Jang, H., Lee, S. Y., Kim, J. M., Kim, K. S., Ahn, J. H., Kim, P., Choi, J. Y. & Hong, B. H. Large-scale pattern growth of graphene films for stretchable transparent electrodes. *Nature* (2009).

147. Si, Y. & Samulski, E. T. Synthesis of water soluble graphene. *Nano Lett.* (2008).

148. Guo, H.-L., Wang, X.-F., Qian, Q.-Y., Wang, F.-B. & Xia, X.-H. A Green Approach to the Synthesis of Graphene Nanosheets. *ACS Nano* (2009).

149. Stankovich, S., Dikin, D. A., Piner, R. D., Kohlhaas, K. A., Kleinhammes, A., Jia, Y., Wu, Y., Nguyen, S. B. T. & Ruoff, R. S. Synthesis of graphene-based nanosheets via chemical reduction of exfoliated graphite oxide. *Carbon N. Y.* (2007).

150. Yi, M. & Shen, Z. A review on mechanical exfoliation for the scalable production of graphene. *Journal of Materials Chemistry A* (2015).

151. Mohan, V. B., Lau, K. tak, Hui, D. & Bhattacharyya, D. Graphene-based materials and their composites: A review on production, applications and product limitations. *Composites Part B: Engineering* (2018).

152. Zhang, L., Liang, J., Huang, Y., Ma, Y., Wang, Y. & Chen, Y. Size-controlled synthesis of graphene oxide sheets on a large scale using chemical exfoliation. *Carbon* (2009).

153. Zhu, Y., Murali, S., Cai, W., Li, X., Suk, J. W., Potts, J. R. & Ruoff, R. S. Graphene and graphene oxide: Synthesis, properties, and applications. *Adv. Mater.* (2010).

154. Schwierz, F. Graphene transistors. *Nat. Nanotechnol.* **5**, 487 (2010).

155. Schwierz, F. Graphene transistors: Status, prospects, and problems. *Proc. IEEE* **101**, 1567–1584 (2013).

156. Zhan, B., Li, C., Yang, J., Jenkins, G., Huang, W. & Dong, X. Graphene field-effect transistor and its application for electronic sensing. *Small* **10**, 4042–4065 (2014).

157. Liao, C., Zhang, M., Niu, L., Zheng, Z. & Yan, F. Highly selective and sensitive glucose sensors based on organic electrochemical transistors with graphene-modified gate electrodes. *J. Mater. Chem. B* (2013).

158. Atta, N. F., Galal, A. & El-Ads, E. H. Graphene — A Platform for Sensor and Biosensor Applications. in *Biosensors - Micro and Nanoscale Applications* (2015).

159. Kuila, T., Bose, S., Mishra, A. K., Khanra, P., Kim, N. H. & Lee, J. H. Chemical functionalization of graphene and its applications. *Progress in Materials Science* (2012).

160. Georgakilas, V., Tiwari, J. N., Kemp, K. C., Perman, J. A., Bourlinos, A. B., Kim, K. S. & Zboril, R. Noncovalent Functionalization of Graphene and Graphene Oxide for Energy Materials, Biosensing, Catalytic, and Biomedical Applications. *Chemical Reviews* (2016).

161. Shah, B., Yin, P. T., Ghoshal, S. & Lee, K. B. Multimodal magnetic core-shell nanoparticles for effective stem-cell differentiation and imaging. *Angew. Chemie - Int. Ed.* (2013).

162. Bai, S. & Shen, X. Graphene-inorganic nanocomposites. *RSC Advances* (2012).

163. Wang, Z., Ping, Y., Fu, Q. & Pan, C. Preparation of Metal Nanoparticle Decorated Graphene Hybrid Composites: A Review. *MRS Adv.* **3**, 849–854 (2018).

164. Tjoa, V., Jun, W., Dravid, V., Mhaisalkar, S. & Mathews, N. Hybrid graphene-metal nanoparticle systems: Electronic properties and gas interaction. *J. Mater. Chem.* (2011).

165. Jazayeri, M. H., Amani, H., Pourfatollah, A. A., Pazoki-Toroudi, H. & Sedighimoghaddam, B. Various methods of gold nanoparticles (GNPs) conjugation to antibodies. *Sensing and Bio-Sensing Research* (2016).

166. Thangaraj, S. E., Antony, E. J., Yousuf, S., Selvakumar, P. M., Dhanaraj, P. & Enoch, I. V. M. V. Binding interaction of a fluoranthene--thiol on gold nanoparticles with $β$-cyclodextrin and DNA. *J. Exp. Nanosci.* **12**, 62–71 (2017).

167. Sun, J., Guo, A., Zhang, Z., Guo, L. & Xie, J. A conjugated aptamer-gold nanoparticle fluorescent probe for highly sensitive detection of rHuEPO-α. *Sensors* (2011).

168. Li, F., Zhang, H., Dever, B., Li, X.-F. & Le, X. C. Thermal Stability of DNA Functionalized Gold Nanoparticles. *Bioconjug. Chem.* (2013).

169. Ratnoff, O. D. The evolution of hemostatic mechanisms. *Perspect. Biol. Med.* **31**, 4–33 (1987).

170. Sosic, A., Meneghello, A., Cretaio, E. & Gatto, B. Human thrombin detection through a sandwich aptamer microarray: Interaction analysis in solution and in solid phase. *Sensors* (2011).

171. Licari, L. G. & Kovacic, J. P. Thrombin physiology and pathophysiology. *J. Vet. Emerg. Crit. Care* (2009).

172. Huntington, J. A. Molecular recognition mechanisms of thrombin. in *Journal of Thrombosis and Haemostasis* (2005).

173. Deng, B., Lin, Y., Wang, C., Li, F., Wang, Z., Zhang, H., Li, X. F. & Le, X. C. Aptamer binding assays for proteins: The thrombin example-A review. *Analytica Chimica Acta* (2014).

174. Bock, L. C., Griffin, L. C., Latham, J. a, Vermaas, E. H. & Toole, J. J. Selection of single-stranded DNA molecules that bind and inhibit human thrombin. *Nature* (1992).

175. Mir, M., Vreeke, M. & Katakis, I. Different strategies to develop an electrochemical thrombin aptasensor. *Electrochem. commun.* (2006).

176. Xiao, Y., Lubin, A. A., Heeger, A. J. & Plaxco, K. W. Label-free electronic detection of thrombin in blood serum by using an aptamer-based sensor. *Angew. Chemie - Int. Ed.* (2005).

177. Giese, B. Long-Distance Electron Transfer Through DNA. *Annu. Rev. Biochem.* (2002).

178. Yu, C. H., Ge, B., Sen, D. & Yu, H. Z. Immobilized DNA switches as electronic sensors for picomolar detection of plasma proteins. *J. Am. Chem. Soc.* (2008).

179. Gangopadhyay, R. & De, A. Conducting Polymer Nanocomposites: A Brief Overview. *Chem. Mater.* **12**, 608–622 (2000).

180. Harrison, W. A. *Electronic structure and the properties of solids: the physics of the chemical bond*. (Courier Corporation, 2012).

181. Kertesz, M., Choi, C. H. & Yang, S. Conjugated polymers and aromaticity. *Chemical Reviews* (2005).

182. Heeger, A. J. Semiconducting and metallic polymers: The fourth generation of polymeric materials. *Curr. Appl. Phys.* (2001).

183. Chiang, C. K., Fincher, C. R., Park, Y. W., Heeger, A. J., Shirakawa, H., Louis, E. J., Gau, S. C. & MacDiarmid, A. G. Electrical conductivity in doped polyacetylene. *Phys. Rev. Lett.* (1977).

184. MacDiarmid, A. G., Mammone, R. J., Kaner, R. B., Porter, S. J., Pethig, R., Heeger, A. J. & Rosseinsky, D. R. The Concept of `Doping' of Conducting Polymers: The Role of Reduction Potentials [and Discussion]. *Philos. Trans. R. Soc. A Math. Phys. Eng. Sci.* (1985).

185. Jeon, I.-R., Noma, N., Claridge, R. F. C. & Shirota, Y. Electrochemical Doping of Poly(3-vinylperylene) and Electrical Properties of Doped Polymers. *Polym. J.* **24**, 273 (1992).

186. Su, W. P., Schrieffer, J. R. & Heeger, A. J. Solitons in polyacetylene. *Phys. Rev. Lett.* (1979).

187. Su, W. P., Schrieffer, J. R. & Heeger, A. J. Soliton excitations in polyacetylene. *Phys. Rev. B* (1980).

188. Bredas, J. L., Themans, B., Andre, J. M., Chance, R. R. & Silbey, R. The role of mobile organic radicals and ions (solitons, polarons and bipolarons) in the transport properties of doped conjugated polymers. *Synth. Met.* (1984).

189. Defects and Disorder in Polymer Crystals. in *Crystals and Crystallinity in Polymers* 185–295 (Wiley-Blackwell, 2013).

190. Jaiswal, M. & Menon, R. Polymer electronic materials: a review of charge transport. *Polym. Int.* **55**, 1371–1384

191. Mott, N.F. and Davis, E. A. *Electronic process in non-crystalline materials*. *Oxford University Press.* (1979).

192. Sheng, P. Fluctuation-induced tunneling conduction in disordered materials. *Phys. Rev. B* (1980).

193. Prigodin, V. N. & Efetov, K. B. Metal-insulator transition in an irregular structure of coupled metallic chains. *Synth. Met.* **65**, 195–201 (1994).

194. Schäfer-Sieber, D. & Roth, S. Limitation of the conductivity of polyacetylene by conjugational defects. *Synth. Met.* **28**, D369–D374 (1989).

195. Kivelson, S. & Heeger, A. J. First-order transition to a metallic state in polyacetylene: A strong-coupling polaronic metal. *Phys. Rev. Lett.* **55**, 308–311 (1985).

196. Elschner, A., Kirchmeyer, S., Lovenich, W., Merker, U. & Reuter, K. *PEDOT: Principles and Applications of an Intrinsically Conductive Polymer*. *Chemical Communications* (2010).

197. Tourillon, G. & Garnier, F. New electrochemically generated organic conducting polymers. *J.*

Electroanal. Chem. (1982).

198. Feldhues, M., Kämpf, G., Litterer, H., Mecklenburg, T. & Wegener, P. Polyalxykothiophenes soluble electrically conducting polymers. *Synth. Met.* (1989).

199. Jonas, F. & Schrader, L. Conductive modifications of polymers with polypyrroles and polythiophenes. *Synth. Met.* (1991).

200. Heywang, G. & Jonas, F. Poly(alkylenedioxythiophene)s - New, very stable conducting polymers. *Adv. Mater.* (1992).

201. Krebs, F. C. Fabrication and processing of polymer solar cells: A review of printing and coating techniques. *Solar Energy Materials and Solar Cells* (2009).

202. Rivnay, J., Inal, S., Collins, B. A., Sessolo, M., Stavrinidou, E., Strakosas, X., Tassone, C., Delongchamp, D. M. & Malliaras, G. G. Structural control of mixed ionic and electronic transport in conducting polymers. *Nat. Commun.* (2016).

203. Ding, Y., Invernale, M. A. & Sotzing, G. A. Conductivity trends of pedot-pss impregnated fabric and the effect of conductivity on electrochromic textile. *ACS Appl. Mater. Interfaces* (2010).

204. Kim, Y. H., Sachse, C., MacHala, M. L., May, C., Müller-Meskamp, L. & Leo, K. Highly conductive PEDOT:PSS electrode with optimized solvent and thermal post-treatment for ITO-free organic solar cells. *Adv. Funct. Mater.* (2011).

205. Nardes, A. M., Kemerink, M., Janssen, R. A. J., Bastiaansen, J. A. M., Kiggen, N. M. M., Langeveld, B. M. W., Van Breemen, A. J. J. M. & De Kok, M. M. Microscopic understanding of the anisotropic conductivity of PEDOT:PSS thin films. *Adv. Mater.* (2007).

206. Takano, T., Masunaga, H., Fujiwara, A., Okuzaki, H. & Sasaki, T. PEDOT nanocrystal in highly conductive PEDOT:PSS polymer films. *Macromolecules* (2012).

207. Crispin, X., Marciniak, S., Osikowicz, W., Zotti, G., Gon, A. W. D. van der, Louwet, F., Fahlman, M., Groenendaal, L., Schryver, F. De & Salaneck, W. R. Conductivity, morphology, interfacial chemistry, and stability of poly(3,4-ethylene dioxythiophene)–poly(styrene sulfonate): A photoelectron spectroscopy study. *J. Polym. Sci. Part B Polym. Phys.* **41**, 2561–2583 (2003).

208. Nardes, A. M., Kemerink, M. & Janssen, R. A. J. Anisotropic hopping conduction in spin-coated PEDOT:PSS thin films. *Phys. Rev. B - Condens. Matter Mater. Phys.* (2007).

209. Aleshin, A. N., Williams, S. R. & Heeger, A. J. Transport properties of poly(3,4-ethylenedioxythiophene)/poly(styrenesulfonate). *Synth. Met.* **94**, 173–177 (1998).

210. Yan, H. & Okuzaki, H. Effect of solvent on PEDOT/PSS nanometer-scaled thin films: XPS and STEM/AFM studies. *Synth. Met.* (2009).

211. Lin, Y. J., Ni, W. S. & Lee, J. Y. Effect of incorporation of ethylene glycol into PEDOT:PSS on electron phonon coupling and conductivity. *J. Appl. Phys.* (2015).

212. Pathak, C. S. Effect of dimethyl sulfoxide on the electrical properties of PEDOT:PSS/n-Si heterojunction diodes. *Curr. Appl. Phys.* **15**, 528–534 (2015).

213. Kim, J.-S., Jung, J. H., Lee, D. E. & Joo, J. J. Enhancement of electrical conductivity of poly(3,4-ethylenedioxythiophene)/poly(4-styrenesulfonate) by a change of solvents. *Synth. Met.* **126**, 311–316 (2002).

214. Zhang, S., Kumar, P., Nouas, A. S., Fontaine, L., Tang, H. & Cicoira, F. Solvent-induced changes in PEDOT:PSS films for organic electrochemical transistors. *APL Mater.* (2015).

215. White, H. S., Kittlesen, G. P. & Wrighton, M. S. Chemical derivatization of an array of three gold microelectrodes with polypyrrole: fabrication of a molecule-based transistor. *J. Am. Chem. Soc.* **106**, 5375–5377 (1984).

216. Rivnay, J., Inal, S., Salleo, A., Owens, R. M., Berggren, M. & Malliaras, G. G. Organic electrochemical transistors. *Nat. Rev. Mater.* **3**, 17086 (2018).

217. Nielsen, C. B., Giovannitti, A., Sbircea, D. T., Bandiello, E., Niazi, M. R., Hanifi, D. A., Sessolo, M., Amassian, A., Malliaras, G. G., Rivnay, J. & McCulloch, I. Molecular Design of Semiconducting Polymers for High-Performance Organic Electrochemical Transistors. *J. Am. Chem. Soc.* (2016).

218. Lu, J., Pinto, N. J. & MacDiarmid, A. G. Apparent dependence of conductivity of a conducting polymer on an electric field in a field effect transistor configuration. *J. Appl. Phys.* (2002).

219. Nilsson, D., Robinson, N., Berggren, M. & Forchheimer, R. Electrochemical logic circuits. *Adv. Mater.* (2005).

220. Epstein, A. J., Hsu, F. C., Chiou, N. R. & Prigodin, V. N. Electric-field induced ion-leveraged metal-insulator transition in conducting polymer-based field effect devices. *Curr. Appl. Phys.* (2002).

221. Hsu, F.-C., Prigodin, V. & J. Epstein, A. Electric-field-controlled conductance of "metallic" polymers in a transistor structure. *Phys. Rev. B* **74**, (2006).

222. Abdullayeva, N. & Sankir, M. Influence of electrical and ionic conductivities of organic electronic ion pump on acetylcholine exchange performance. *Materials (Basel).* (2017).

223. Bernards, D. A. & Malliaras, G. G. Steady-state and transient behavior of organic electrochemical transistors. *Adv. Funct. Mater.* **17**, 3538–3544 (2007).

224. Bernards, D. A. & Malliaras, G. G. Steady-state and transient behavior of organic electrochemical transistors. *Adv. Funct. Mater.* (2007).

225. Friedlein, J. T., Shaheen, S. E., Malliaras, G. G. & McLeod, R. R. Optical Measurements Revealing Nonuniform Hole Mobility in Organic Electrochemical Transistors. *Adv. Electron. Mater.* **1**, 1500189

226. Inal, S., Malliaras, G. G. & Rivnay, J. Benchmarking organic mixed conductors for transistors. *Nat. Commun.* (2017).

227. Proctor, C. M., Rivnay, J. & Malliaras, G. G. Understanding volumetric capacitance in conducting polymers. *J. Polym. Sci. Part B Polym. Phys.* (2016).

228. Srinivasan, S. Electrode/electrolyte interfaces: Structure and kinetics of charge transfer. in *Fuel Cells* 27–92 (Springer, 2006).

229. Volkov, A. V., Wijeratne, K., Mitraka, E., Ail, U., Zhao, D., Tybrandt, K., Andreasen, J. W., Berggren, M., Crispin, X. & Zozoulenko, I. V. Understanding the Capacitance of PEDOT:PSS. *Adv. Funct. Mater.* (2017).

230. Tybrandt, K., Zozoulenko, I. V. & Berggren, M. Chemical potential-electric double layer coupling in conjugated polymer-polyelectrolyte blends. *Sci. Adv.* (2017).

231. Lin, F. & Lonergan, M. C. Gate electrode processes in an electrolyte-gated transistor: Non-Faradaically versus Faradaically coupled conductivity modulation of a polyacetylene ionomer. *Appl. Phys. Lett.* (2006).

232. Yan, F., Zhang, M. & Li, J. Solution-Gated Graphene Transistors for Chemical and Biological Sensors. *Adv. Healthc. Mater.* **3**, 313–331 (2014).

233. Lin, P. & Yan, F. Organic thin-film transistors for chemical and biological sensing. *Advanced Materials* (2012).

234. Lin, P., Yan, F. & Chan, H. L. W. Ion-sensitive properties of organic electrochemical transistors. *ACS Appl. Mater. Interfaces* (2010).

235. Brown, T. M., Kim, J. S., Friend, R. H., Cacialli, F., Daik, R. & Feast, W. J. Built-in field electroabsorption spectroscopy of polymer light-emitting diodes incorporating a doped poly(3,4-ethylene dioxythiophene) hole injection layer. *Appl. Phys. Lett.* (1999).

236. Fromherz, P. Three levels of neuroelectronic interfacing: Silicon chips with ion channels, nerve cells, and brain tissue. in *Annals of the New York Academy of Sciences* (2006).

237. Khodagholy, D., Gurfinkel, M., Stavrinidou, E., Leleux, P., Herve, T., Sanaur, S. & Malliaras, G. G. High speed and high density organic electrochemical transistor arrays. *Appl. Phys. Lett.* (2011).

238. Defranco, J. A., Schmidt, B. S., Lipson, M. & Malliaras, G. G. Photolithographic patterning of organic electronic materials. *Org. Electron. physics, Mater. Appl.* (2006).

239. Colin, R., Mark, R., Mang-mang, L. & Zhenan, B. Organic thin film transistors. *Rev. Lit. Arts Am.* (2004).

240. Scheiblin, G., Aliane, A., Strakosas, X., Curto, V. F., Coppard, R., Marchand, G., Owens, R. M., Mailley, P. & Malliaras, G. G. Screen-printed organic electrochemical transistors for metabolite sensing. *MRS Commun.* (2015).

241. Scheiblin, G., Coppard, R., Owens, R. M., Mailley, P. & Malliaras, G. G. Referenceless pH Sensor using Organic Electrochemical Transistors. *Adv. Mater. Technol.* (2017).

242. Sirringhaus, H., Kawase, T., Friend, R. H., Shimoda, T., Inbasekaran, M., Wu, W. & Woo, E. P. High-resolution inkjet printing of all-polymer transistor circuits. *Science (80-.).* (2000).

243. Håkansson, A., Han, S., Wang, S., Lu, J., Braun, S., Fahlman, M., Berggren, M., Crispin, X. & Fabiano, S. Effect of (3-glycidyloxypropyl)trimethoxysilane (GOPS) on the electrical properties of PEDOT:PSS films. *J. Polym. Sci. Part B Polym. Phys.* (2017).

244. Stavrinidou, E., Leleux, P., Rajaona, H., Khodagholy, D., Rivnay, J., Lindau, M., Sanaur, S. & Malliaras, G. G. Direct measurement of ion mobility in a conducting polymer. *Adv. Mater.* (2013).

245. Gentile, F., Coppedè, N., Tarabella, G., Villani, M., Calestani, D., Candeloro, P., Iannotta, S. & Di Fabrizio, E. Microtexturing of the conductive PEDOT:PSS Polymer for superhydrophobic organic electrochemical transistors. *Biomed Res. Int.* (2014).

246. Zhang, F., Nyberg, T. & Inganäs, O. Conducting Polymer Nanowires and Nanodots Made with Soft Lithography. *Nano Lett.* (2002).

247. Ouyang, S., Xie, Y., Zhu, D., Xu, X., Wang, D., Tan, T. & Fong, H. H. Photolithographic patterning of PEDOT:PSS with a silver interlayer and its application in organic light emitting diodes. *Org. Electron. physics, Mater. Appl.* (2014).

248. Carotenuto, G., Nicola, S. De, Ausanio, G., Massarotti, D., Nicolais, L. & Pepe, G. P. Synthesis and characterization of electrically conductive polyethylene-supported graphene films. *Nanoscale Res. Lett.* **9**, (2014).

249. Curreli, M., Zhang, R., Ishikawa, F. N., Chang, H. K., Cote, R. J., Zhou, C. & Thompson, M. E. Real-time, label-free detection of biological entities using nanowire-based FETs. *IEEE Trans. Nanotechnol.* (2008).

250. C Peruzzi S Battistoni, A. Verna, S. Marasso, P. D'Angelo, V. Erokhin, S. Iannotta An efficient synergic approach for lithium ions detection based on OECT devices. In submission (2018).

251. FRENS, G. Controlled Nucleation for the Regulation of the Particle Size in Monodisperse Gold Suspensions. *Nat. Phys. Sci.* (1973).

252. Rao, R., Tishler, D., Katoch, J. & Ishigami, M. Multiphonon Raman scattering in graphene. *Phys. Rev. B - Condens. Matter Mater. Phys.* (2011).

253. Malard, L. M., Pimenta, M. A., Dresselhaus, G. & Dresselhaus, M. S. Raman spectroscopy in graphene. *Physics Reports* (2009).

254. Saito, R., Hofmann, M., Dresselhaus, G., Jorio, A. & Dresselhaus, M. S. Raman spectroscopy of graphene and carbon nanotubes. *Adv. Phys.* (2011).

255. Zhou, L.-J., Hou, Z. F. & Wu, L.-M. First-Principles Study of Lithium Adsorption and Diffusion on Graphene with Point Defects. *J. Phys. Chem. C* (2012).

256. Yoo, E. J., Kim, J., Hosono, E., Zhou, H. S., Kudo, T. & Honma, I. Large reversible Li storage of graphene nanosheet families for use in rechargeable lithium ion batteries. *Nano Lett.* (2008).

257. Garay-Tapia, A. M., Romero, A. H. & Barone, V. Lithium adsorption on graphene: From isolated adatoms to metallic sheets. *J. Chem. Theory Comput.* (2012).

258. Sethuraman, V. A., Hardwick, L. J., Srinivasan, V. & Kostecki, R. Surface structural disordering in graphite upon lithium intercalation/deintercalation. *J. Power Sources* **195**, 3655–3660 (2010).

259. Ke, Q. & Wang, J. Graphene-based materials for supercapacitor electrodes – A review. *Journal of Materiomics* (2016).

260. Ghosh, S. K. & Pal, T. Interparticle coupling effect on the surface plasmon resonance of gold nanoparticles: From theory to applications. *Chemical Reviews* (2007).

261. Hutter, E. & Fendler, J. H. Exploitation of localized surface plasmon resonance. *Adv. Mater.* (2004).

262. von Smoluchowski, M. Zur kinetischen Theorie der Brownschen Molekularbewegung und der Suspensionen. *Ann. Phys.* (1906).

263. Huckel, E. Die kataphorese der kugel. *Phys. Zeitschrift* **25**, 204–210 (1924).

264. Pfeiffer, C., Rehbock, C., Huhn, D., Carrillo-Carrion, C., de Aberasturi, D. J., Merk, V., Barcikowski, S. & Parak, W. J. Interaction of colloidal nanoparticles with their local environment: the (ionic) nanoenvironment around nanoparticles is different from bulk and determines the physico-chemical properties of the nanoparticles. *J. R. Soc. Interface* (2014).

265. Giangregorio, M. M., Jiao, W., Bianco, G. V, Capezzuto, P., Brown, A. S., Bruno, G. & Losurdo, M. Insights into the effects of metal nanostructuring and oxidation on the work function and charge transfer of metal/graphene hybrids. *Nanoscale* **7**, 12868–12877 (2015).

266. Bianco, G. V., Giangregorio, M. M., Losurdo, M., Sacchetti, A., Capezzuto, P. & Bruno, G. Demonstration of improved charge transfer in graphene/Au nanorods plasmonic hybrids stabilized by benzyl thiol linkers. *J. Nanomater.* **2016**, 9 (2016).

267. Pica, A., Russo Krauss, I., Merlino, A., Nagatoishi, S., Sugimoto, N. & Sica, F. Dissecting the contribution of thrombin exosite i in the recognition of thrombin binding aptamer. *FEBS J.* (2013).

268. Macaya, R. F., Schultze, P., Smith, F. W., Roe, J. A. & Feigon, J. Thrombin-binding DNA aptamer forms a unimolecular quadruplex structure in solution. *Proc. Natl. Acad. Sci.* (1993).

269. Padmanabhan, K., Padmanabhan, K. P., Ferrara, J. D., Sadler, J. E. & Tulinsky, A. The structure of alpha-thrombin inhibited by a 15-mer single-stranded DNA aptamer. *J. Biol. Chem.* **268**, 17651–17654 (1993).

270. Krauss, I. R., Merlino, A., Giancola, C., Randazzo, A., Mazzarella, L. & Sica, F. Thrombin-aptamer recognition: A revealed ambiguity. *Nucleic Acids Res.* (2011).

271. Xue, Y., Li, X., Li, H. & Zhang, W. Quantifying thiol-gold interactions towards the efficient strength control. *Nat. Commun.* (2014).

272. Kealy, T. J. & Pauson, P. L. A new type of organo-iron compound. *Nature* (1951).

273. Wilkinson, G., Rosenblum, M., Whiting, M. C. & Woodward, R. B. THE STRUCTURE OF IRON BIS-CYCLOPENTADIENYL. *J. Am. Chem. Soc.* (1952).

274. Cass, A. E. G., Davis, G., Francis, G. D., Allen, H., Hill, O., Aston, W. J., Higgins, I. J., Plotkin, E. V., Scott, L. D. L. & Turner, A. P. F. Ferrocene-Mediated Enzyme Electrode for Amperometric Determination of Glucose. *Anal. Chem.* (1984).

275. Carrara, S., Cavallini, A., Leblebici, Y., De Micheli, G., Bhalla, V., Valle, F., Samor, B., Benini, L., Ricc, B., Vikholm-Lundin, I. & Munter, T. Capacitance DNA bio-chips improved by new probe immobilization strategies. in *Microelectronics Journal* (2010).

276. Dąbrowski, A. Adsorption - From theory to practice. *Adv. Colloid Interface Sci.* (2001).

277. Hüfner, S. *Photoelectron spectroscopy. Principles and applications*. *Photoelectron spectroscopy. Principles and applications* (1995).

278. Zhang, F., Cao, H., Yue, D. & Zhou, Z. Graphene covalently modified by DNA G-base. *J. Phys. Chem. C* (2013).

279. Wang, X., Ishii, Y., Ruslinda, A. R., Hasegawa, M. & Kawarada, H. Effective surface functionalization of nanocrystalline diamond films by direct carboxylation for pdgf detection via aptasensor. *ACS Appl. Mater. Interfaces* (2012).

280. Furukawa, M., Yamada, T., Katano, S., Kawai, M., Ogasawara, H. & Nilsson, A. Geometrical characterization of adenine and guanine on Cu(1 1 0) by NEXAFS, XPS, and DFT calculation. *Surf. Sci.* (2007).

281. Pontiroli, D., Aramini, M., Gaboardi, M., Mazzani, M., Sanna, S., Caracciolo, F., Carretta, P., Cavallari, C., Rols, S., Tatti, R., Aversa, L., Verucchi, R. & Riccò, M. Tracking the hydrogen motion in defective graphene. *J. Phys. Chem. C* (2014).

282. Longo, A., Verucchi, R., Aversa, L., Tatti, R., Ambrosio, A., Orabona, E., Coscia, U., Carotenuto, G. & Maddalena, P. Graphene oxide prepared by graphene nanoplatelets and reduced by laser treatment. *Nanotechnology* (2017).

283. Tatti, R., Aversa, L., Verucchi, R., Cavaliere, E., Garberoglio, G., Pugno, N. M., Speranza, G. & Taioli, S. Synthesis of single layer graphene on Cu(111) by C60supersonic molecular beam epitaxy. *RSC Adv.* (2016).

284. Liu, L., Wang, S., Zhu, Z., Li, M. & Sun, B. Electrochemistry of a C84- C2(IV)-modified electrode in aqueous solutions and its interaction with guanine. *J. Phys. Chem. C* (2011).

285. Nardi, M., Verucchi, R., Aversa, L., Casarin, M., Vittadini, A., Mahne, N., Giglia, A., Nannarone, S. & Iannotta, S. Electronic properties of tetrakis(pentafluorophenyl)porphyrin. *New J. Chem.* (2013).

286. Jia, Y. & Li, F. Studies of Functional Nucleic Acids Modified Light Addressable Potentiometric Sensors: X-ray Photoelectron Spectroscopy, Biochemical Assay, and Simulation. *Anal. Chem.* **90**, 5153–5161 (2018).

287. Chung, S., Moon, J. M., Choi, J., Hwang, H. & Shim, Y. B. Magnetic force assisted electrochemical sensor for the detection of thrombin with aptamer-antibody sandwich formation. *Biosens. Bioelectron.* (2018).

288. Li, T., Liu, Z., Wang, L. & Guo, Y. Gold nanoparticles/Orange II functionalized graphene nanohybrid based electrochemical aptasensor for label-free determination of insulin. *Rsc Adv.* **6**, 30732–30738 (2016).

289. Furukawa, M., Fujisawa, H., Katano, S., Ogasawara, H., Kim, Y., Komeda, T., Nilsson, A. & Kawai, M. Geometrical characterization of pyrimidine base molecules adsorbed on Cu(1 1 0) surfaces: XPS and NEXAFS studies. in *Surface Science* (2003).

290. Khattak, G. D., Mekki, A. & Wenger, L. E. X-ray photoelectron spectroscopy (XPS) and magnetic susceptibility studies of vanadium phosphate glasses. *J. Non. Cryst. Solids* **355**, 2148–2155 (2009).

291. Castner, D. G., Hinds, K. & Grainger, D. W. X-ray photoelectron spectroscopy sulfur 2p study of organic thiol and disulfide binding interactions with gold surfaces. *Langmuir* **12**, 5083–5086 (1996).

292. Deng, J., Yuan, S., Li, X., Wang, K., Xie, L., Li, N., Wang, J. & Huang, N. Heparin/DNA aptamer co-assembled multifunctional catecholamine coating for EPC capture and improved hemocompatibility of

vascular devices. *Mater. Sci. Eng. C* (2017).

293. Qu, D., Zheng, M., Zhang, L., Zhao, H., Xie, Z., Jing, X., Haddad, R. E., Fan, H. & Sun, Z. Formation mechanism and optimization of highly luminescent N-doped graphene quantum dots. *Sci. Rep.* (2014).

294. Liu, Y., Yan, K., Okoth, O. K. & Zhang, J. A label-free photoelectrochemical aptasensor based on nitrogen-doped graphene quantum dots for chloramphenicol determination. *Biosens. Bioelectron.* (2015).

ACKNOWLEDGEMENTS

Firstly, I would like to express my sincere gratitude to my supervisor Dr. Salvatore Iannotta from the Institute of Materials for Electronics and Magnetism (IMEM) of Parma who offered me the opportunity to be involved in the world of Organic Bioelectronics. I want to thank him for his continuous support for my Ph.D study and related research, for his patience, motivation and immense knowledge. His guidance helped me in all the time of research and writing of this work.

Besides my supervisor, I would like to thank the rest of the other people from IMEM. Huge thanks go to Dr. Giuseppe Tarabella, Dr. Pasquale D'Angelo, Dr. Filippo Fabbri, Dr. Francesca Rossi, Dr. Giovanna Trevisi, Dr. Victor Erokhin, Dr. Svetlana Erokhina and Dr. Tatiana Berzina, who in different extent and modalities, have contributed decisively to my PhD. I want to thank Dr. Roberto Verucchi and Dr. Laura Pasquardini, from the IMEM Trento unit, for their advices and suggestions.

My sincere thanks also goes to Prof. Andrea Secchi who provided an opportunity to join his team as intern, and who gave access to the laboratory and research facilities. Without his precious support, it would have not been possible to conduct this research.

I would like to thank my lab mates and friends: Valentina (Casso), Davide (Meh!) and Regina (дорогой) for their continued support and for all the funny moments inside and outside the Lab. Thanks are also due to my Parma's friends Serena and Matia for being a significant part of this long experience far from home and for being lovely friends.

My sincere gratitude goes to my interested, encouraging and always-enthusiastic partner in crime Dr. Silvia Battistoni. Her experience has provided to me a great source of inspiration and the model for much of what I am now in scientific research. I will miss our time together, our laughs and jokes but the thing that I will miss most will be singing in the car during our road trip.

Last but not the least, I would like to thank my family, Francesco and all my friends for supporting me spiritually throughout writing this thesis and my life in general.